



City Research Online

City, University of London Institutional Repository

Citation: Veerasamy, Dhamotharan (2019). Effect on flap transition of upstream wake turbulence. (Unpublished Doctoral thesis, City, University of London)

This is the accepted version of the paper.

This version of the publication may differ from the final published version.

Permanent repository link: <https://openaccess.city.ac.uk/id/eprint/22341/>

Link to published version:

Copyright: City Research Online aims to make research outputs of City, University of London available to a wider audience. Copyright and Moral Rights remain with the author(s) and/or copyright holders. URLs from City Research Online may be freely distributed and linked to.

Reuse: Copies of full items can be used for personal research or study, educational, or not-for-profit purposes without prior permission or charge. Provided that the authors, title and full bibliographic details are credited, a hyperlink and/or URL is given for the original metadata page and the content is not changed in any way.

Effect on Flap Transition of Upstream Wake Turbulence

Thesis submitted as part of the requirement
for the fulfilment of a degree of
Doctor of Philosophy
by
Dhamotharan Veerasamy



School of Mathematics, Computer Science & Engineering
City, University of London
February 2019

Contents

Acknowledgements	v
Abstract	vii
1 Introduction	1
1.1 Background	1
1.2 High-Lift Devices	2
1.2.1 Flow characteristics of high-lift devices	3
1.3 Laminar – turbulent transition	6
1.4 Motivation	15
2 Experimental details	17
2.1 Experimental setup	17
2.2 Comparison of wake characteristics	22
2.3 Probes and instrumentation	26
3 Transitional intermittency distribution	31
3.1 Introduction	31
3.2 Determination of transition onset point using Skewness	37
3.3 A rational method for intermittency measurement	42
3.4 Summary	53
4 Transition due to aerofoil wake-boundary layer interaction	55
4.1 Introduction	55
4.2 Transitional characteristics	59
4.2.1 Mean velocity profile	59
4.2.2 Fluctuating velocity	65
4.2.3 Disturbance energy growth	71
4.2.4 Power spectral density	75
4.2.5 Correlation measurement	80
4.2.6 Effect of gap on the streak spacing	83

4.2.7	Effect of Reynolds number on the streak spacing	85
4.3	Discussion and Summary	88
5	Linear stability analysis	93
5.1	Introduction	93
5.2	Solver validation	96
5.3	Base flow velocity profile	100
5.4	Results and discussion	103
6	Conclusions and recommendations	109
	Appendix A Uncertainty analysis	115

Acknowledgment

I take this opportunity to express my sincere thanks to people who have greatly assisted me with my my PhD research. First of all, I thank my first supervisor Prof. Chris Atkin for his guidance and support throughout the PhD project. My heartfelt appreciations for his motivation and encouragement for my research and for my other activities such as my successful participation in Airbus Fly Your Ideas. His time management and leadership qualities are some important skills that I would like to inherit from him. Next, I would like to thank my second supervisor Prof. Michael Gaster for his constant advice and mentoring during my experimental research. His profound knowledge and experience on transition and stability helped me immensely to carry out my PhD research successfully. I would like to thank Prof. O N Ramesh from Indian Institute of Science (IISc), for being my mentor since my Master's studies at IISc. It was at IISc where I was exposed to the fascinating subjects of fluid dynamics and boundary layer theory. Thanks and appreciations to my senior colleagues Pradeepa, Ricky, Marco and my labmates Evelien, Barry, Isabella, Toby and Nick for making my experimental research at City more easier with their suggestions and useful feedback. I thank my friends, Muthu and Sathis for their cheerful support and fun times within City and in London. I extend my sincere thanks to Sathis for his tremendous contribution towards thesis editing and corrections.

I am grateful to the members of our lab technical support team, Keith, Richard and Phil who made my life easier in the lab by providing their support. Many thanks to Abhijit, Rajesh and Joel for being available anytime to clarify my technical doubts, in particular on stability theory. Last, but not the least, I would like to thank my wife Kokila, our lovely son, my parents and family members for making my life beautiful and more meaningful.

Abstract

Wake – boundary layer interactions are common in multi-element aerofoils and turbomachines. The laminar-turbulent transition mechanism in such systems, occurring due to the interaction of upstream wake with the downstream boundary layer, has been the subject of several studies reported in the literature. Nevertheless, most of the research carried out in the literature has used a circular cylinder as the upstream wake generating body, while most real applications experience upstream disturbances originating from an aerofoil wake. Further, the wake characteristics of a circular cylinder and aerofoil are entirely different; this, in turn, might result in different transitional characteristics. Thus, to reveal the mechanisms in wake boundary layer interactions in multi-element aerofoils, it is necessary to reproduce the evolving flow field as realistically as possible. In this context, the present research addresses the interaction problem considering a simplified but realistic system involving an aerofoil and a flat plate. Such an experimental setup is new and has not been employed before for transition studies.

An experimental investigation has been carried out in the low turbulence Gaster wind tunnel at City, University of London. Here, a NACA 0014 aerofoil at zero degree angle of attack is used to generate an upstream wake and a flat plate is used as the downstream surface, resulting in an interaction of the aerofoil wake with the initially laminar boundary layer on the flat plate. All the measurements in the present experiments have been carried out using hot-wire anemometry technique to obtain the mean velocity profiles and two-point correlations.

Using the new data, a skewness based technique has been developed to differentiate the laminar, turbulent and transition zones in the flow. In addition, a rational procedure for determining the intermittency is proposed with the aim to overcome the subjectivity involved in the methods proposed in the literature. The results obtained from the proposed method have been validated with the existing dual-slope method.

The core part of the investigation is the interaction of the upstream aerofoil wake and the downstream boundary layer on the flat plate. In particular, the laminar-turbulent transition characteristics due to the above interaction has been studied in the pre-transitional zone in order to understand the initial disturbance growth and further establish the transition mechanism. An important contribution lies in the study of the effect of gap between the aerofoil and the flat plate on the transitional characteristics.

From the measurements in the pre-transitional zone, it is observed that the streamwise disturbance growth is exponential. In addition, the streamwise power spectrum confirms that the spatial growth of the disturbance is similar to that of a T-S wave, which is further verified using linear stability analysis. Certainly, such spatial amplification is characteristic of natural transition. On the other hand, in the same pre-transitional region, two features typical of by-pass transition are observed: a non-modal disturbance profile in the wall-normal direction and the presence of a longitudinal streaky structure. These measurements in the pre-transitional zone reveal the presence of mixed behaviour, with characteristics of both natural and bypass transition, which is entirely different to that of the cylinder wake- boundary layer interaction and to free-stream turbulence induced transition. Another interesting observation is that the spanwise scale of the streaky structure appears to be much larger ($> 10\delta$) than that predicted by transient growth theory, and it varies with the gap between the aerofoil and the flat plate.

On the whole, the aerofoil-wake boundary layer interaction seems to result in a different type of transition mechanism which possesses features associated with both natural and bypass transition.

Nomenclature

Latin symbols

$\overline{u^3}$	Third moment of the streamwise fluctuating velocity (m^3)
\overline{U}	Local mean velocity (m/s)
\tilde{u}, \tilde{v}	Streamwise and wallnormal perturbation velocity for linear stability analysis
c	Chord length of the aerofoil (m)
C_2	Constant for TERA method
C_3	Constant for MTERA method
C_L	Lift coefficient of the wing
c_l	Lift coefficient of the aerofoil
c_p	Phase velocity (m)
d_w	Wake defect in percentage
$E_{u,se}$	Integral averaged energy, from the surface to the sheltering edge
F	Normalised frequency, $F = (2\pi f\nu \times 10^6/U_0^2)$
f	Frequency (Hz)
f_s	Sampling frequency (Hz)
h_w	Vertical gap between the aerofoil and flat plate (mm)
l	Total length of the flat plate (m)
P	Power spectral density
P_n	Normalised power spectral density, $P_n = P/(0.5U_0^2\Delta F)$
R	Correlation function

Re_c	Reynolds number based on aerofoil chord length
Re_x	Reynolds number based on streamwise station
Re_{δ^*}	Reynolds number based on displacement thickness
t	Time (s)
T_a	Amplitude of T-S wave
T_c	Ambient temperature during calibration
t_c	Convective time scale of the boundary layer (δ/\bar{U})
T_h	Threshold value
T_I	Integral time scale
T_K	Kolmogorov time scale
T_m	Ambient temperature during measurement
T_u	Turbulent intensity
T_w	Temperature of the sensor in hot-wire probe
U	Normalised mean velocity, \bar{U}/U_0
u	Streamwise fluctuating velocity, $u = (U_I - \bar{U})$
u_{rms}^3	Cube of the root mean squared fluctuating velocity (m^3)
U_0	Free-stream velocity (m/s)
u_0	Maximum defect velocity (m/s)
U_I	Instantaneous velocity in the streamwise direction
w_w	Half width of the wake
x	Streamwise distance from the flat plate leading edge (m)
x_t	Transition onset point
x_w	Streamwise gap between the aerofoil trailing edge and flat plate leading edge (x/c)
y	Wall-normal distance from the flat plate (m)

$y_{0.5}$ Wall-normal location of 50% defect velocity

z Spanwise distance (m)

Greek symbols

α Non-dimensional streamwise wave number; also used for angle of attack in chapter 1

δ_s Distance from the surface of the flat plate to the upper minimum in the fluctuation profile (sheltering edge) (m)

Δt_s sampling time interval

δ Boundary layer thickness (m)

δ^* Displacement thickness (m)

η Non-dimensional wall-normal location, y/δ^*

γ Intermittency

\Im Imaginary

ν Kinematic viscosity

ω Non-dimensional circular frequency

ϕ Amplitude function of the perturbation or Eigenfunction

ψ Stream function of the perturbation

\Re Real

Acronyms

FST Free-stream turbulence

T – S Tollmien–Schlichting

Chapter 1

Introduction

1.1 Background

Every aircraft in today's world contains the genes of 200 years of flying machine design. For instance, the concept of having separate systems for lift and thrust production was first conceived by Sir George Cayley in 1799 ([Anderson, 1999](#)), which is still the skeleton of any modern day aircraft design. In those 200 years of evolution, the first 100 years were spent mainly developing ideas in order to lift the aeroplane off the ground. Most of the attempts were aiming to equip the aircraft with high power engines in order to achieve high enough velocity to produce sufficient aerodynamic lift to raise the machine off the ground. However, with the use of powerful engines, the weight went up leading to an increase in the required velocity and the process went into a cycle without achieving the required lift. This trial and error exercise helped to realise the importance of thrust to weight ratio. Drawing inspirations from the knowledge of history, the first successful manned flight was achieved by Wright brothers in 1903. The Wright brothers managed to solve the problem of control using a wing-warping scheme. The first use of hinged, flap-like surfaces (called as ailerons) was by Henri Farman in 1909.

The next stage of aircraft evolution was to increase the payload capacity paving the way for modern air transportation. One of the hurdles encountered during the design process is to limit the increase in flight speeds, driven by increased aircraft weights, during the take-off and landing phases which became notorious for fatal accidents. This led to the invention of high-lift devices such as slats and flaps. Inspired by the aileron design, a plain flap was introduced by Royal Aircraft Factory in 1914. The modern flap system evolved from the pioneering inventions by Sir Frederick Handley Page (who was a Professor at City, University of London) and independently by G. V. Lachmann in 1917 when they introduced the concept of

leading edge slots to improve low-speed handling characteristics. In parallel, several trailing edge flaps were developed, of which the Fowler flap is the most efficient in terms of lift augmentation. Even today, the combination of the slotted flap and the Fowler flap is used as the high-lift system in modern day aircraft.

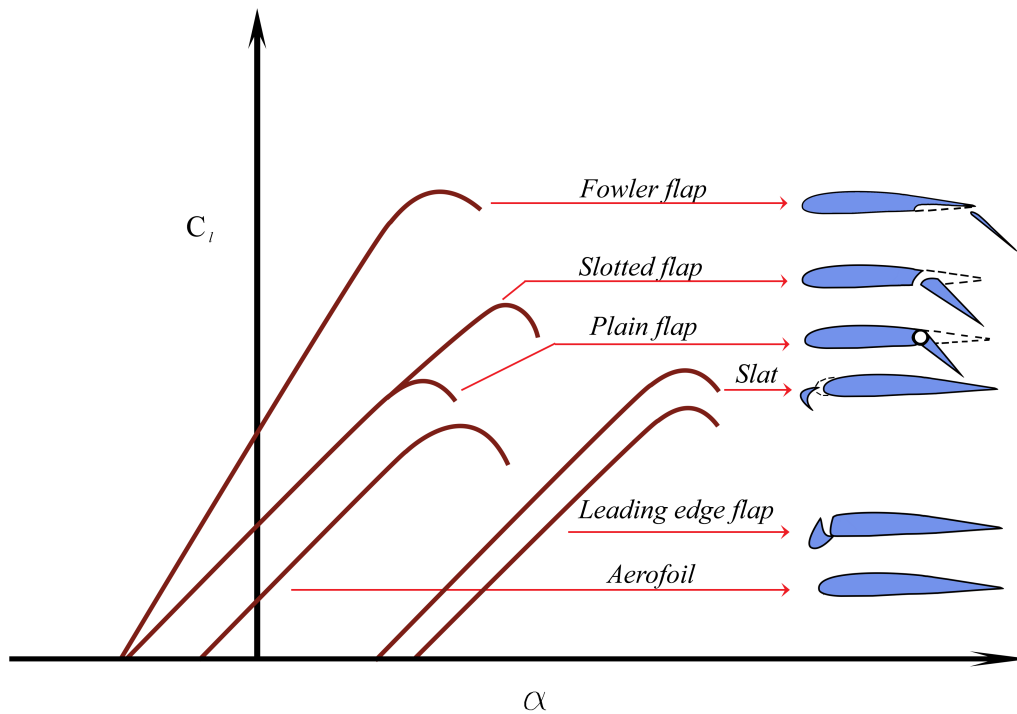


Figure 1.1: High-lift devices and its lift characteristics, (Reproduced from [Anderson, 1999](#)).

Figure 1.1 shows the lift characteristics of different types of slat/flap combinations plotted as lift coefficient (C_l) against angle of attack (α). The lift coefficient, C_l is a non-dimensional parameter which determines the lift characteristics of any aerofoil/wing. It can be clearly seen that the lift coefficient, C_l increases dramatically with the flap settings, irrespective of the type of flap. Another advantage of flap usage is that the maximum lift occurs at a lower angle of attack as compared to that of a no-flap configuration, which, in turn, would help to reduce the approach attitude angle. Among the different flaps, it can be noticed that slope of the $C_l - \alpha$ curve is higher for Fowler flap due to its increased effective camber and chord length.

1.2 High-Lift Devices

High-lift systems (slats and flaps) are more complex in design and are also costly to manufacture. For instance, according to [Rudolph \(1996\)](#), the high-lift system ac-

counts for 6% to 11% of the total production cost of a typical jet transport aircraft and it may potentially increase for higher configurations (wide body aircraft/jumbo jets). The high costs are a consequence of the need for the high-lift system to be effective for take-off and landing without affecting the cruise efficiency. Investing such an enormous amount of money in producing the high-lift devices is returnable in terms of aircraft overall performance through simultaneous increase in both $C_{L,max}$ and the lift-to-drag (L/D) ratio. Meredith (1993) has mentioned,

1. An increase in maximum lift coefficient ($C_{L,max}$) of 1.0% leads to an increase in payload of 22 passengers or 2000 kg for a fixed approach speed on landing.
2. Also, an increase in the L/D ratio of 1.0% during take-off will be equivalent to an increase in payload of 14 passengers or 1300 kg for a given range.
3. If the lift coefficient at a constant angle of attack is increased by 0.1, then the approach attitude angle will decrease by 1 degree, since the required lift could be achieved at a lower angle of attack. This allows a reduction in landing gear height, which eventually reduces the overall weight of an aircraft, thus, in turn, leads to reduced fuel consumption.

In order to fully exploit the benefits associated with the high-lift devices, an engineer has to overcome many design challenges to arrive at an optimal configuration. In the next subsection, factors governing the flow characteristics of the high-lift devices and the associated challenges in their design are discussed in detail.

1.2.1 Flow characteristics of high-lift devices

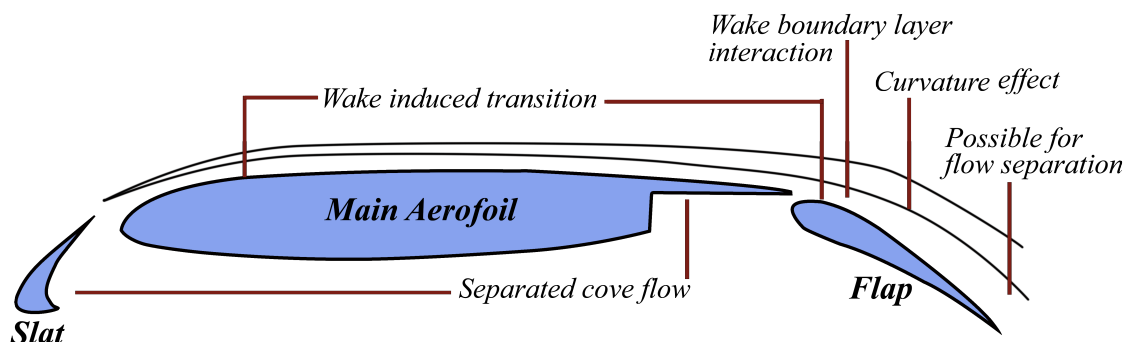


Figure 1.2: Schematic of the high-lift device and its flow characteristics.

Figure 1.2 illustrates the major factors influencing the operational characteristics of flaps at high-lift condition. Among them, wake – boundary layer interaction and

flow separation due to adverse pressure gradient are important. For instance, when the wake originating from the upstream elements (slat and main aerofoil) approaches the flap boundary layer, it will result in a displacement effect on the flow field of the flap. Such an interaction reduces the suction acting on the flap. The reduction in the flap loading or the pressure distribution due to the wake-boundary layer interaction is called damping effect, [Spaid \(2000\)](#). In addition, as the wake from the upstream main aerofoil interacts with the boundary layer of the flap, it accelerates transition from laminar to turbulent flow. Predicting the occurrence of transition on such multi-element aerofoils is important as it has a major influence on maximum lift developed by the slats and flaps. In the cruise condition, where the Reynolds number is very high, the flow over the wing becomes turbulent shortly downstream of the leading edge. But in the case of landing or take off, where the high-lift devices come into operation, the slats and flaps experience much lower Reynolds numbers (relative to cruise), which may support extended region of laminar boundary layer. From the above perspectives, understanding the laminar-turbulent transition characteristics on the high-lift devices is essential for optimizing their aerodynamic performance. [Van Dam \(1999\)](#) considers that transition prediction capability is a necessary component of any computational aerodynamics method used in high-lift design.

In addition, due to the large adverse pressure gradient on the surface of the flap, the flow may separate. However, there are situations where the flow on the flap surface remains attached but the flow off-the-surface (in the wake region) reverses. This type of behaviour is called wake bursting. [Smith \(1975\)](#) suggested that the wake bursting may decrease the $C_{L,max}$ and increase the drag. [Pomeroy et al. \(2014\)](#) investigated the wake bursting behaviour and observed that it causes an increase in turbulent fluctuation in the shear layer (in between boundary layer edge and wake core) rather than the wake core region.

[Rumsey and Ying \(2002\)](#) reviewed the capability of the CFD tools to predict the flow characteristics of high-lift devices. They confirmed that most of the models reasonably predict the lift coefficient up to $C_{L,max}$, but the value of $C_{L,max}$ is predicted incorrectly. Nevertheless, the review article is a decade old, leaving a possibility that the current CFD models may now predict $C_{L,max}$ reasonably well. However, the recent AIAA Aerospace Sciences Meeting ([Rumsey et al., 2018](#)) revealed that still we are lagging in predicting $C_{L,max}$ accurately (figure 1.3). Through further deliberations with Airbus representatives, we came to know that Airbus is facing $\pm 5\%$ error in $C_{L,max}$ prediction. Such difficulties in predicting the $C_{L,max}$ directly raises the question of what is still missing in the understanding of the flow physics

at high-lift condition?

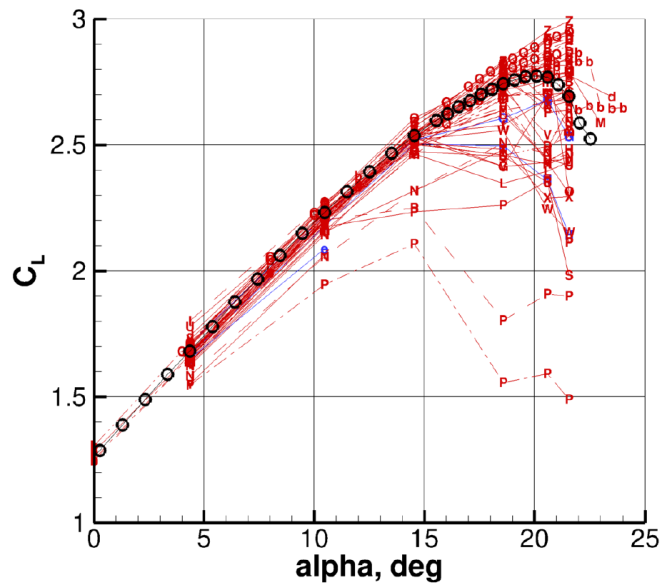


Figure 1.3: Variation of measured and predicted lift coefficient with angle of attack (AIAA Aerospace Sciences Meeting, [Rumsey et al., 2018](#)).

[Rumsey and Ying \(2002\)](#) reviewed the computational capabilities of transition prediction in high-lift devices, and it is clear from their conclusion that numerical models failed to accurately predict the transition in multi-element systems. Even in the recent high-lift prediction workshop, ([Rumsey et al., 2018](#)) confirmed that transition models are inconsistent with experimental results especially near the $C_{L,max}$ region.

To have a better understanding of complex nature of the flow at high-lift condition, there is a need to have a closer look at the physics in great detail. In particular, understanding the complex interactions underlying the flow in such multi-element aerofoil systems becomes important for better design of high-lift devices. In this context, the present PhD research aims to examine the underlying physics of the laminar-turbulent transition due to wake-boundary layer interaction. Through intensive experimental investigations, an attempt is made to understand the transition mechanism involved in them.

Having defined the research problem and the thesis objective, the rest of this chapter summarises the efforts taken in the literature with regards to the transition studies, in general. This is then followed by a brief summary of transition research in the presence of wake-boundary layer interactions.

1.3 Laminar – turbulent transition

In general, fluid flows are classified into two types, “Laminar” and “Turbulent”. Laminar flow is defined as the streamlined flow where the fluid flows smoothly, in parallel layers without any mixing; on the other hand if the flow exhibits irregular, diffusive (mixing), vortical, dissipative or any nonlinearities then it is considered as turbulent. Hitherto, there is no universal theory to determine the origin of turbulence, however it is widely accepted that the perturbations to the laminar state are naturally amplified and the flow eventually transition from laminar to turbulent. Research on this laminar–turbulent transition was initiated by Reynolds more than a century ago, and is still ongoing. As mentioned earlier, the present thesis also focuses on understanding the laminar-turbulent transition process.

Boundary layer transition

Flow over solid surfaces or through pipes is restricted by skin friction acting between the fluid and the surface. The flow adjacent to the surface has zero velocity (called the no-slip condition) and then slows down the adjacent fluid resulting in the development of a shear layer normal to the surface. The shear layer adjacent to the wall is termed the boundary layer.

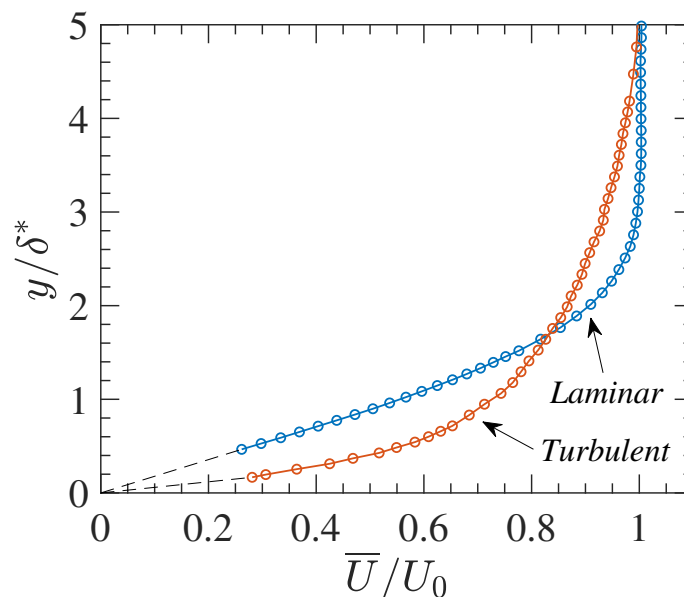


Figure 1.4: Streamwise velocity profiles of laminar and turbulent boundary layer. The abscissa shows local mean velocity is normalised with free-stream velocity; the ordinate shows wall-normal stations are normalised with displacement thickness.

Inside the boundary layer the flow may exist in either laminar or turbulent states depending mainly on the Reynolds number ($Re_x = U_0 x / \nu$). Examples of the stream-wise velocity profiles measured along the wall-normal direction for both the laminar and turbulent boundary layer is shown in figure 1.4.

The underlying physics of the transition from laminar to turbulent boundary layer is not well established. Particular problems of interest are mechanism of transition and the location of transition onset. Understanding and thereby predicting the transition onset is still a major challenge for the aerodynamics community. One of the obvious reasons for this lack of understanding is due to the influence of multiple factors on the transition onset, such as surface roughness, free-stream disturbances, pressure gradients, acoustics etc. Further, when it comes to a system with multiple aerodynamic surfaces (e.g. multi-element aerofoil, turbomachines) the interactions of the above mentioned factors significantly increase. This, in turn, makes the physics much more complex. It has been widely accepted by the research community that in general laminar–turbulent transition occurs through two different routes, which are termed *natural transition* (for 2D flows, also described as Tollmien-Schlichting type transition) and *bypass transition* (also described as free-stream turbulence induced transition). In the sections below, the characteristics of these two different transitions are discussed and eventually transitional characteristics in wake-boundary layer interactions are reviewed from the studied literature.

Before proceeding with the different types of transition it is a must to know about the receptivity. Receptivity is the mechanism by which free-stream disturbances entrain into the boundary layer and cause an initial perturbation for the generation of an unstable disturbance. For any type of transition the very first stage involves the receptivity mechanism. Subsequent stages can be discussed in terms of the stability of the laminar ‘base’ flow to these disturbances and the later stages are classified based on the type of transition, which is discussed below. If the disturbances grow in time or space, then the base flow is considered as unstable, on the other hand if it decays, it would be considered as stable.

Natural transition

The process of natural transition, for 2D flows in a low turbulence environment, is schematically represented in the figure 1.5. The initial stage of the natural transition starts with the formation and amplification of a two-dimensional (2D) wave called as Tollmien-Schlichting (T-S) wave. This stage is termed as the primary instability stage. These 2D wave amplifies and then grows into a three-dimensional (3D)

wave, thus entering the second stage of transition termed as secondary instability. These waves then break down into turbulent spots, which ultimately result in a fully turbulent flow condition further downstream.

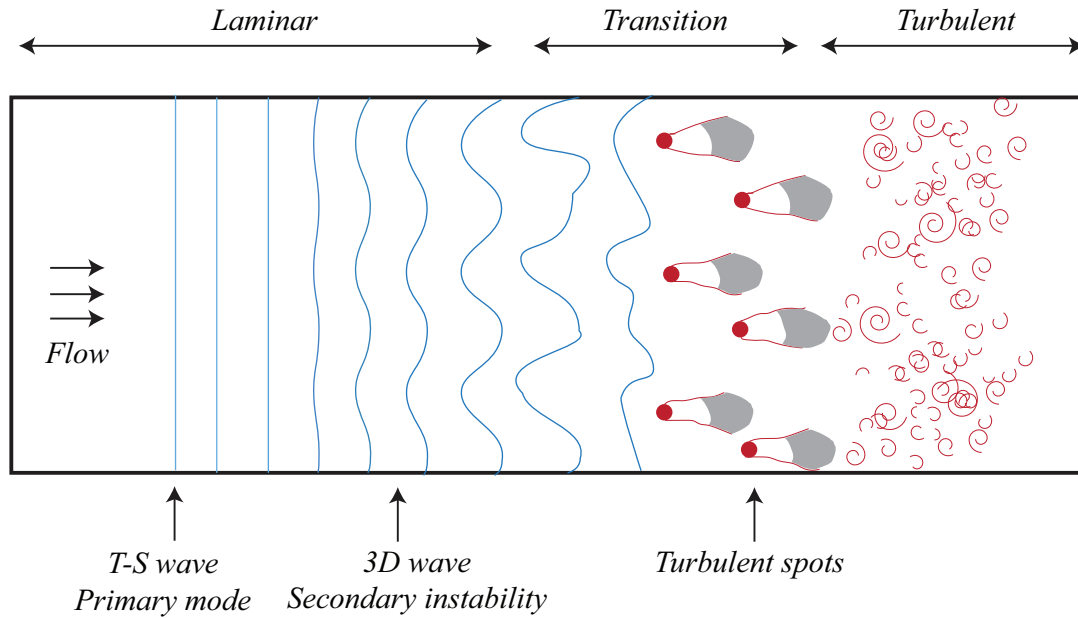


Figure 1.5: Schematic representation of stages in natural transition.

The initial instability and amplification of the 2D waves can be studied through linear stability theory, by assuming that the initial disturbances can be expressed as the sum of a set of Fourier modes ($e^{i(\alpha x + \beta z - \omega t)}$) where α and β represent the streamwise and spanwise wave numbers and ω represents the angular frequency. For a 2D spatially growing disturbance α is complex, while β and ω are taken as real. By superimposing the Fourier modes on a two-dimensional parallel base flow, and further linearising the Navier-Stokes equations, a stability equation (referred to the Orr-Sommerfeld equation) can be derived and solved for stable and unstable modes. Using linear stability theory, one can also obtain the critical Reynolds number (Re_{cr}) above which disturbances are amplified. It is worth mentioning that Re_{cr} is different from the transition onset Reynolds number (Re_{tr}). Linear stability theory could not predict the value of Re_{tr} because of the nonlinear stages involved between Re_{cr} and Re_{tr} . If the amplitudes of the wave beyond Re_{cr} is not high enough then it will reach the second branch of the neutral curve and decay. On the other hand, if the amplification of the disturbance is high enough, then a spanwise variation occurs in the 2D wave, whereby the 2D wave is transformed into a 3D wave. This was experimentally observed in Klebanoff et al. (1962) and it is noticed that there is an occurrence of peaks and valleys along the spanwise direction. It is reasoned that the secondary instability of the 2D disturbance is the cause of the 3D

state, [Herbert \(1988\)](#). Also, from the distribution of the vorticity field, [Klebanoff et al. \(1962\)](#) noticed the existence of longitudinal vortices, later it was observed as Λ shaped vortices. Further downstream of the vortex region, turbulent spots are generated, leading to transition. So, in general, if the initial disturbance in the flow propagates through linear (2D disturbance and its growth) and nonlinear (3D wave and vortices) stages, then it is called natural transition.

Though the general process of natural transition is described above, different types of natural transition are identified in the literature. In particular, five different types of natural transition (N, K, C, H and S) have been observed so far, which are not discussed here for brevity and also not to deviate from the scope of the thesis. Nonetheless, it is emphasized here that the different types of natural transitions can be attributed to the different types of secondary instability associated with the amplitude of the 2D disturbance. Also, it is noticed that the alignment of Λ vortices is different for K (ordered peak-valley pattern), C and H (staggered peak-valley pattern) type transition, which is visually observed in [Saric \(1986\)](#). A detailed review on all the types of natural transition can be found in [Kachanov \(1994\)](#).

Bypass transition

Bypass transition usually occurs in a flow if the level of free-stream disturbances are high. This type of transition occurs rapidly rather than the slow, exponential growth of the T-S wave in natural transition. In the pre-transitional region (defined as the stages before the appearance of turbulent spots) of bypass transition, none of the characteristics of the natural transition can be noticed. From the past three decades of research, the inherent characteristics of the bypass transition are well established as described below.

Firstly, the word ‘bypass’ was first used by [Morkovin \(1969\)](#) to describe the type of transition that occurs via bypassing the growth of T-S wave and its secondary instability. Further, the transition occurs at a Reynolds number well below the critical Reynolds number determined from the linear stability theory. These kind of transitional characteristics were commonly observed in flows with high levels of free-stream turbulence. Later, [Klebanoff \(1971\)](#) investigated this problem and he noticed the oscillation of the boundary layer thickness and he referred it as a breathing mode; later it was termed as Klebanoff mode by [Kendall \(1985\)](#). Also, Klebanoff observed the existence of streaky structures in the boundary layer. In fact, [Dryden \(1937\)](#) and [Taylor \(1939\)](#) already spotted these free-stream turbulence-induced characteristics, but it was known to the research community only after Klebanoff’s work. Later,

Arnal and Juillen (1978) showed that the energy of the dominant disturbance in the boundary layer occurs at low frequency. Further they noticed, the maximum value of the streamwise perturbation ($u_{rms,max}$) along the wall-normal direction occurs at the middle of the boundary layer in contrast to the near wall location in natural transition.

Extensive research on free-stream turbulence-induced transition was conducted by the scientific community after Kendall (1985). Kendall demonstrated the existence of streaky structures through spanwise correlation measurement and flow visualisation. He also confirmed that the streamwise streaky structures are unsteady and their spanwise spacing would be of the order of twice the spacing of the minimum correlation. Subsequently, the breakdown of the streaky structure was studied by Boiko et al. (1994). Earlier, it was hypothesised that the secondary instability of the streaky structure would be caused by the co-existence of a T-S wave. This was verified by Boiko et al. (1994) by artificially introducing the T-S wave, who also observed that the presence of a T-S wave rapids the streak breakdown process into turbulence. Simultaneously, the detailed measurement of Westin et al. (1994) showed that, before the onset of transition, u_{rms} (root mean squared value of the streamwise disturbances) values reaches up to 10% inside the boundary layer, further the maximum streamwise disturbance ($u_{rms,max}$) grows in proportion to $x^{0.5}$ in the streamwise direction.

The physical reason behind the linear disturbance growth was not clear until theoreticians came up with algebraic or transient growth theory (Luchini, 1996; Andersson et al., 1999). The development of this theory is briefly discussed here. Initially, for an inviscid parallel flow, Ellingsen and Palm (1975) suggested that, if a three-dimensional disturbance is imposed on a two-dimensional flow, then the streamwise disturbance velocity (u) grows linearly (algebraically) with respect to time and produces alternating high and low velocity streaks. Landahl (1980) examined the same case and showed that the streamwise disturbance velocity increases linearly in time with no limit on amplitude. Also, he offered a physical reasoning for the streak growth mechanism: if a fluid element is displaced in the wall-normal direction, it retains its streamwise momentum and cause perturbation on the streamwise velocity component. This mechanism is referred to the lift-up effect. Later, this theory was extended to the viscous case by introducing a small three-dimensional disturbance with a large streamwise scale by Hultgren and Gustavsson (1981). They showed that viscosity will eventually limit the maximum streamwise disturbance growth and eventually lead to decay due to viscous dissipation. This inviscid phenomenon

with viscous damping is referred to transient growth, i.e. an algebraic growth of the disturbance energy until viscosity becomes significant (Fransson, 2003).

The above developed theories are temporal; for a wall-bounded shear flows, a spatial theory would be more appropriate, since the disturbances are amplified in the spatial direction. In this context, Luchini (1996) developed a similar approach for a Blasius boundary layer. He concluded that the streamwise disturbance velocity grows linearly with $x^{0.213}$ (x - streamwise stations). Further, Luchini (2000) determined the optimal perturbation for a maximum energy growth, and if optimal perturbations are used, the energy growth is proportional to the streamwise location. He also predicted the streamwise disturbance profile and compared with experiments (Westin et al., 1994) which agreed well with non-modal theory.

Afterwards, an extensive study on the free-stream turbulence induced transition was carried out by Matsubara and Alfredsson (2001). They have shown that all the pre-transitional characteristics obtained until that period and the associated results (algebraic energy growth and streamwise disturbance profile) matches well with the non-modal theory developed by Luchini (2000). This confirms that the pre-transitional region of the bypass transition is algebraic/transient in nature. In addition, they have demonstrated that the spanwise scale of the streaks and its height are almost equal to the boundary layer thickness. Through correlation measurement, they confirmed that the spanwise spacing between the streaks are approximately twice the boundary layer thickness. Knowing the above characteristics of bypass transition, Fransson et al. (2005) conducted experiments with a range of free-stream turbulence intensities (1.4-6.7%) and found that the initial disturbance energy is proportional to the square of the free-stream turbulence intensity, T_u^2 . Furthermore, the growth of the streamwise disturbance energy (u_{rms}^2) varies linearly with the streamwise station ($u_{rms}^2 \sim x$). They also obtained a scaling for energy growth, whereby when the Re_x is normalised with Re_x at the position where $u_{rms} = 0.1U_0$, the energy growth curves obtained for various turbulent intensities collapse into a single curve. Such a scaling is again confirmed by Balamurugan and Mandal (2017) through PIV measurements.

Numerical simulations have also been carried out by several researchers (Rai and Moin, 1993; Jacobs and Durbin, 2001; Brandt et al., 2004; Ovchinnikov et al., 2008) to understand the physics of bypass transition. Among them, (Jacobs and Durbin, 1998, 2001) tried to explain the receptivity and the streak generation involved in bypass transition through a phenomenon called shear sheltering, where the shear

layer acts as a filter for the high-frequency free-stream disturbances, allowing only the low-frequency disturbances to penetrate into the boundary layer. Furthermore, the low-frequency disturbances are amplified by the mean shear (Andersson et al., 1999) so that the energy spectrum shifts towards the lower frequency end.

At the end of the pre-transitional region, the streaks break down to turbulent spots. From flow visualisation of the streaks, Matsubara and Alfredsson (2001) observed that the streak breakdown occurs through an instability. From the simulation of Brandt et al. (2004), it was proposed that streak breakdown could be characterised as either sinuous or varicose modes (type of oscillations of the streak). Several investigations were carried out on the streak instability, but the present research focus is limited to the initial disturbance growth region, so streak instability is not discussed further here. However, it is referred to the recent experimental paper by Balamurugan and Mandal (2017) who carried out a detailed investigation on the sinuous and varicose mechanisms.

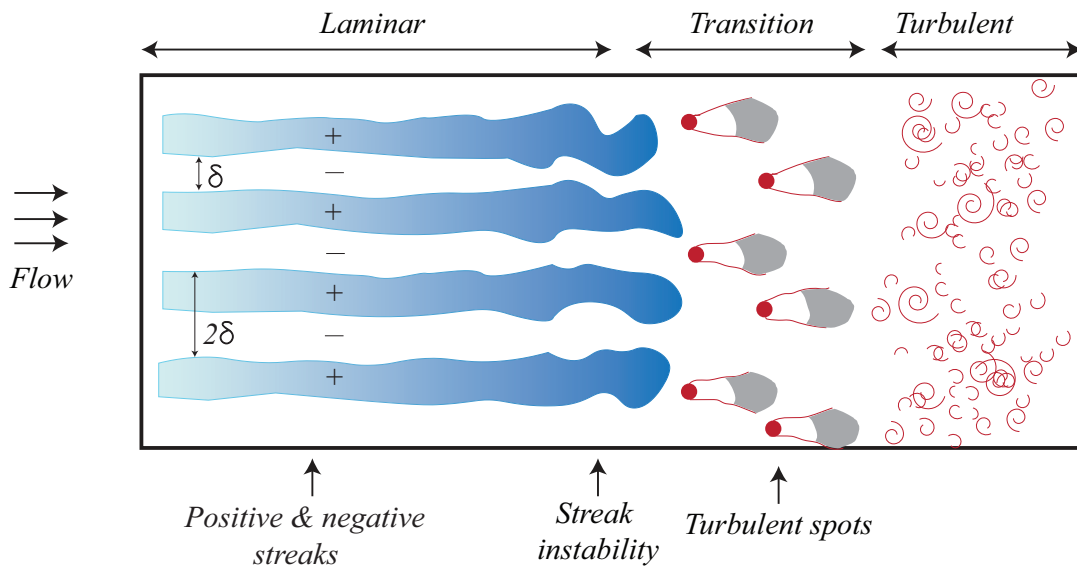


Figure 1.6: Schematic representation of stages in bypass transition.

By studying the above literature, it can be summarised that, in the pre-transitional region of a flow exhibiting bypass transition, the following characteristics are observed:

1. The flow remains laminar and the mean velocity profile is only slightly perturbed. In the near wall, there would be a velocity gain and at the edge of the boundary layer, there would be a velocity deficit. It was reasoned that velocity gain and deficit are due to the occurrence of high-speed and low-speed streaks.

2. The measured streamwise disturbance profile is in correspondence with the non-modal disturbance profile obtained from transient growth theory.
3. The maximum streamwise disturbance energy ($u_{rms,max}^2 \sim x$) grows linearly in the streamwise direction, termed as algebraic growth.
4. Unsteady streaky structures are present inside the boundary layer. The spanwise scale of the streaks is approximately equal to the boundary layer thickness (δ) and the spanwise streak spacing would be around twice the boundary layer thickness (2δ), illustrated in figure 1.6.

The above four observations or findings are the key characteristics of the by-pass transition.

Wake induced transition

Having discussed the two different transition mechanisms in the above sections, the current discussion is focussed on transition studies involving wake-boundary layer interactions. The scenario of wake-boundary layer interaction usually occurs in multi-element aerofoils and turbomachinery flows. So, here the literature from both areas is reviewed. In case of the multi-element aerofoils, earlier studies on wake-boundary layer interaction were more focused on studying the shape of the confluent boundary layer and its turbulent characteristics. For instance, [Savill and Zhou \(1983\)](#) carried out an extensive study on interaction effects by placing an upstream wake generated from different types of geometry (circular cylinder, aerofoil and flat plate) and its interaction on the downstream flat plate boundary layer. From the measurements on the flat plate, they concluded that an exchange of vortices takes place between the wake and the boundary layer; vortices drawn out from the boundary layer maintain its coherence structure in the wake, similarly vortices from the wake drawn into the boundary layer. [De Zhou and Squire \(1985\)](#) extended that work by adding further complexities such as pressure gradient and wake asymmetry. They found that the level of turbulence in the wake has the strongest influence on the interaction. [Squire \(1989\)](#) carried out an extensive review of wake-boundary layer interaction studies. He concluded that the upstream wake increases the overall turbulence level in the flow and accelerates the transition onset. But it is clear from his review article ([Squire, 1989](#)) that, at that time, no study had attempted to explore receptivity and transition mechanisms in the wake-boundary layer interaction.

Bertelrud (1998) and Bertelrud and Anders (2002) have documented comprehensive reports on transition location in a high-lift device at high Reynolds number, however the mechanism of transition is not established. Lee and Kang (2000) aligned two aerofoils in tandem and concluded that bypass transition occurs in flow around the downstream aerofoil when the incoming wakes are fully turbulent. The configuration of the tandem aerofoil, however, does not accurately represent a realistic multi-element aerofoil system, due to the lack of vertical gap between the individual aerofoils.

In the last two decades, the transition research on this topic shifted towards study of the interaction of a circular cylinder wake with the flat plate boundary layer (Kyriakides et al., 1999; Ovchinnikov et al., 2006; Pan et al., 2008; Mandal and Dey, 2011; He et al., 2013). Such a configuration could have been inspired by turbomachinery studies, where the periodically passing wakes from the rotor blade are mimicked in the laboratory by a moving circular cylinder arrangement and where the downstream stator blade is simulated using a flat plate with imposed pressure distribution (Liu and Rodi, 1991; Wu et al., 1999; Coull and Hodson, 2011). This sort of arrangement helps to reveal the effect of periodic wake passing on the turbo-machine blades. The reasoning for utilising a circular cylinder for wake generation could be as follows: according to Pfeil and Herbst (1979), the global wake characteristics (mean velocity profile and drag) of the circular cylinder and turbine blades are nearly the same, making it logical to choose the circular cylinder instead of a blade aerofoil. Also in the laboratory, designing a moving circular cylinder arrangement would be easier than using real blades.

Similar wake-boundary layer interaction effects occur in multi-element aerofoils, with the only exception that the upstream wake is steady in the case of multi-element aerofoils as opposed to an unsteady wake in turbomachinery flows. Hence, for transition studies in such multi-element system, a static cylinder is employed. The results of several studies using this type of configuration are discussed below.

Pan et al. (2008) observed that coherent structures of the circular cylinder wake behave largely like spanwise vortices. These spanwise vortices interact at a distance with the boundary layer of the downstream body and induce a secondary, spanwise vortex. Secondary instability of this vortex structure leads to hairpin-shaped vortices (head of the hairpin oriented in the streamwise direction) which grow with the associated streaky structures, eventually leading to a fully turbulent flow. Mandal and Dey (2011) also reported similar transition mechanisms in the cylinder-flat plate

system. From these simplified experiments, which still involve complex physics, we can deduce the physics of this particular transition mechanism associated with discrete vortices in the free-stream; moreover the vortex axes are, in these cases, particular in being aligned perpendicular to both the surface normal and to the free-stream. In addition, for the cylinder-wake boundary layer interaction, [Ovchinnikov et al. \(2006\)](#); [Pan et al. \(2008\)](#); [Mandal and Dey \(2011\)](#) observed features of bypass transition such as self-similarity of the u_{rms} profile, low and high speed streaks. From the literature of cylinder-wake boundary layer interaction, we can confirm, the onset of transition depends upon the upstream wake coherent structures, but the later stage of breakdown is more like bypass transition.

1.4 Motivation

As discussed in the brief literature review above, several experiments have been conducted to study the wake-boundary layer interaction in multi-element aerofoils. However, the studies do not necessarily offer insights into more realistic wake interactions, for example in wing-flap system and turbomachinery flows. There are some key differences between the wakes generated from cylinder and aerofoil despite their similar global characteristics (drag and mean velocity profile). In particular, the wake originating from cylinder contains shed vortices which are not so dominant in an aerofoil-generated wake, especially in the main-element of the aerofoil at higher Reynolds number. It is anticipated that, due to this difference in the wake kinematics of the cylinder and aerofoil, the receptivity mechanism involved in the transition process could be different, which in turn might lead to a different transition mechanism. It is therefore the goal of the present research to consider a more realistic representation of practical aerodynamic systems. Fundamental experimental investigations have therefore been carried out to understand the transition mechanism involved in multi-element aerofoils by considering an aerofoil-flat plate system. It is emphasised here that such an experimental setup involving a fully turbulent aerofoil wake and a flat plate is not utilised before to study the transition process.

Outline of this thesis

The main contents of the thesis are organised as follows.

Chapter 2: Firstly, the distinct wake characteristics of circular cylinder and aerofoil are discussed. The basic details of the experimental setup and measurements techniques used in this study are then described. Tunnel characteristics, types of probes and types of measurements carried out and their uncertainty levels are discussed in more detail.

Chapter 3: In order to study the transition mechanism, it is vital to determine the laminar, transitional and turbulent regimes in the given flow. For this purpose, a skewness based technique is used. Further, a new rational technique to measure intermittency is proposed.

Chapter 4: Reveals the major theme of the work where the receptivity of the boundary layer to the wake disturbance and its transition characteristics are discussed. The present experimental observations are compared with the transitional characteristics of natural, bypass and wake-induced transition studies reported previously in the literature. It is concluded that the transition mechanism has different characteristics to the ones observed in the literature.

Chapter 5: Discusses the results of a spatial, linear stability analysis carried out on the experimentally-measured mean velocity profiles to reveal some characteristics of natural transition. Further, a parametric study on the confluent wake-boundary layer is performed to explore the effect of wake geometry on the unstable boundary layer mode.

Chapter 6: Briefly summarises the key conclusions obtained from the present work and possible directions for future investigations are suggested.

Chapter 2

Experimental details

The details of the experimental arrangement and instrumentation are discussed in this chapter. Further, as described in Chapter 1, there are significant differences between the wake characteristics of an aerofoil and a circular cylinder. These differences are characterised using preliminary measurements and the choice of an aerofoil wake for the present thesis investigation is explained.

2.1 Experimental setup

All the experiments reported in this thesis were performed in the Gaster wind tunnel at City, University of London. This is a closed circuit wind tunnel with a test section dimension of $0.924 \times 0.915 \times 3.66$ m and the lateral width is diverged from 0.924 to 0.940 m in the downstream direction. The operating velocity inside the test section could be set within the range of 0.5 - 25 m/s. For the present experiment, three different velocities given by $U_0 = 5, 10$ and 20 m/s are chosen, however in most of the analyses, measurements at $U_0 = 20$ m/s is considered. The vertically mounted flat plate, made of aluminium with a total length of about 2150 mm and a thickness of 10 mm was used in the present experiment. In order to maintain the stagnation point on upper side of the flat plate, a trailing-edge flap, of 110 mm length, is employed.

The test section of the wind tunnel is removable, with different test sections utilised by colleagues for different experiments. Hence it was important to ensure that the constant pressure distribution on the flat plate was unaltered during each experiment, after re-installation of the test section. A pressure measurement was always carried out before performing each experiment and a sample number of such measurements is shown in figure 2.1. C_p stands for static pressure coefficient, which is calculated based on equation 2.1, where p and p_{ref} denotes the local static pressure

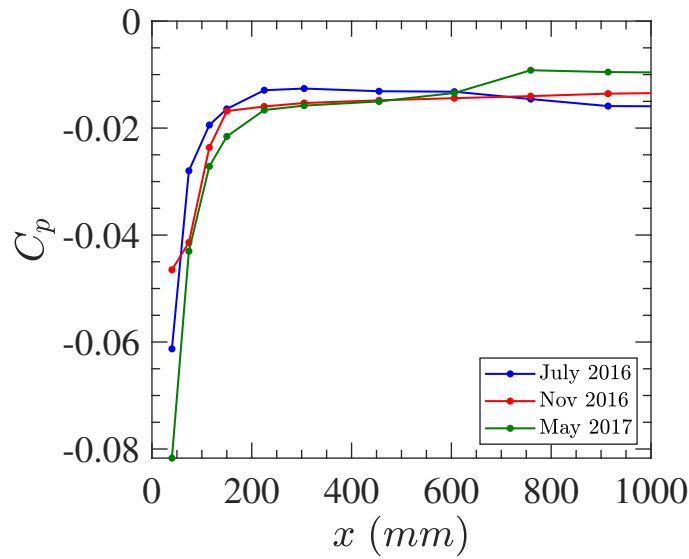


Figure 2.1: Distribution of pressure co-efficient on the surface of the flat plate without upstream wake.

and free-stream static respectively. ρ is the density of air, obtained using barometric pressure and ideal gas relation, $\rho = p/RT$. The first part of pressure measurement is at 40 mm from the leading edge. As can be ascertained from figure 2.1, the pressure distribution is approximately constant downstream of $x = 200$ mm. Even when the measurements are made at different time periods shown in the figure, it can be confirmed that a constant pressure distribution is maintained over the flat plate (within the experimental scatter).

$$C_p = \frac{p - p_{ref}}{0.5\rho U_0^2} \quad (2.1)$$

$$C_p = 1 - (\bar{U}/U_0)^2 \quad (2.2)$$

From figure 2.1, it can be noted that there is a weak suction peak where an increase in velocity of about 4% from the free-stream value is noted, as calculated from equation 2.2 (\bar{U} and U_0 denotes the local mean velocity and free-stream velocity in the streamwise direction respectively). After the suction peak, the flow smoothly and monotonically recovers to an approximately constant pressure value downstream. The presence of the suction peak near the leading edge will play a crucial role in transition experiments. For instance, a mild acceleration or any non-uniform pressure distribution in the leading edge would have a significant effect on T-S wave amplification (Klingmann et al., 1993; Westin et al., 1994). On the other hand, any flow separation at the leading edge or generation of turbulent spot at the leading edge would lead to rapid transition in the immediate downstream flow.



Figure 2.2: Shape and dimension of the flat plate leading edge.

In the present experiments, the leading edge is made up of an asymmetric, wooden bi-convex surface as shown in figure 2.2. An attempt is made to check if the non-uniform pressure distribution or the weak suction peak near the leading edge cause any disturbance in the flow downstream of the flat plate. The velocity profiles obtained using hot-wire measurements at a free-stream velocity of 20 m/s are shown in figure 2.3. The velocity profiles and the variation of boundary layer thicknesses match very well with the Blasius solution. The first derivatives of the mean velocity profile also follow the Blasius solution very closely. This is shown in figure 2.4. Such an observation confirms that the downstream flow is not disturbed by the leading edge suction peak.

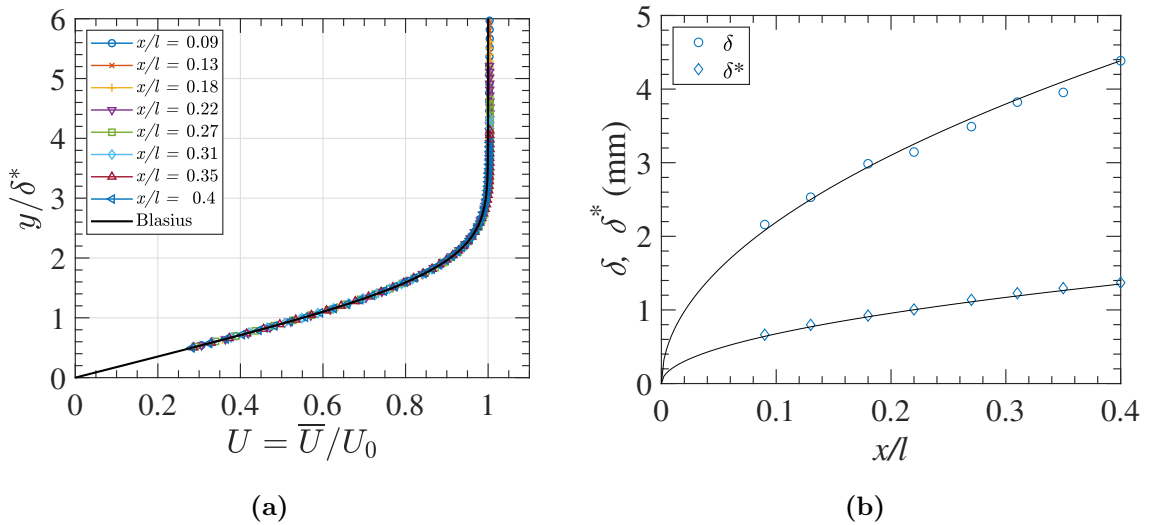


Figure 2.3: (a) Mean velocity profile and (b) the growth of boundary layer thickness and displacement thickness in the downstream distance on the flat plate (without upstream wake).

To quantify free-stream turbulence level in the tunnel, the streamwise fluctuation profiles normalised with the free-stream velocity are shown in figure 2.5. As can be seen from the figure, the free-stream turbulence intensity of the tunnel in the streamwise direction is 0.015% (within the frequency range 5Hz to 5kHz). This compares with 0.007% when the tunnel is empty. Though not shown here, the hot-wire signals did not show any sign of turbulent spots and the complete laminar profiles indicate that there was no separation upstream and the weak suction peak does not

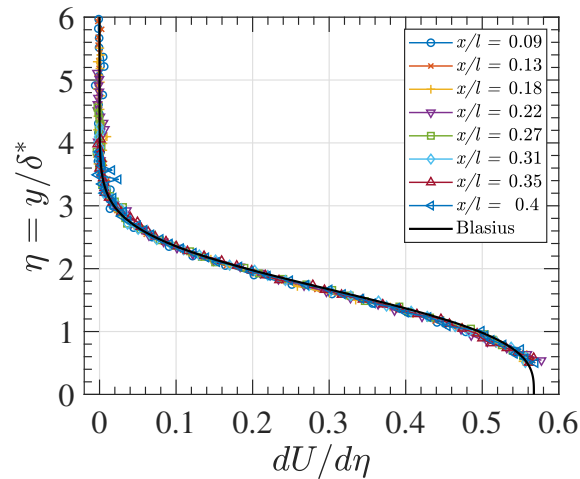


Figure 2.4: First derivative of the mean velocity profile shown in figure 2.3a.

affect the downstream flow.

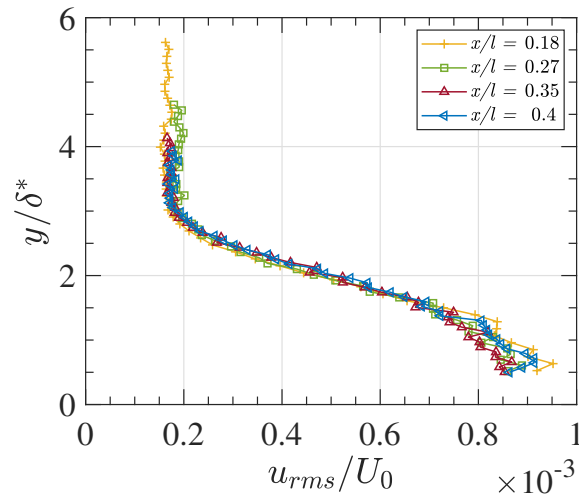


Figure 2.5: Wall-normal distribution of the streamwise fluctuating velocity measured at various streamwise stations.

As discussed in the previous chapter, an aerofoil is introduced ahead of and above the flat plate at zero degree angle of attack to study the transition due to wake-boundary layer interaction as shown schematically in figure 2.6. Various key parameters for the configuration are indicated on the schematic. The streamwise and wall-normal stations are defined using a coordinate system, $x - y$ having its origin at the leading edge of the flat plate. The vertical separation between the aerofoil and the flat plate is denoted as the ‘gap’ (h_w) and the horizontal separation is denoted as the ‘overlap’ (x_w). It is well-known from the literature (Smith, 1975; Spaid, 2000; Van Dam, 1999; Rumsey and Ying, 2002; Watanabe et al., 2006) that these two

parameters play a crucial role in determining the aerodynamic performance of a multi-element aerofoil system. A systematic study of a range of these parameters is very important since a multi-element system has to perform satisfactorily over a wide range of flap settings. Hence, in the present experiments, transition studies have been performed while varying these two parameters.

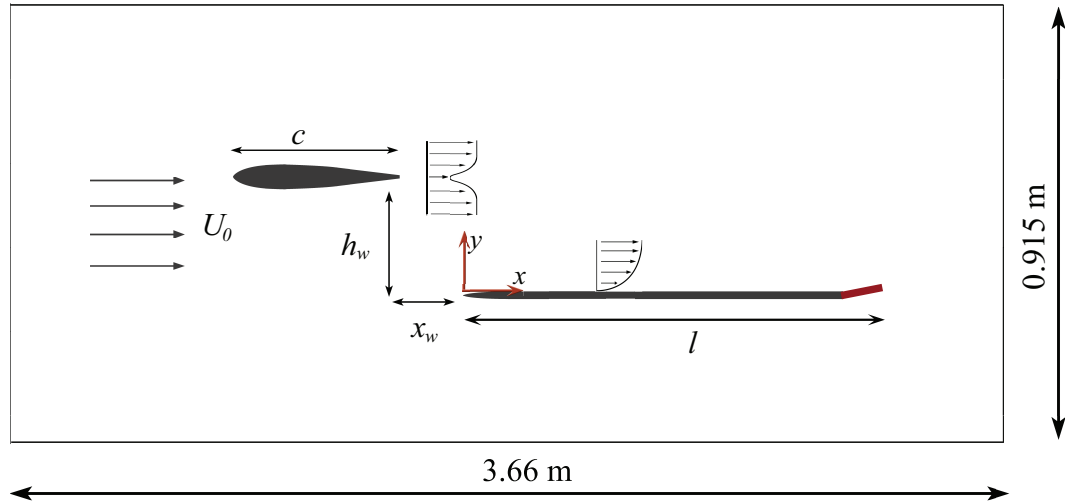


Figure 2.6: Schematic representation of the experimental setup.

The chord length (c) of the aerofoil is 250 mm. The experiments were performed at three different freestream velocities (U_0) and at various ‘overlaps’ and ‘gap’ values. The values of these parameters is mentioned clearly in table 2.1.

Case	x_w	h_w (mm)	U_0 (m/s)	Re_c ($\times 10^5$)
Case 1	0.25c	20,25,30,35,40,60,80	5,10,20	0.8,1.7,3.4
Case 2	0.5c	20,40,60	5,10,20	0.8,1.7,3.4
Case 3	0.75c	20,40,60	5,10,20	0.8,1.7,3.4

Table 2.1: Cases considered in the present experiment.

When the aerofoil is placed upstream of the flat plate, it would influence the pressure distribution on the flat plate. To ascertain the magnitude of any such influences, pressure measurements were carried out with the aerofoil placed at different ‘gaps’ (h_w) for a fixed overlap ($x_w = 0.25c$) and Reynolds number, $Re_c = 3.4 \times 10^5$. The result of these measurements are shown in figure 2.7, where the original pressure distribution on the flat plate without the aerofoil is also shown for comparison. It can be noted that the suction peak value appears to decrease when the aerofoil is present. There is also a slight overshoot (about 1% from the later constant value) in the pressure distribution once the flow recovers from the suction peak. However, the

pressure distribution on the flat plate remains approximately constant after about $x = 200$ mm. So, all the measurements were carried out downstream of this location and up to $x = 900$ mm. The flat setting is not changed throughout the experiments as the pressure distribution over the flat plate is not altered due to the variation in gap.

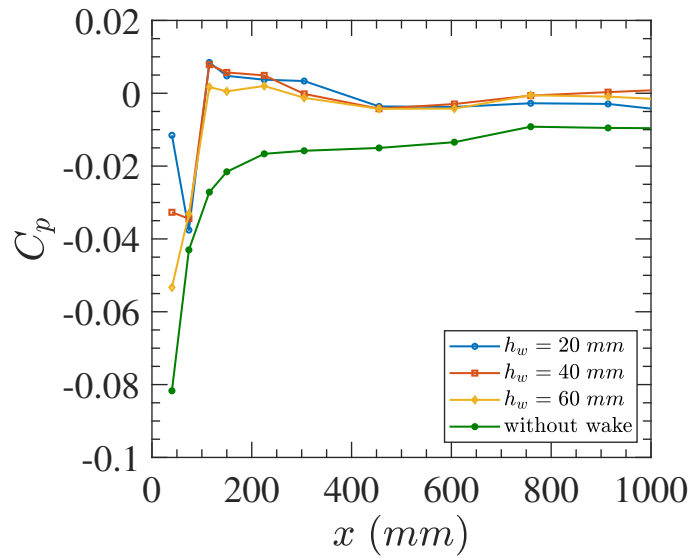


Figure 2.7: Pressure distribution for various h_w of the aerofoil.

2.2 Comparison of wake characteristics

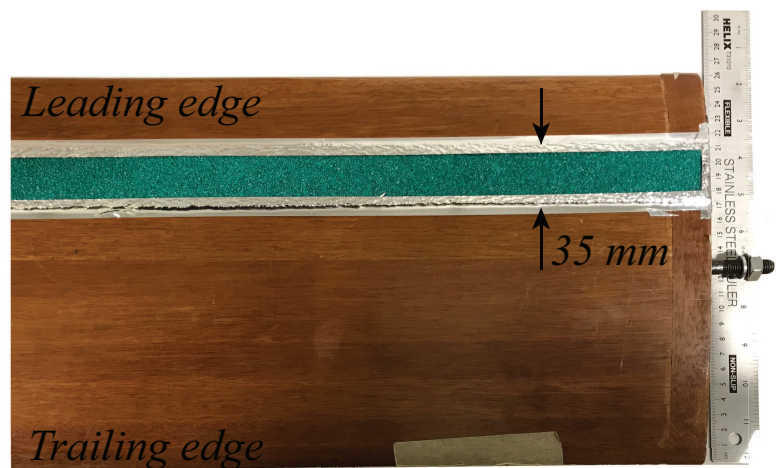


Figure 2.8: NACA 0014 aerofoil with a sandpaper roughness strip placed around 25% of chord.

To study the difference in the wake characteristics of an aerofoil and a circular cylinder, a NACA 0014 aerofoil section (see figure 2.8) is chosen for the present

experiments. The Reynolds number based on the aerofoil chord is $Re_c = 3.4 \times 10^5$, with a free-stream velocity of 20 m/s. To simulate higher Reynolds number flow over the aerofoil, a sandpaper roughness strip (average roughness height = 425 μm) is used for tripping the boundary layer at around 25% of the chord. The aerofoil was positioned at zero degree angle of attack with both ends flushed into the end walls. The mean velocity profiles of the aerofoil wake are measured at various streamwise distances using a single normal-wire probe. The results from these measurements are shown in figure 2.9a in which U_0 , \bar{U} and u_0 represent free-stream velocity, mean velocity and maximum defect velocity respectively. $\eta = y/y_{0.5}$; $y_{0.5}$ is the wall-normal location corresponding to the defect velocity being equal to 50% of maximum defect velocity. For comparison, the self-similar solution of the wake mean velocity given in equation 2.3 (Wyganski et al., 1986) is also plotted in the figure. It can be observed that the present results are in excellent agreement with the plane wake measurements of Wygnanski.

$$f(\eta_{0.5}) = \frac{U_0 - \bar{U}}{u_0} = \exp[-0.637(\eta_{0.5})^2 - 0.056(\eta_{0.5})^4] \quad (2.3)$$

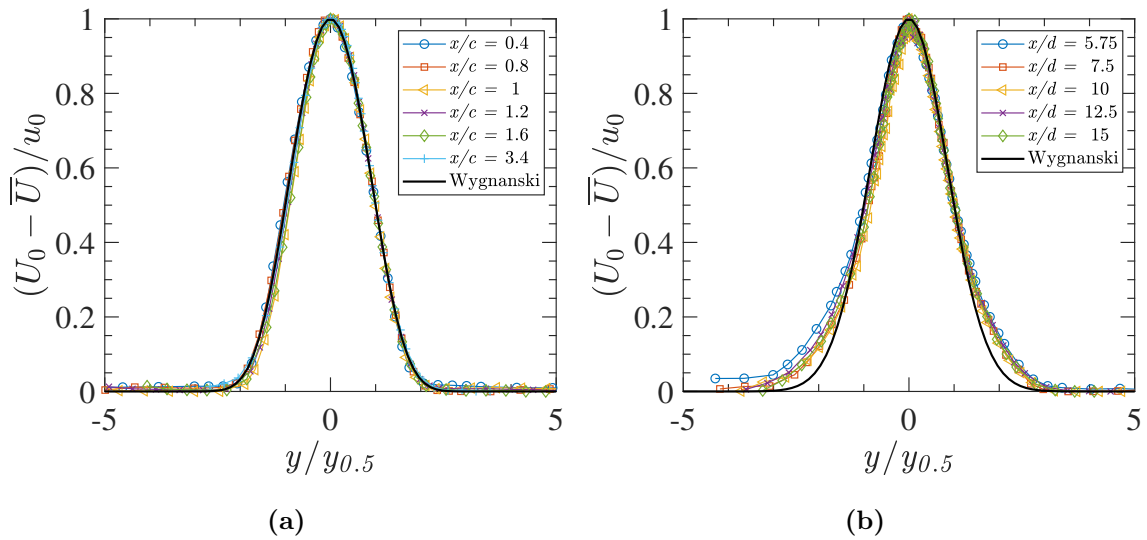


Figure 2.9: Self similar mean velocity profiles of (a) aerofoil and (b) cylinder wake compared with Wygnanski (1986).

To compare, a circular cylinder with a diameter of 20 mm is used for the wake study. The Reynolds number of the flow based on the cylinder diameter is $Re_d = 2.7 \times 10^4$. The mean velocity profiles behind the circular cylinder are shown in figure 2.9b. The comparison with Wygnanski's cylinder measurements are also in good

agreement, though there are some small differences towards the edge of the wake. These differences may be expected to reduce as the wake develops into complete self-similarity further downstream when $u_0/U_0 < 0.1$ (Pope, 2000).

It must be emphasized that these two flows are very different, hence, a direct comparison between the profiles is of little value. The present section only tries to highlight the major characteristic differences between these two wake flows.

Next, the spectral characteristics of the two wake flows are explored at a number of points across the wake profiles. The selected points in the aerofoil wake profile (at $x/c = 0.8$) are shown in figure 2.10a (points A,B,C,D,E,F) and the corresponding spectra are shown in figure 2.10b. A similar analysis for the cylinder wake profile is shown in figure 2.11a & 2.11b.

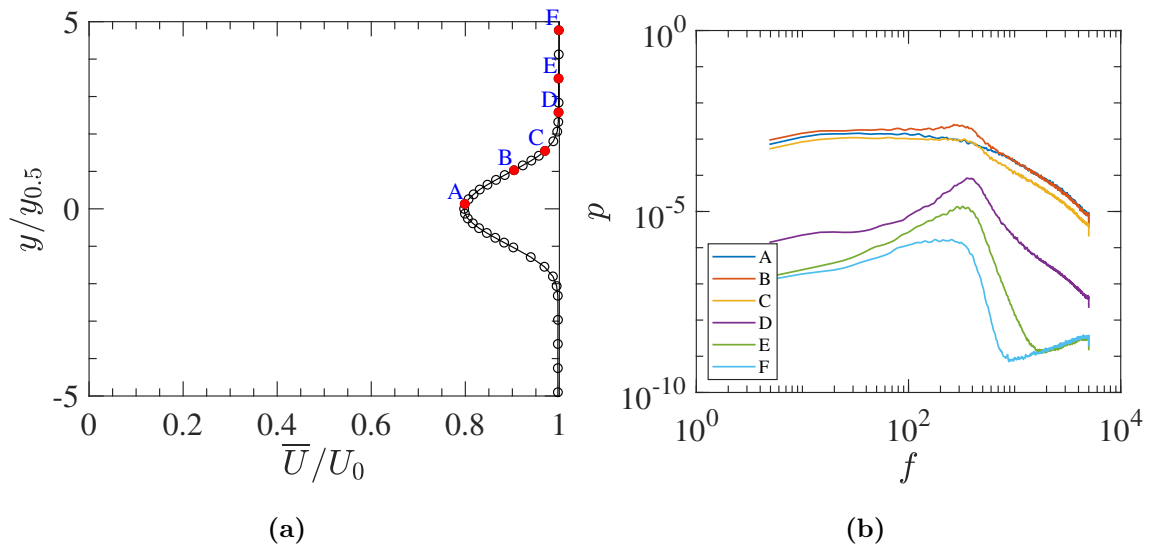


Figure 2.10: (a) Mean velocity profile of aerofoil wake at $x/c = 0.8$ and its corresponding (b) power spectral density.

It can be seen from the spectrum in the aerofoil wake (figure 2.10b) that, away from the centreline of the wake, a bandwidth of frequencies become dominant in the spectrum. This is recognized as a slightly spread-out bump in the spectrum at locations D, E and F. In contrast, the spectrum for the cylinder wake is shown to be characteristically different. It can be seen from figure 2.11b that a single frequency dominates the cylinder wake spectrum, i.e. the vortex shedding frequency behind the cylinder. Hence, we see that the nature of disturbances coming from the cylinder and aerofoil wakes are significantly different in nature and frequency content.

In order to better understand the presence of a bandwidth of dominant fre-

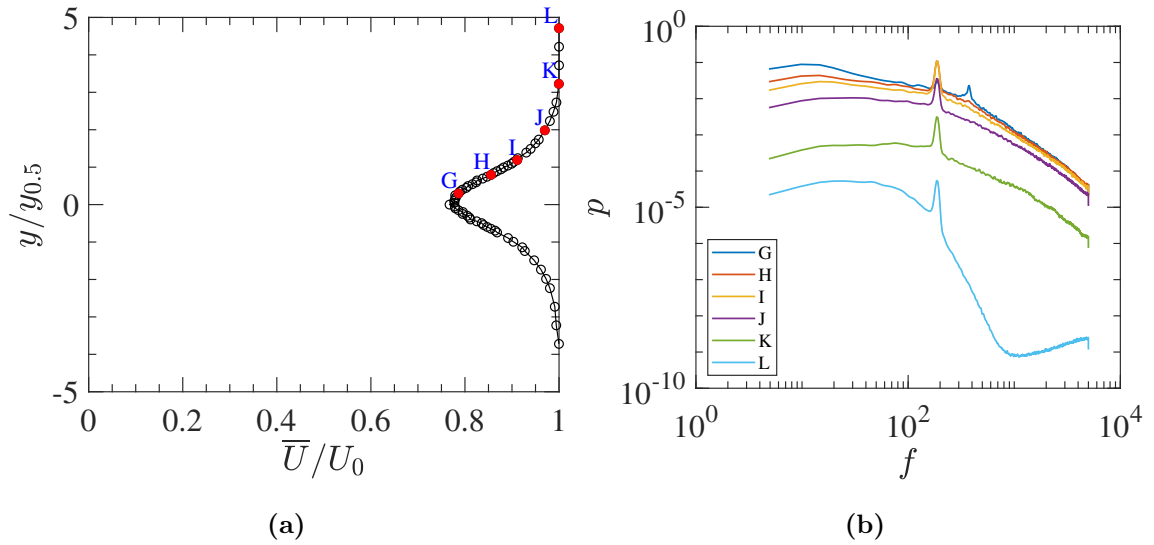


Figure 2.11: (a) Mean velocity profile of circular cylinder at $x/d = 10$ and its corresponding (b) power spectral density.

quencies in the aerofoil wake, a comparison is made with the spectrum of a plane turbulent wall-jet from the literature (figure 2.12a and 2.12b). Away from the wall, at points O, P and Q in the edge of the shear layer, a similar bumpy nature of the spectrum is clearly visible. As both flows possess such bumpy frequency characteristic towards the edge of the shear layer, it is plausible that this spectral behaviour may be associated with the intermittent turbulent flow present in this region.

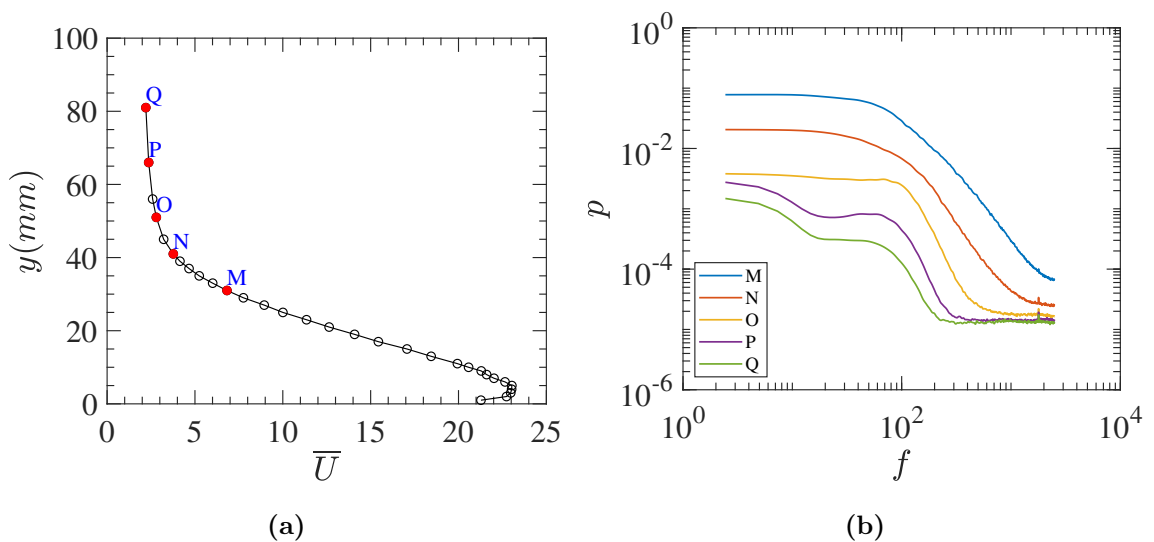


Figure 2.12: Mean velocity profile of wall jet and its corresponding streamwise spectral distribution obtained from the data of [Veerasamy, 2011](#).

Having seen the characteristic differences between the two wake flows so far, it is important to emphasize that, in the literature (Kyriakides et al., 1999; Ovchinnikov et al., 2006; Pan et al., 2008; Mandal and Dey, 2011), a circular cylinder-flat plate setup was predominantly used to study the wake-boundary layer interaction problem occurring in multi-element aerofoil systems and turbomachinery flows. However, it is shown from present results that the wake kinematics of the circular cylinder and the aerofoil are entirely different which may result in different receptivity mechanisms and, in turn, different transition mechanisms on the downstream element. Thus, in the current experiments, the aerofoil-flat plate setup was employed to realistically represent the multi-element aerofoil system for studying the wake-boundary layer interactions.

2.3 Probes and instrumentation

The streamwise velocity and its fluctuations in the boundary layer are measured using hot-wire anemometer probes. In this section, the basic working principles of hot-wire anemometry are briefly outlined along with the details of the probes used for measurement.

There are two main methods of hot-wire anemometry, namely i) constant current anemometry (CCA) ii) Constant temperature anemometry (CTA). In both these methods, a sensing wire element is used as one arm of a Wheatstone bridge. By maintaining either the current passing through the sensor element or the temperature of the sensor element as a constant, the velocity of the flow over the sensing element is determined. The basic working principle is described in detail in the textbook by Bruun (1996). The constant current anemometer was the first to be used in the earlier days, particularly for heat transfer flows. Later, with the advancement of feedback circuits and associate electronics, the constant temperature unit became the standard practice for velocity measurements.

In the present thesis, all the velocity measurements were carried out using a Dantec DISA 55M01 CTA unit. Two types of probes were used in the study which are schematically shown in figure 2.13. Both these probes are miniature probes and use a fine tungsten wire (diameter $5\mu\text{m}$, length 1.25 mm) as the sensing element. When a current is passed through the wire, it heats up due to the Joule effect. And when there is flow over the wire, it convects away some of the heat and changes the temperature of the wire. A feedback circuit is employed to pass the required amount of current through the wire by adjusting the voltage so that the temperature of the

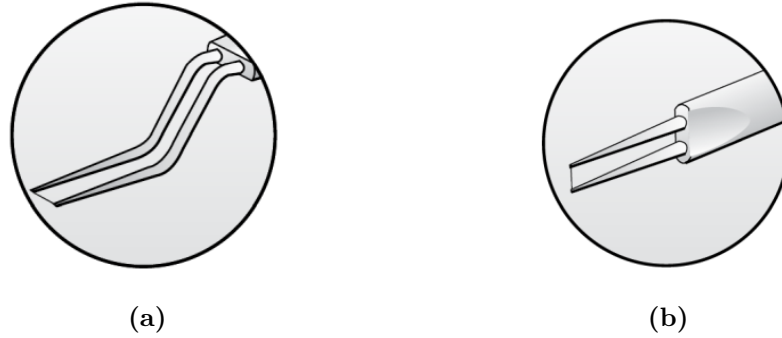


Figure 2.13: Miniature (a) Boundary layer probe, Dantech 55P15 (b) Straight wire probe, Dantech 55P11.

wire is maintained constant. A relation between the voltage drop and the flow speed is given by King's law as

$$E_I^2 = A + BU_I^n \quad (2.4)$$

A hot-wire probe measures the instantaneous voltage required to maintain the constant temperature while being in the flow. This instantaneous voltage can be converted to instantaneous velocity from equation 2.4. A , B and n in the equation are calibration constants to be determined before each experiment and this is discussed in detail in the next section. The instantaneous voltage and velocity can be split into mean (\bar{E} , \bar{U}) and fluctuating parts (e, u), as given by,

$$E_I = \bar{E} + e \quad (2.5)$$

$$U_I = \bar{U} + u \quad (2.6)$$

Differentiating equation 2.4 and substituting the decomposition into mean and fluctuations gives the relation between fluctuating voltage and fluctuating velocity as,

$$u = \frac{2\bar{E}}{Bn\bar{U}^{n-1}}e = \left(\frac{d\bar{E}}{d\bar{U}}\right)^{-1}e \quad (2.7)$$

Procedure followed in CTA setup:

1. The working temperature of the hot-wire sensor is initially set in terms of a overheat ratio, which is given as, $a = (R_w - R_0)/R_0 = \alpha_0(T_w - T_0)$. R_w and R_0 are the resistance of the wire at operating temperature (T_w) and ambient temperature (T_0).
2. The overheat ratio is usually chosen as, $a = 1.5$, which leads to the temperature of the wire around 150-170°C, which is much lower than the oxidizing temperature of 350°C for the Tungsten filament ([Bruun, 1996](#))
3. To determine the maximum frequency up to which the present anemometer setup can operate, a square-wave test is performed. This frequency is also referred to as the cut-off frequency.
4. During this test, the hot-wire was placed in the free-stream with the maximum operating velocity and a square function voltage was fed into the Wheatstone bridge. Through an oscilloscope the shortest possible impulse response is noted. By adjusting the amplifier filter and gain settings the response time is optimised.
5. The response time was noted to be around 10 – 12 μ s, which is about 80-100 kHz.
6. The sampling frequency was chosen as 10 kHz. According to Nyquist theorem, disturbances up to 5 kHz can be resolved in the present measurements. This sampling frequency can be safely assumed to capture all the fluctuations occurring in the flow since the dominant frequencies in the transitional experiments on a zero pressure gradient flat plate are noticed to be within this regime. Further, the signal was acquired for a total duration of 30 s to give converged statistics.
7. Before digitizing the hotwire signal using an A/D converter, the raw signal is passed through an analogue filter (Krohn-Hite, model 3360 series). Here, the signal is band pass filtered between 5Hz – 5kHz. The choice of value 5Hz is chosen to remove the DC component and the electronic noises, 5kHz is chosen to avoid aliasing.
8. A national instrument DAQ card is used to digitize the acquired signal and a user interface is developed through LabVIEW for storing the data and controlling the wind tunnel speed.

Calibration:

Calibration is performed before each experiment. The probe is placed in the free-stream of the wind tunnel without the aerofoil configuration. The free-stream velocity is varied from 0 – 20 m/s by controlling the wind tunnel motor. The mean voltage for each free-stream speed is noted for further analysis. The free-stream velocity is known from the Pitot-static tube measurements independently. Once the mean voltage (\bar{E}) and the corresponding mean velocity (\bar{U} , from Pitot tube measurement) are known, these are plotted as \bar{E}^2 vs \bar{U}^n . A curve-fit is sought as per King's law (equation 2.4). The value of n is varied from 0.2 to 1.2 in 0.01 increments to fit a linear curve. An optimal value of n is chosen to give an acceptable error in the curve-fit. In general, the n value is obtained to be around 0.4 -0.45. Furthermore from the linear curve fit, the constants A and B are determined.

Temperature correction:

If the ambient temperature varies during the experiment, the output voltage needs to be corrected for possible temperature dependence. To perform this temperature correction, ambient temperature was continuously monitored using a temperature probe and the voltage is corrected using the following expression,

$$E_{corr} = \left(\frac{T_w - T_0}{T_w - T_m} \right)^{0.5} E_a \quad (2.8)$$

where, E_a – acquired voltage; E_{corr} – corrected voltage; T_w – sensor temperature; T_m – ambient temperature during measurement; T_0 – ambient temperature during measurement and calibration.

Probe positioning:

All the probes used in the present investigation were moved inside the tunnel using a 3-axis traverse system which allows independent movement in the streamwise (x), spanwise (z) and wall-normal (y) directions. The smallest step size possible in the streamwise and spanwise directions is 10 μm while that in the wall-normal (y) direction is 1.25 μm . For making near wall boundary layer measurements and to avoid accidental contact of the probe with the surface of the flat plate, the distance between the probe and the wall needs to be known accurately. For this purpose, a laser positioning system is mounted beside the probe arm. In the present study, a wall-normal resolution of 0.1 mm was used throughout the boundary layer and 1 mm was used outside the boundary layer. The closest point of measurement to the

wall had approximately 20% of the free-stream velocity. After this point, the profile was extrapolated linearly to the wall and the shift in the wall-normal direction was determined. The hot-wire probe was not used closer than this location owing to heat transfer between the probe and the wall. This was observed to be present with and without flow as well.

Two point correlation setup:

Two-point spanwise correlations in the boundary layer were measured using two miniature probes. One straight wire probe was fixed at a given wall-normal location and the other boundary layer probe was moved in the spanwise direction to obtain simultaneous velocity measurements at these points. Both the probes were calibrated simultaneously while being at the same wall-normal position. This was confirmed from the mean velocity obtained from their output voltage. The minimum spanwise spacing between the probes was measured manually by visual observation and using rulers. The minimum spacing was noted to be 5 mm. Apart from the initial positioning of the probes, further measurements with various spacings of the probes were performed using the automated traverse mechanism.

Power spectral density calculation:

The frequency content in a time series signal is usually described by plotting the power spectrum. This helps in recognizing the dominant frequencies in the flow field. First, the desired frequency resolution is chosen. In the present study, 5 Hz is chosen as the desired resolution. This value would be sufficient to capture any T-S wave or any low frequency activity present in the flow. For the sampling frequency of 10 kHz and resolution of 5 Hz, the block size of the signal (N_{fft}) can be calculated using the following formula,

$$\Delta f = f_s/N_{fft} \quad (2.9)$$

Thus the signal is divided into several blocks and each block with $N_{fft} = 2048$ (to nearest power of 2) number of samples. Each block of sample is multiplied with a hamming window to reduce spectral leakage. The windowing length is chosen as 1024 implying an overlap of 50% of the windows. Pwelch function in MATLAB was used for performing the spectral analysis using these parameters.

Chapter 3

Transitional intermittency distribution

In this chapter, a new, rational procedure is developed to extract the transition onset, breakdown point and threshold level, which in turn, aids in a more physical determination of intermittency. In addition, the proposed procedure is successfully implemented on the present experiments for intermittency measurements. Further, scaling parameters have been identified which capture the trends as the proximity of the aerofoil is varied in the wall-normal direction.

3.1 Introduction

The intermittency factor (γ), is defined as the fraction of time the flow remains turbulent at a given point in the flow field. The value of the intermittency factor varies from 0 to 1, where a zero value represents a fully laminar region and the value of one represents a fully turbulent regime. The initial idea of intermittency was proposed by [Corrsin \(1943\)](#) to differentiate the turbulent and non-turbulent patterns in axisymmetric turbulent jets and [Townsend \(1948\)](#) made the first intermittency measurements in a turbulent wake. Though the idea of intermittency is derived from fully turbulent flows, its usefulness became prominent in transitional boundary layer research since the discovery of turbulent spots in the transition zone by [Emmons \(1951\)](#). Based on the experimental observation of turbulent spots, [Emmons \(1951\)](#) postulated a theory for intermittency with an assumption that the turbulent spots occur randomly in the flow, which is commonly called ‘continuous breakdown’. Later, [Schubauer and Klebanoff \(1955\)](#) observed the velocity signals obtained from hot-wire measurements on a flat plate, and found that the spots occur suddenly and then they grow gradually in the downstream direction. Such an observation was contrary to the theory proposed by [Emmons \(1951\)](#). Some years

later, [Narasimha \(1957\)](#) proposed a modification to the original assumption made by Emmons about turbulent spot production. He proposed that the breakdown of laminar into turbulent spots on a flat plate was concentrated on a small region (concentrated breakdown) rather than being continuous. Subsequently, the groundwork laid by the intermittency theories proposed by both [Emmons \(1951\)](#) and [Narasimha \(1957\)](#) has led to much debate in transition research. Today, Narasimha's concentrated breakdown theory is widely accepted following validation of his theory by the experimental results of other investigators, who have also, improvised the model for different flows. For instance, [Mayle and Dullenkopf \(1990\)](#) modified Narasimha's intermittency model for unsteady wake boundary layer interaction. [Johnson and Fashifar \(1994\)](#) arrived at an intermittency function with an assumption of linear growth of spots along the streamwise direction. [Ramesh and Hodson \(1999\)](#) improvised the model by incorporating the calming effect and [Fransson et al. \(2005\)](#) verified it for high free-stream turbulence.

Though, several intermittency models have been developed for various flows, the actual measurement of intermittency still remains as a challenge. There are numerous techniques developed by many researchers ([Hedley and Keffer, 1974](#); [Kuan and Wang, 1990](#); [Schneider, 1995](#); [Zhang et al., 1996](#); [Canepa et al., 2002](#); [Falco and Gendrich, 1990](#)) for the definitive measurement of γ . However, the methods proposed in the literature do not seem to work for all type of flows, resulting in no universal procedure for determining γ .

Initially, the procedure followed for the intermittency measurement was quite complex ([Schubauer and Klebanoff, 1955](#); [Narasimha, 1957](#)). It involved photographing the hot-wire signal from the oscilloscope screen and identifying the number and duration of bursts (occurrence of abrupt high frequency peaks in the signal, also considered as turbulent spots; refer to figure [3.1a](#)) in a given period of time. Subsequently, the intermittency can be obtained by taking the ratio of the aggregate duration of the bursts to the total time of the acquired signal. Later, deducing the intermittency was achieved using computer-based methods. [Hedley and Keffer \(1974\)](#) conceived a generic procedure for measuring the intermittency in a fully turbulent boundary layer which has been used as a reference in transitional boundary layer research by many investigators. In general, the intermittency is determined by following a procedure consisting of three sequential steps involving *detector*, *criterion* and *indicator* functions (see figure [3.1](#)). The detector function can be obtained by processing the raw signal to make it easier to discriminate between laminar and turbulent portions in the signal: this is called 'sensitizing' the signal (figure [3.1b](#)).

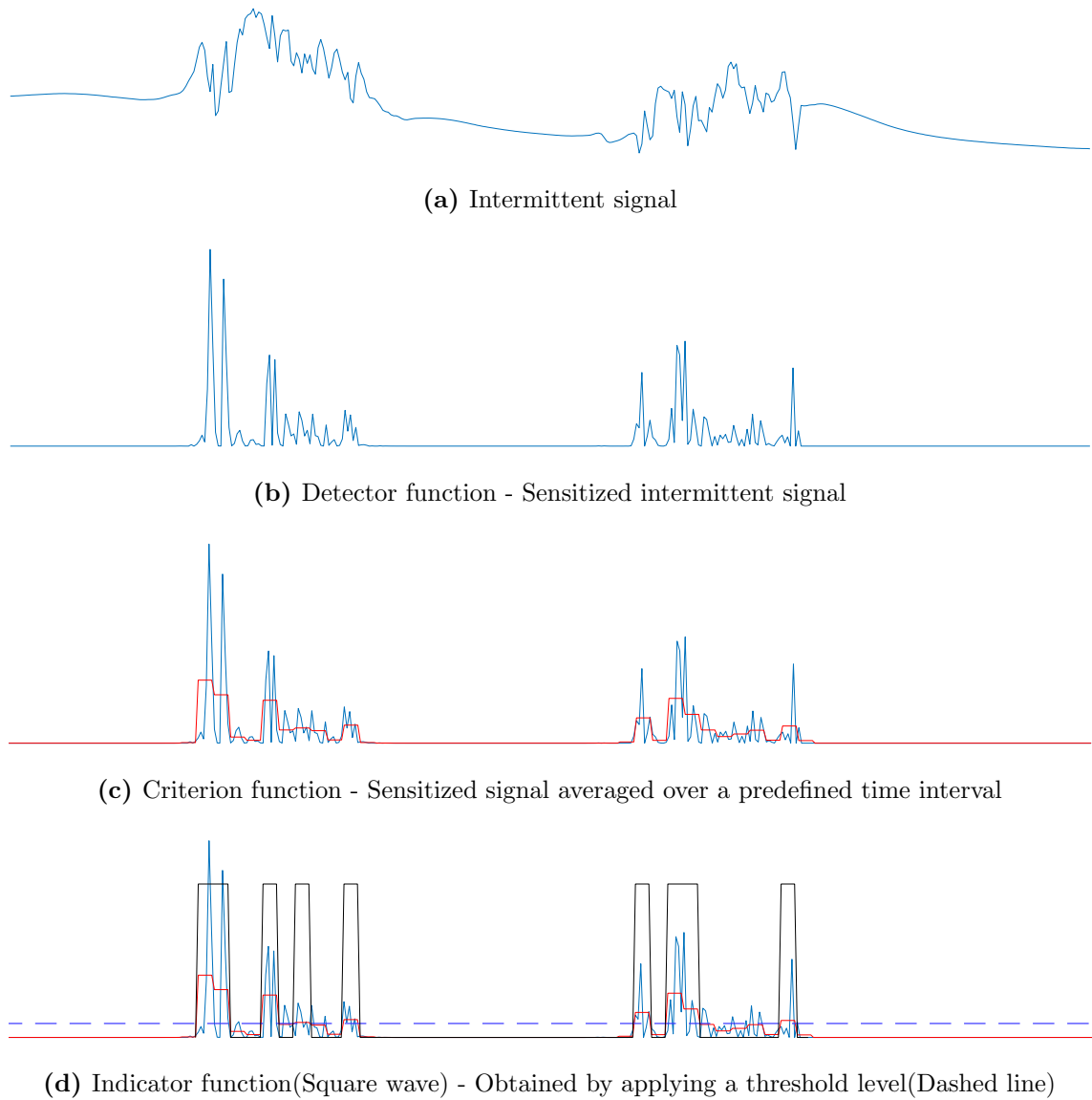


Figure 3.1: General procedure followed to estimate the intermittency function.

In the second step, the criterion function (indicated as a red line in figure 3.1c) is obtained by smoothing the sensitized signal over a predefined time interval (usually of the order of the sampling interval); this is done to avoid the turbulent drop outs and spurious signals (laminar spikes) being taken into account during the analysis. As a next step, a threshold value (T_h) is chosen (technique for choosing this value vary with methods) to detect the presence of turbulent spots in the signal. In any part of the obtained signal, if the criterion function exceeds the threshold value then that region is considered as turbulent, which is indicated by an indicator function, $I(t)$ (black coloured square wave, see figure 3.1d). The indicator function would be assigned a value of 1 for this turbulent condition, else it remains zero. Eventually, by averaging the indicator function over a given period of time, intermittency is

calculated at a point. This is the general procedure followed in many algorithms developed by several researchers for intermittency measurements using hot wires and hot films. Specific details of various functions used in the literature are discussed below.

Firstly, various detector functions proposed in the literature are discussed. Depending on the type of instrumentations and intermittency methods, researchers have employed different detector functions. [Townsend \(1948\)](#) and [Corrsin \(1943\)](#) used the time derivative of the streamwise (u) fluctuating signal, [Hedley and Keffer \(1974\)](#) used the derivative of both the streamwise (u) and wall-normal (v) fluctuating velocity components as the detector function. Further, a variety of detector functions, used by other researchers was discussed in [Hedley and Keffer \(1974\)](#) and it can be observed that the most widely used detector function is the time-derivative of the fluctuation signals. [Falco and Gendrich \(1990\)](#) and [Walker and Solomon \(1992\)](#) used a nonlinear sensitizing technique, on the basis that the amplitude of the fluctuation (u) and its derivative (du/dt) will be large for turbulent signals, and small in laminar regions. Hence, using the product of u with du/dt as the detector function increases the capability for discriminating the laminar and turbulent portions in the signal. Subsequently, [Kuan and Wang \(1990\)](#); [Ramesh et al. \(1996\)](#) and [Jahanmiri et al. \(1991\)](#) used the second derivative of the fluctuating velocity with the motive that higher derivatives will enhance the high frequency (turbulent) components, in turn enabling easier classification.

As similar to the detector function, a variety of predefined time intervals (T_s) has been considered for smoothening the signal. As mentioned earlier, one of the primary ideas for considering the time interval is to avoid the turbulent drop-outs and spurious signals being taken into account for intermittency calculation. In that aspect, the time scale of the eddy associated with the flow will play a major role in deciding the required time interval. A longer time interval T_s may eliminate the short duration bursts (small eddy); on the other hand, choosing a very short time interval may consider the spurious signals into account. So, it is important to select an optimum time interval for smoothening the signals. In this regard, [Hedley and Keffer \(1974\)](#) suggested that an order of 15-35 times of Kolmogorov time scale (T_k) would be an optimum time interval for determining the edge intermittency in turbulent boundary layer. And they have used T_s as $28T_k$, which is equal to 4 times of their sampling time interval (Δt_s). The above choice of the T_s could be optimal for turbulent boundary layers. However, in the case of transitional boundary layers, the eddy size is comparatively larger, which requires the value of T_s to be much

greater than the Kolmogorov scale, (Kuan and Wang (1990)). In this context, many transitional investigators have chosen T_s of the order of 150 - 250 times T_k , which is around 3 to 10 times the sampling interval. For example, Kuan and Wang (1990) and Keller and Wang (1993) have applied $3\Delta t_s$ ($200T_k$), Blair (1992) - $150T_k$, Ramesh et al. (1996) - $5\Delta t_s$, Zhang et al. (1996) - $10\Delta t_s$ and Canepa et al. (2002) used $10\Delta t_s$ ($250T_k$). Another approach followed in choosing T_s in transitional research stems from the convective time of the boundary layer ($t_c = \delta/\bar{U}$). For instance, Fasihfar and Johnson (1992); Hazarika and Hirsch (1995) and Walker and Solomon (1992) have used $2\pi t_c$, $2t_c$ and $0.11t_c$ respectively.

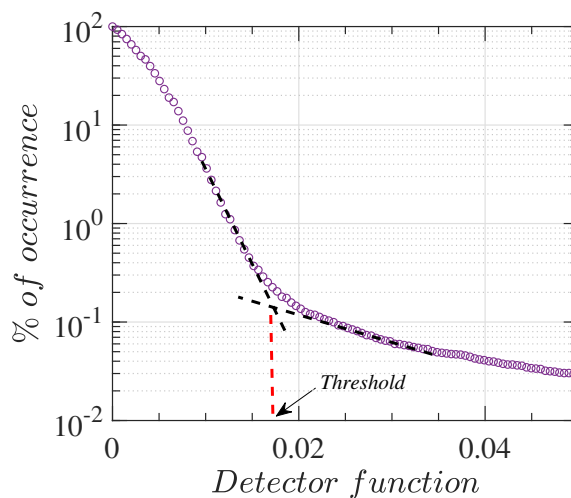


Figure 3.2: Threshold determination technique in dual slope method.

The next step is the determination of the threshold value. Several investigators have proposed different techniques for threshold determination. For example, Kuan and Wang (1990) proposed the idea of the dual slope method to determine the threshold value, which works based on graphical search. In this method, the probability density function (PDF) of the sensitized transitional signal is plotted against the values of the criterion function as shown in figure 3.2. From this plot, they observed two different slopes and the intersection of these two slopes is considered as the threshold value. The above method was successfully used by Ramesh et al. (1996) and Jahanmiri et al. (1991) for two different flow conditions. However, Canepa et al. (2002) mentioned that the identification of two different slopes when applying this method is not always possible, especially towards the end of the transition zone. Similar observation was also noted in the present research and it is discussed in the next section. Also, because of the graphical approach involved in this method, there is a certain level of subjectivity that exists in selecting the threshold value.

Some of the other known intermittency calculation methods in transitional research are the \bar{U} , TERA and MTERA (see equations: 3.1, 3.2, 3.3). The \bar{U} method was introduced by [Shaw et al. \(1985\)](#) with the concept of using a given percentage of the local mean velocity as a threshold. Due to the arbitrariness in choosing the threshold percentage, this method was not well received by other investigators. Turbulent Energy Recognition Algorithm (TERA) developed by [Falco and Gendrich \(1990\)](#) for a fully developed turbulent boundary layer was adapted to determine the intermittency in transitional boundary layer. [Walker and Solomon \(1992\)](#); [Zhang et al. \(1996\)](#) and [Canepa et al. \(2002\)](#) observed that the threshold value determined by the TERA method is very low, which results in very high intermittency in the laminar region. The author has had a similar experience during the present research as well, the results of which are discussed in detail in Section 3.3. To overcome this issue, [Zhang et al. \(1996\)](#) introduced a Modified Turbulent Energy Recognition Algorithm (MTERA) and tested it on a transitional boundary layer over a concave surface. The results obtained from this experiment showed that the intermittency estimates were reasonable and not very sensitive to the constants appearing in the equations (e.g. C_3 in equation 3.3). Further, [Canepa et al. \(2002\)](#) considered several intermittency methods and analysed them to find out the least subjective approach suitable for a hot-film transitional boundary layer investigation.

$$|u| > C_1 \bar{U} \quad (3.1)$$

$$\overline{|u\partial u/\partial t|} > C_2 (u\partial u/\partial t)_{rms} \quad (3.2)$$

$$\overline{|u\partial u/\partial t|} > C_3 (\bar{U}(\partial u/\partial t)_{rms}/(u\partial u/\partial t)_{rms}) \quad (3.3)$$

Despite there being many algorithms for intermittency calculation, none of the methods re found to be robust. This is because of the subjective approaches involved: for instance, the determination of the threshold value is highly dependent on the selection of constants C_1 , C_2 and C_3 in equations 3.1 - 3.3 above, or finding the intersection of two different slopes graphically in the dual-slope method. Moreover, some of the methods proven for particular flow types do not seem to estimate correctly the intermittency in other types of flows. In the present work, a new method is introduced with a more physical approach to estimate the onset of transition and intermittency in the transitional zone. The major differences between the proposed approach and those reported in the literature are (1) the rigorous identification of transition onset and breakdown points and (2) further utilisation of information obtained from those points to determine the threshold value and so estimate the intermittency.

3.2 Determination of transition onset point using Skewness

Determining the location of transition onset is a difficult task. In general, onset is defined as the point where the first turbulent spot occurs. Several methods, such as surface Pitot tubes, hot-wires, surface hot-films, china-clay flow visualisation and other flow visualisation techniques, can be employed to detect the transition onset (x_t) and breakdown points (x_b). Among all of these, the surface Pitot tube and hot-wire methods were considered as more accurate, yet simple methods by [Abu-Ghannam and Shaw \(1980\)](#). Despite the availability of several methods, the point of transition detection is still subjective. For instance, in the hot-wire technique, the point at which the transition occurs is usually determined by observing the fluctuating signal visually. While it is logical to use such an approach, it does not necessarily guarantee an accurate point of transition. As discussed in the introduction of this chapter, an attempt is now made to define a rational technique, which can then be reliably used to detect the transition onset and breakdown points objectively. To achieve this, the concept of skewness parameter is utilised. [Halstead et al. \(1997\)](#) and [Bertelrud \(1998\)](#) have already explored the skewness distribution in the transitional zone of turbomachinery flows and multi-element aerofoils. However, the way they have defined the skewness (third moment normalised with its maximum value, $\overline{u^3}/\overline{u^3}_{max}$) did not identify the onset and breakdown points, rather it just gave the region of transition. To obtain the precise location of those points, the skewness parameter must be defined in a way that the third moment is normalised with the cube of the root mean square of the fluctuating velocity, given by $\overline{u^3}/u_{rms}^3$, such definition is generally followed in turbulent research ([Pope, 2000](#)).

To this end, examples of how the third moment and skewness distributions varied with streamwise location during the current experiments are shown in figure [3.3](#). The corresponding time histories of the velocity fluctuations are provided for selected streamwise locations in figure [3.4](#). Before discussing skewness, let us look at the third moment plot shown in figure [3.3a](#). For convenience, the plot of the third moment can be divided into four regimes: (1) the third moment remains constant up to a certain point ($x/l < 0.1$), (2) it rises and attains a positive peak ($0.1 \leq x/l < 0.2$), (3) it then decays to a negative region ($0.2 \leq x/l < 0.27$), and (4) subsequently reaches a plateau region ($x/l > 0.27$).

Region 1: The average fluctuation of any random noise in the laminar region has to be zero. Consequently, the initial region in figure 3.3a, where the third moment remains at zero can be considered as a laminar region. This observation can be complemented by looking at the time-wise variation of the fluctuating velocity signals shown at different streamwise locations in figure 3.4. In these plots, the actual signal is measured for 30 s here, but for the sake of brevity, it is shown only for 0.5 s. Thus, from the fluctuation signals, it is clear that the flow remains laminar up to $x/l = 0.09$.

Region 2: The fluctuation signal at $x/l = 0.1$ shows the occurrence of bursts which is an indication of turbulence spots. At the same time, it can also be observed from the third moment plot in figure 3.3a that, at $x/l = 0.1$, the third moment starts rising from zero. From these observations, it can be said that any deviation from the initial plateau or flat region of the third moment plot corresponds to the appearance of turbulent spots in the flow leading to transition onset. From the signals downstream of $x/l = 0.1$ in figure 3.4, it can be seen that the spots peak predominantly in the positive direction up to $x/l = 0.2$. This is clearly reflected in the third moment plot until $x/l = 0.2$ and it remains positive.

Region 3: After $x/l = 0.2$, the fluctuations in the velocity signals in figure 3.4 tend to be more evenly split between positive and negative directions. This is reflected by a decrease in the magnitude of the third moment plot as seen in figure 3.3a. As the negative fluctuations begin to dominate, the third moment tends towards an overall negative value.

Region 4: The fourth region ($x/l > 0.27$) sees the third moment settling down in the negative region, as seen in figure 3.3a. The corresponding fluctuating velocity signals show that the flow has become fully turbulent. This observation has been verified in the present research for various experimental measurements made for different geometric and flow conditions. Therefore, it can be concluded that, the regions behind the transition onset, where the third moment tend to reach a plateau can be considered as a fully turbulent flow. The explanation why a negative third moment (and skewness) is seen in the fully turbulent regime can be obtained by looking at some of the previous observations of skewness distribution in the turbulent boundary layer. (Balint et al., 1991; Monty et al., 2011; Harun, 2012)

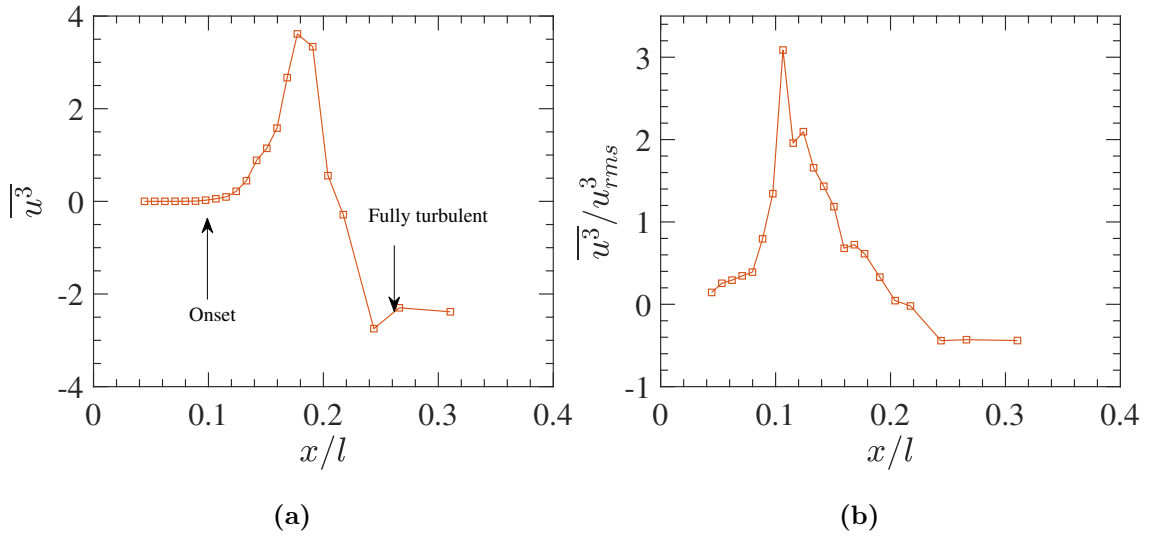


Figure 3.3: Third moment (a) and skewness (b) of the fluctuating signal measured at $y/\delta^* = 0.5$, $h_w = 25$ mm, $x_w/c = 0.25$ & $Re_c = 3.4 \times 10^5$.

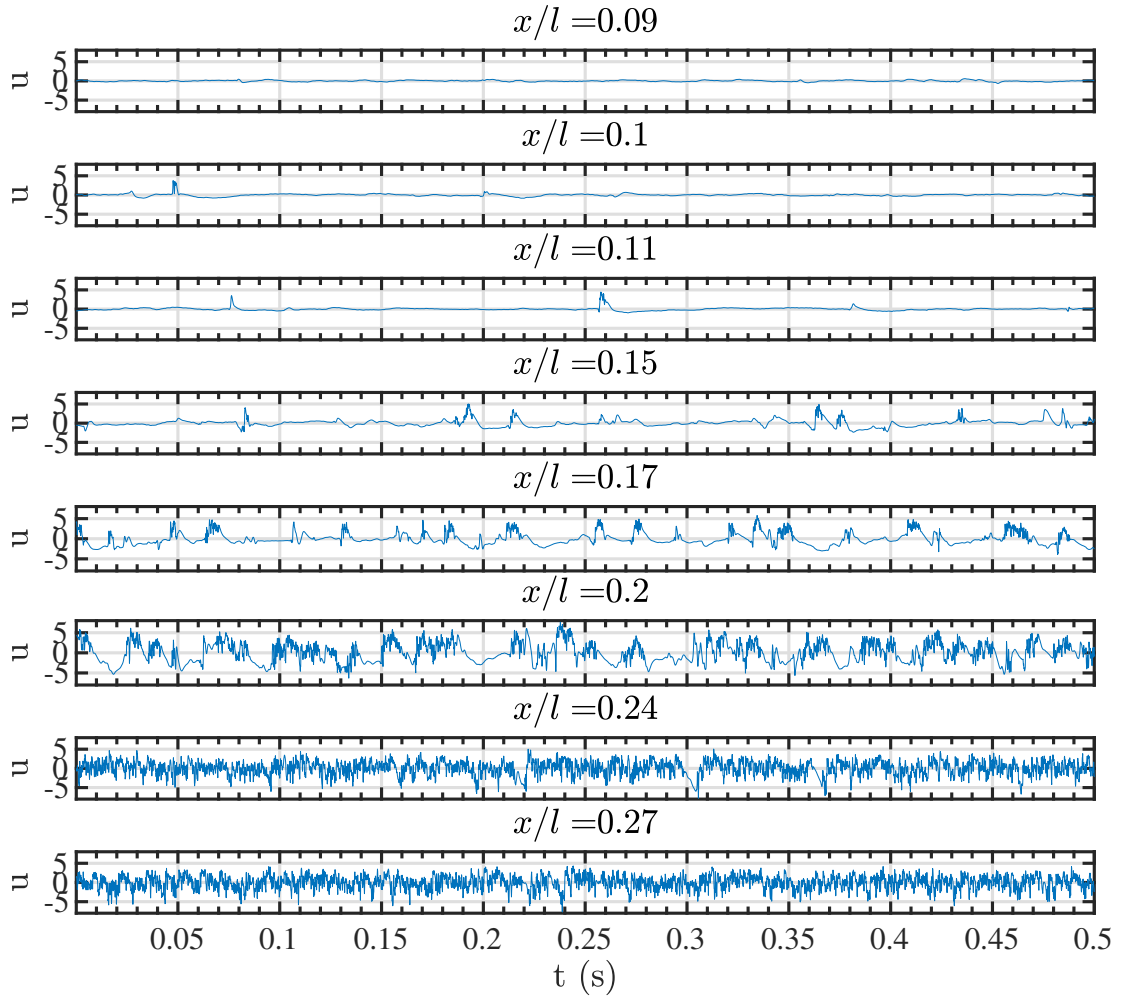


Figure 3.4: Streamwise velocity fluctuation of laminar to turbulent transition, geometry conditions correspond to figure 3.3.

In a zero pressure gradient, fully turbulent flow, [Balint et al. \(1991\)](#) and [Monty et al. \(2011\)](#) have observed that the skewness (and hence the third moment) remains at a non-zero value and that its sign varies across the boundary layer, from positive in the near wall region to negative in the outer region (above the logarithmic layer). Hence, with this understanding, occurrence of negative skewness in the present experiment, especially in the turbulent region ($x/l > 0.27$) can be explained by the fact that this measurement was made at $y/\delta^* = 0.5$, ($y/\delta = 0.17$), which would generally be above the logarithmic layer.

By determining the laminar and turbulent regions from the third moment and velocity-time signal plots, it has become easier to locate the transition zone, which starts at $x/l = 0.1$ and ends at $x/l = 0.27$. However, obtaining the transition onset location from the velocity-time plot is time consuming and prone to human error (*i.e.* failing to notice the spot). Further, it is rather difficult to locate the onset point exactly from the third moment plot. To overcome this issue, the skewness is obtained from the third moment by normalising it with the cube of the u_{rms} . From this skewness plot shown in figure [3.3b](#), it becomes very clear that the point at which the transition onset occurs corresponds to an initial peak in the skewness plot. This is consistent with the corresponding velocity fluctuation signals in figure [3.4](#), where turbulent spots can be observed distinctly at the x/l location corresponding to the skewness peak, *i.e.* $x/l = 0.1$. Similar observation was made by [Gomes et al. \(2015\)](#), where they used surface hot films for obtaining the shear stress signals. They observed that when the skewness parameter with the present definition is used on their signals, the transition onset point occurs around the initial peak of the skewness. Thus, it can be concluded that the definition of skewness used in this work can be effectively used to identify the transition onset point.

The above definition of transition onset point (x_t), obtained from the skewness distribution, was used to help interpret the experimental results obtained for different gaps (between the aerofoil and the plate). Figure [3.5a](#) and figure [3.5b](#) show the third moment and the skewness distribution for various gap heights. By comparing the figures, it is clear the point where the third moment starts to deviate from zero (in figure [3.5a](#)) attains a peak in the skewness (in figure [3.5b](#)). So, the uncertainty involved in choosing the onset point from the third moment distribution is avoided when the skewness plot is used to identify the turbulent onset point (x_t). Thus, in general, it is established that, the peak in the skewness plot corresponds to transition onset. On the other hand, the transition zone can be identified from the initial and final plateau regions of the third moment plot.

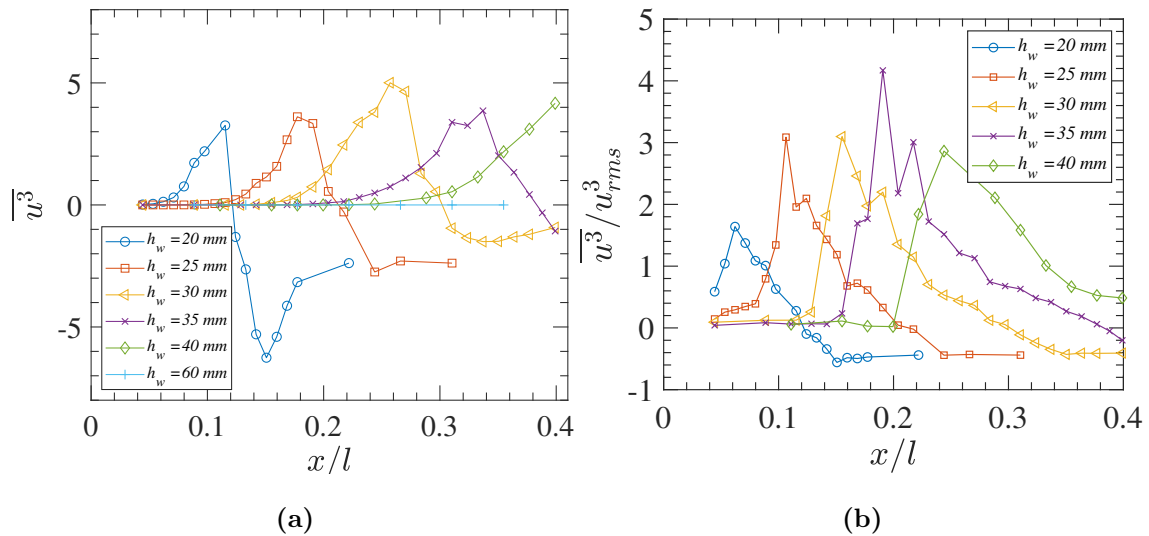


Figure 3.5: Third moment (a) and skewness (b) for various gap measured at $y/\delta^* = 0.5$, $x_w/c = 0.25$ & $Re_c = 3.4 \times 10^5$.

Given that both transition onset and zone length seem to vary linearly with the height of the gap between aerofoil and plate, we now explore whether there is an underlying similarity in behaviour by normalising the abscissa of the skewness distribution with the transition onset location (x_t). The result is shown in figure 3.6. The interesting part of this normalisation is that all the curves collapse onto a single curve, although the curve corresponding to $h_w = 20$ mm does not seem to exactly coincide with the other curves. It can be reasoned that, as the aerofoil wake is very near to the flat plate, transition develops rapidly, leaving only a very short initial disturbance growth region. In addition, as the streamwise measurements are discrete in space, there is a high probability that the onset point would have been missed (given the resolution of 50 mm in the streamwise direction). These considerations might explain why the curve corresponding to $h_w = 20$ mm does not coincide fully with the others. Nonetheless, within the experimental scatter, we can conclude that a scaling effect is present for the skewness distribution with respect to onset location. This scaling also indicates that the transition onset point varies linearly with the position of the wake, which is further confirmed in figure 3.7.

Additionally, the breakdown points obtained from the third moment distribution for three different h_w (20, 25 and 30 mm) are plotted in figure 3.7. Thus, the onset and breakdown points obtained from the skewness and third moment distributions vary linearly with h_w of the aerofoil, but with different slopes. In turn, the length of the transition region appears to be increasing with increasing h_w . These results

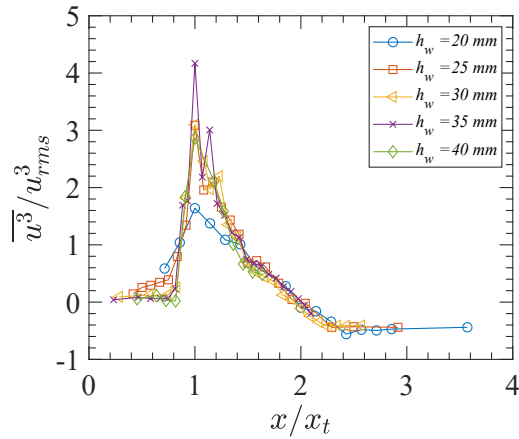


Figure 3.6: Skewness distribution scaled with transition onset point (x_t).

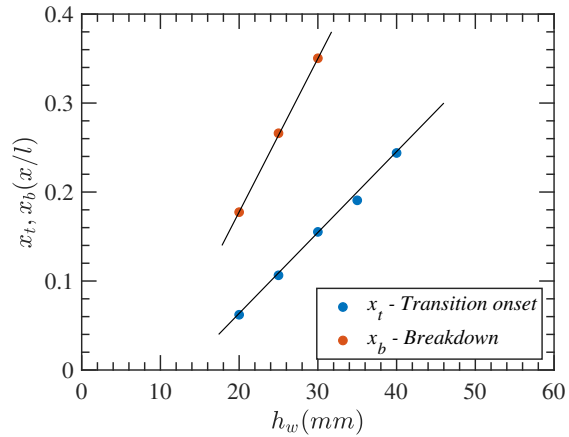


Figure 3.7: Variation of transition onset (x_t) and breakdown (x_b) points.

will also be cross-checked in later sections with the intermittency results.

3.3 A rational method for intermittency measurement

As mentioned in the introduction of the chapter, selection of threshold value (T_h) determines the final step for intermittency estimation. Selection of a lower T_h will indicate greater intermittency in the laminar regime and earlier transition onset in the flow. On the other hand, selection of a higher T_h might indicate that a fully turbulent flow regime is still transitional. Therefore, it is crucial to have an optimum T_h to accurately determine the intermittency. As discussed before, most of the intermittency estimation methods in the literature involved an arbitrary constant or subjective approach to determine the threshold value. In order to check the validity of their threshold choices on the intermittency estimations, three methods, namely, TERA (Walker and Solomon, 1992), MTERA (Zhang et al., 1996) and dual-slope method (Kuan and Wang, 1990), have been tested on the present experimental measurements. The results of this exercise is discussed below.

The results obtained using the TERA and MTERA methods are shown in figure 3.8a and 3.8b. Figure 3.8a clearly reveals the erroneous values and unphysical trend of the intermittency distribution obtained using the TERA method. On the other hand, the MTERA method at least provides a sensible trend of the intermittency distribution, distinguishing the laminar and the turbulent regimes. However,

it can be observed that the intermittency estimations are sensitive to the constants involved. Further, the estimated intermittency values are not consistent with the corresponding fluctuation signals or the skewness distribution. For instance, by observing the corresponding fluctuation signals from figure 3.9, it is clear that the turbulent spots originate around $x/l = 0.16$ and the signal remains intermittent up to $x/l = 0.32$; whereas, the MTERA intermittency suggests that transition onset is in the region $0.09 < x/l < 0.12$ and that the flow remains intermittent up to $0.22 < x/l < 0.28$. So, comparison with the time histories suggests that the intermittency estimated using the MTERA method is also not accurate for the current data set.

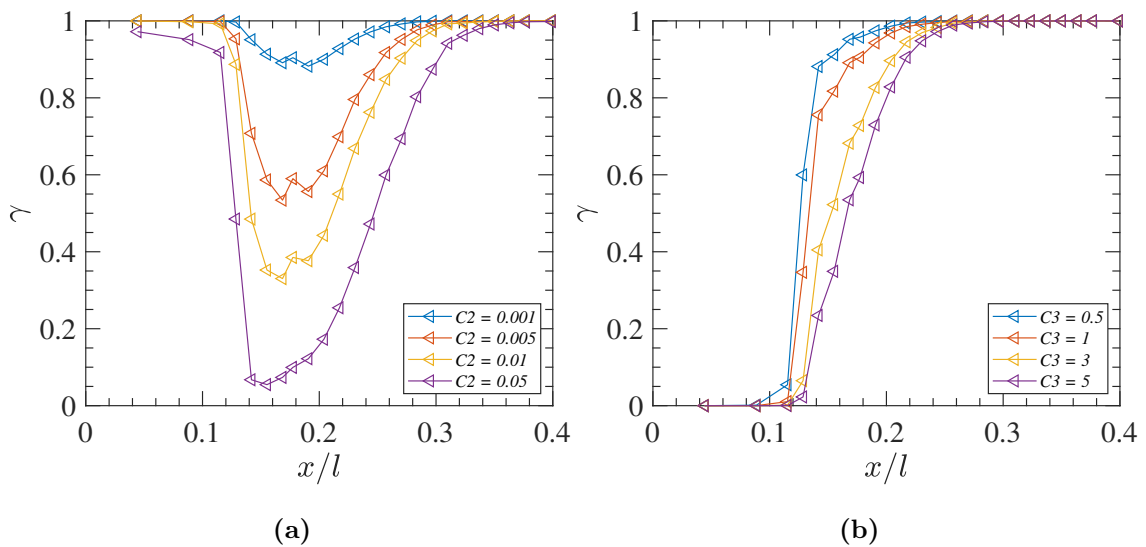


Figure 3.8: Intermittency distribution using TERA (a) and MTERA (b) method for various constant values involved in threshold determination(see equation 3.2 and 3.3). The geometric and flow conditions are $y/\delta^* = 0.5$, $x_w/c = 0.25$, $h_w = 30 \text{ mm}$ & $Re_c = 3.4 \times 10^5$.

Next, the dual slope method (Kuan and Wang, 1990) is applied for the same experimental data as used for TERA and MTERA method evaluation. By following the procedure of the dual slope method in Kuan and Wang (1990), the frequency of occurrence of the detector function is obtained, in which a change in slope was observed. By graphically fitting a straight line on each slope, the threshold value is obtained corresponding to the point of intersection of the two lines.

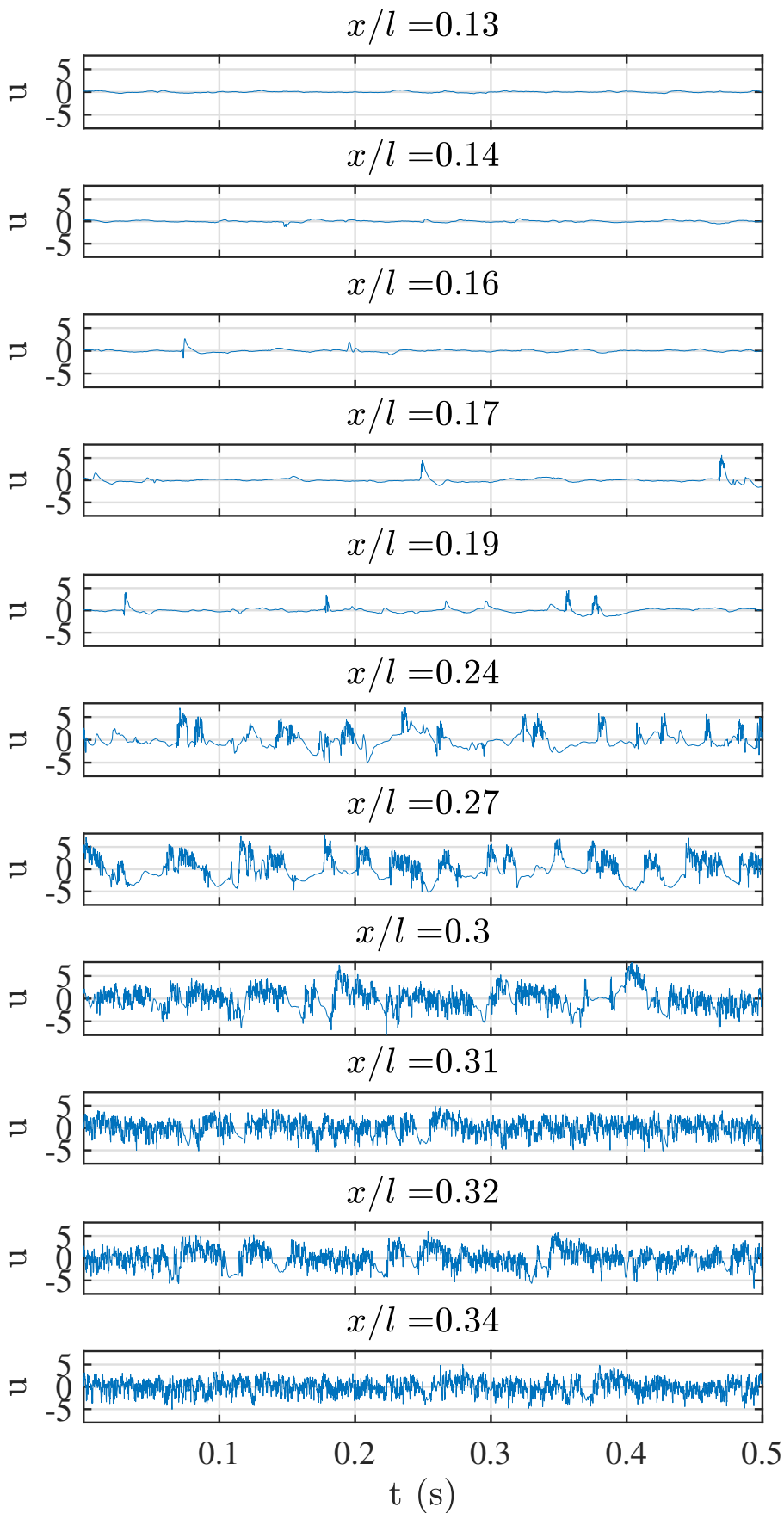


Figure 3.9: Corresponding fluctuating velocity signals of figure 3.8a and 3.8b.

Figure 3.10 shows the frequency of occurrence of the sensitised signals obtained for five different streamwise stations, where the change in slope is noticeable. However, it was very difficult to detect the two different slopes towards the end of the transition zone, which can also be noticed in figure 3.10 at $x/l = 0.31$. Canepa et al. (2002) have also faced the same issue while applying this method on his signals obtained using hot film. Despite this difficulty, from the obtained threshold value, intermittency distribution along the streamwise station is obtained and it is shown in figure 3.11. The trend of the intermittency distribution looks sensible and by comparing with its corresponding fluctuating signal from figure 3.9, it is observed that transition onset and breakdown points determined by this method are practical. However, it is worth to mention that the way the threshold obtained from this method is graphical, which involves subjectivity in choosing the threshold value.

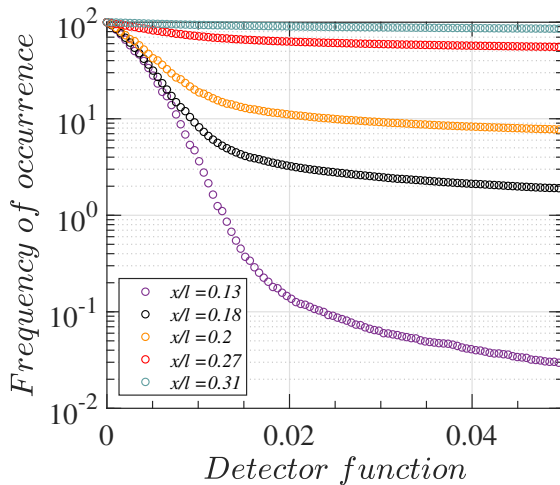


Figure 3.10: Frequency of occurrence of the sensitized signal for various streamwise stations.

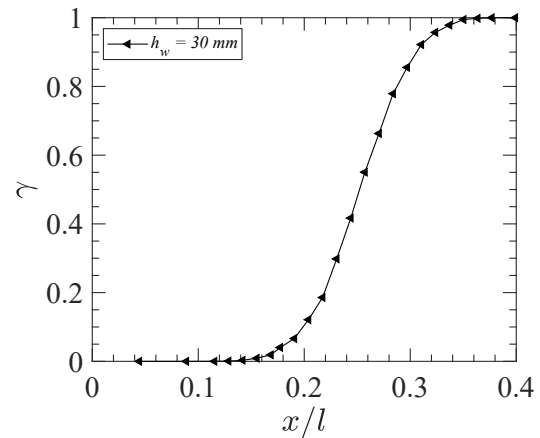


Figure 3.11: Intermittency distribution obtained from dual slope method.

To overcome the subjective selection of the threshold value, an objective approach is introduced with the help of skewness distribution. The basic idea behind this approach is explained in figure 3.12 using the streamwise fluctuating velocity signals obtained at four different points (designated as 1, 2, 3 and 4) on the flat plate whose fluctuating velocity signals are shown by $u_1(t)$, $u_2(t)$, $u_3(t)$ and $u_4(t)$ respectively. The points 1 and 2 are chosen in the upstream region where the flow tends to be laminar, and the points 3 and 4 are from the downstream region of the plate, generally falling in the transition region. It is known that, as the boundary layer thickness increases, then the magnitude of the fluctuations in the flow also increases. This is clearly demonstrated in the fluctuation velocity plots in figure 3.12, where the magnitude of the fluctuation increases from the laminar region to the downstream

end of the transitional zone (from points 1 to 4). It is important to note that the flow remains laminar (points 1 & 2), even in the presence of increasing fluctuations, until we reach point 3 to observe turbulent spots. By observing the locations of the transition onset (point 3) and the mid of transition zone (point 4), it becomes distinctly clear that the perturbations in the laminar flow and the velocity fluctuation due to the turbulent spots are very different. An interesting fact is that the laminar perturbations do not seem to increase in magnitude between the transition onset point (point 3) and the middle of the transitional zone (point 4), in contrast to the increasing amplitude of these perturbations in the laminar region (points 1 & 2). This observation prompts an assumption that the magnitude of the laminar fluctuations remains constant throughout the transition region. In this regard, *it is proposed to choose the magnitude of the laminar fluctuation at the transition onset point as a threshold value for intermittency estimation*. Naturally, it would then be easy to distinguish the turbulent fluctuations from the transitional signals. Such an approach has been adopted and applied to the present measurements to estimate the intermittency. It will be demonstrated that the obtained results look sensible and that the derived intermittency values matches the visual analysis of the fluctuating signal well.

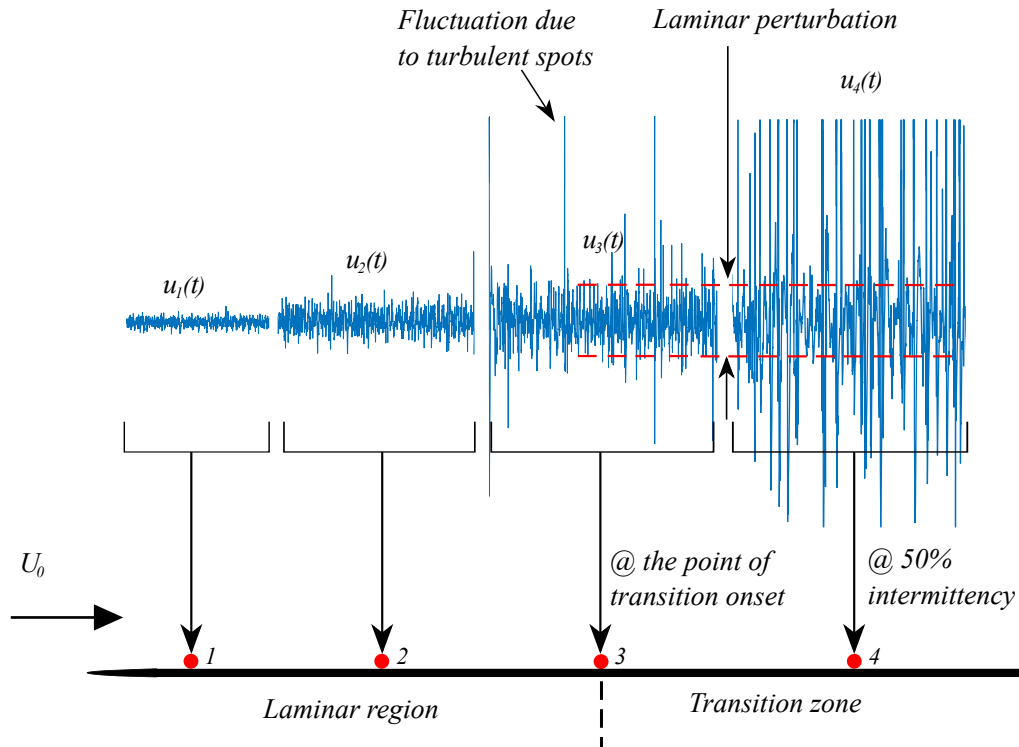


Figure 3.12: An objective approach to choose the threshold value for intermittency estimation (for the purpose of illustration, $u_4(t)$ is sliced at higher end, due to its large magnitude).

Extracting the laminar fluctuations directly from the raw signal is difficult due to the presence of occasional turbulent spots. To overcome this difficulty, a technique used in the dual-slope method is here adopted for sensitizing the flow signals to discriminate between the laminar and turbulent parts. The technique involves double differentiation of the fluctuating velocity signal and further squaring it, $D(t) = (\partial^2 u / \partial t^2)^2$. By doing so, the high frequency fluctuation part alone is sensitized, thus easily differentiating between the laminar and turbulent fluctuations. Once the signal is sensitized, then the *r.m.s* of the sensitized signal ($D(t)_{rms}$) is considered for the selection of threshold value. As proposed earlier, the value of $D(t)_{rms}$ corresponding to the transition onset point is chosen as the threshold value. It is emphasized that the intermittency methods available in the literature have adopted different threshold values at each local streamwise station. Rather here, it is emphasized that a single threshold value corresponding to the onset point is chosen for the entire flow.

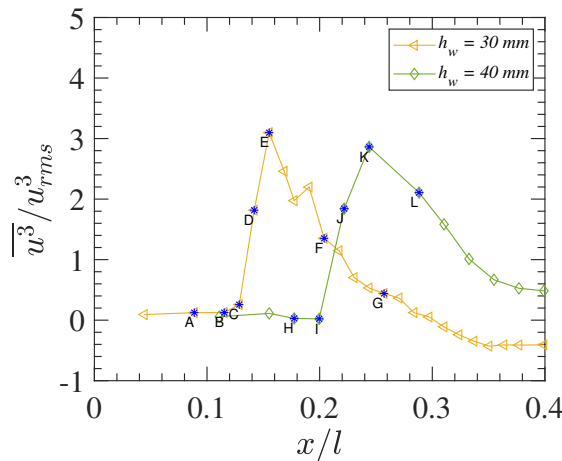


Figure 3.13: Skewness distribution for two different h_w ; $x_w = 0.25c$, $Re_c = 3.4 \times 10^5$ & $y/\delta^* = 0.5$.

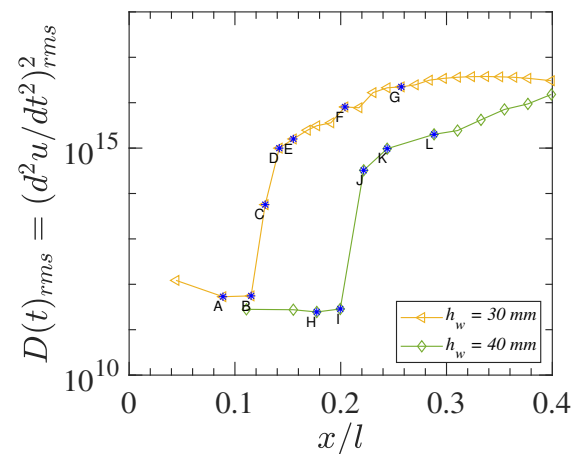


Figure 3.14: $D(t)_{rms}$ along the streamwise station for two different h_w ; Geometric conditions are similar to figure 3.13.

Figure 3.14 depicts the $D(t)_{rms}$ for two different heights, $h_w = 30$ & 40 mm. Our objective is to choose the $D(t)_{rms}$ at the onset points, which would then enable us to select the threshold. From previous section 3.2, the transition onset point can be determined using the skewness distribution plot. The skewness distribution obtained for the two heights are reproduced in figure 3.13, from which we can identify that points “E and K” are the points of onset. Figure 3.14 reveals that the $D(t)_{rms}$ values obtained in the initial laminar region are almost constant whereas, just before

the point of transition onset (points E and K), the value is intensified and increases gradually from there onwards. Eventually, $D(t)_{rms}$ corresponding to the transition onset points (E and K) are chosen as the threshold values.

Before proceeding with the selected threshold, as discussed in the literature, the sensitized signal is averaged or smoothed over the time interval (T_s). It is reiterated that the T_s should be chosen a value between 150 and 250 times the Kolmogorov time scale (T_k). In the present analysis, Kolmogorov time scale is calculated from the turbulent regime, using equation 3.4 (Tennekes and Lumley, 1972) and it is found to be $3\mu s$. The integral time scale (T_I) is calculated by performing an autocorrelation on the acquired fluctuation signal.

$$T_k/T_I \sim Re_t^{-1/2} \quad (3.4)$$

$$Re_t = u_{rms} \times (U_0 T_I / \nu) \quad (3.5)$$

For the present investigation, the signals are acquired at 10 kHz and the smoothing time interval, T_s , has been set as 7 sampling interval, which corresponds to approximately 230 times Kolmogorov scales. Subsequently, the chosen threshold value is applied on the smoothed signal, which in turn yield the indicator function, $I(t)$ given in equation 3.6 & 3.7. Eventually, by integrating the indicator function for the whole signal, the intermittency is determined (equation 3.8).

$$I(t) = \begin{cases} 0, & D(t) \leq D(t)_{rms}|_{x_t} \\ 1, & D(t) > D(t)_{rms}|_{x_t} \end{cases} \quad (3.6)$$

$$(3.7)$$

$$\gamma = \frac{1}{T} \int_0^T I(t) dt \quad (3.8)$$

Reverting back to figure 3.14 for a moment, it is instructive to explore the sensitivity of the estimated intermittency by selecting different threshold values from this figure. All the points marked from A to L have therefore been tested as a potential threshold values in order to verify and validate the proposed idea of choosing the threshold. The intermittency plots corresponding to these trials are plotted in figure 3.15 and 3.16. By observing figure 3.15, we can see that any threshold value chosen in the laminar region (points A & B) results in an erroneous intermittency distribution, wrongly classifying the laminar region as intermittent in nature. On the

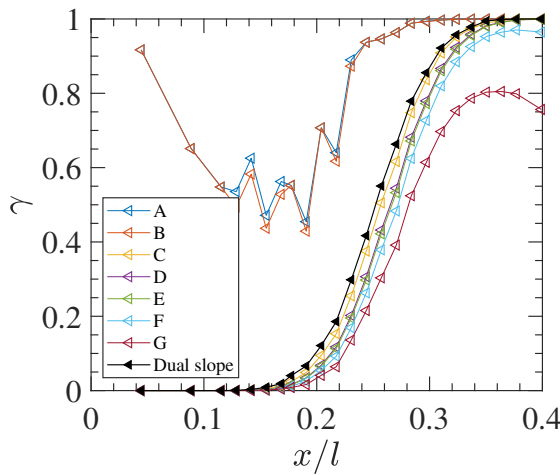


Figure 3.15: Intermittency estimates for various threshold values chosen from $h_w = 30 \text{ mm}$ in figure 3.14.

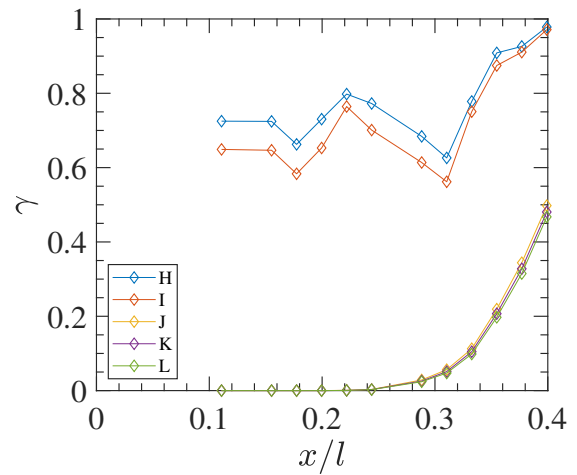


Figure 3.16: Intermittency estimates for various threshold values chosen from $h_w = 40 \text{ mm}$ in figure 3.14.

other hand, the threshold values chosen far from the transition onset location (point F & G) classify the fully turbulent region as intermittent, which is also incorrect. The threshold values corresponding to the region leading up to transition onset, *i.e.* points C – E, all yield a sensible intermittency distribution. This can be verified by comparing the fluctuating velocity signals in figure 3.9 and the intermittency plot of point E, where the whole transition region lies between $x/l = 0.16$ and $x/l = 0.36$. By observing all the points (A-G) in figure 3.15, it is clear that, if a threshold value is chosen at the laminar region or far from the transition onset point, it would give an erroneous intermittency estimation. A threshold value chosen close to the transition onset location would estimate the intermittency more reliably. Similar observations are made with respect to $h_w = 40 \text{ mm}$, shown in figure 3.16. Here the complete transition regime is not captured for $h_w = 40 \text{ mm}$ due to the physical constraints in the measurement domain.

Further, the intermittency distribution obtained from the dual slope method is compared with the proposed method in figure 3.15. It seems that the intermittency values obtained from the dual slope method (black curve) are slightly higher when compared to the intermittency values obtained using the current method (curves C-E). By considering the subjectivity involved in the dual slope method, this variation can be disregarded. The reliability of the proposed method to detect the turbulent spots is demonstrated by plotting the sensitized signal and the indicator function on the same plot in figure 3.17. It can be seen that the indicator function accurately

captures the turbulent bursts, leaving out any spurious laminar spikes. These observations confirm that the proposed idea of choosing the threshold at the transition onset is an effective way to determine the intermittency, performing particularly well for the current experimental data.

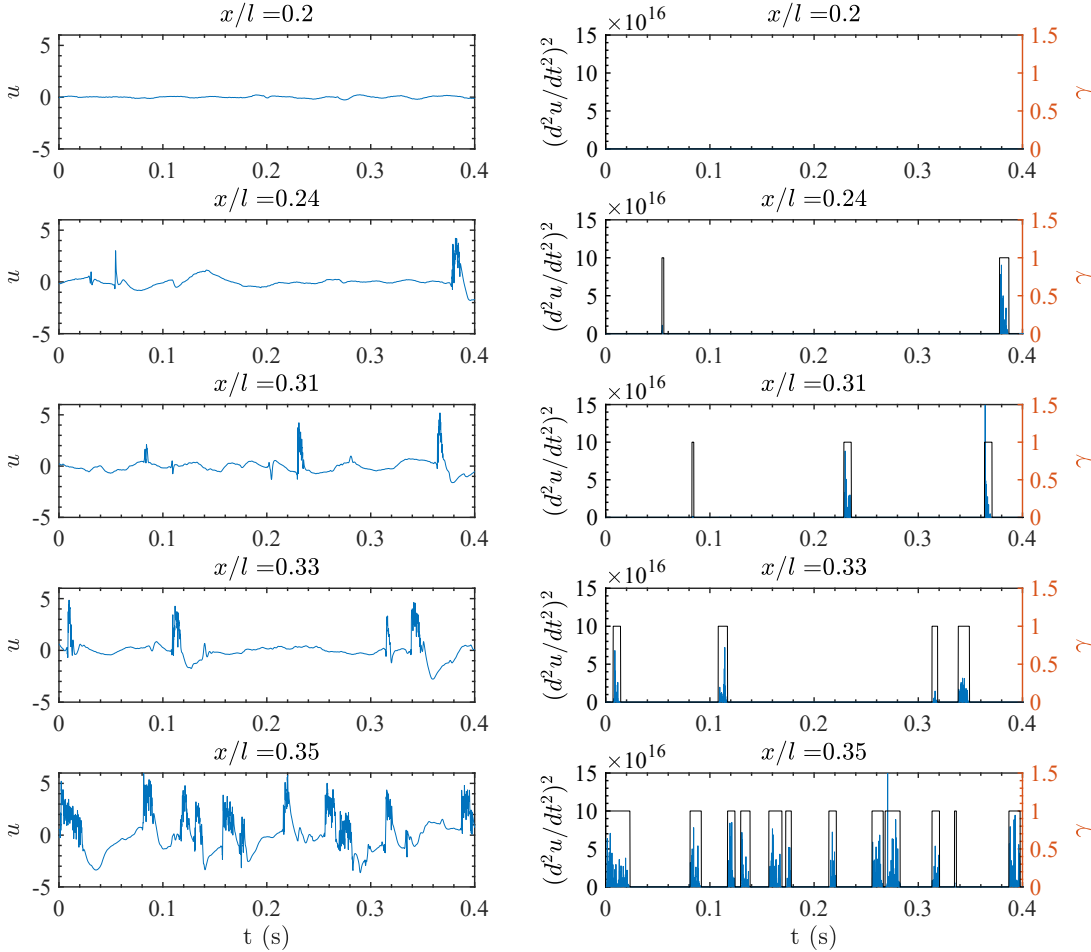


Figure 3.17: Raw fluctuating signal and its corresponding sensitized signal and indicator function (Correspond to $h_w = 40$ mm, figure 3.16).

Having verified the proposed idea, the analysis is extended for different gap heights h_w . As a first step to determine the threshold value, $D(t)_{rms}$ is evaluated and shown in figure 3.18. The figure confirms that the $D(t)_{rms}$ for all h_w follows the same trend as discussed before. Further, as previously with skewness (figure 3.6), an attempt is made to check whether $D(t)_{rms}$ follows the same scaling with x_t . Figure 3.19 reveals that, if $D(t)_{rms}$ obtained at various streamwise stations are normalised with the $D(t)_{rms}$ of onset point, then all the curves seems to collapse onto a single curve. This confirms that, along with the location of transition onset, the fluctuation levels also vary linearly with gap height h_w .

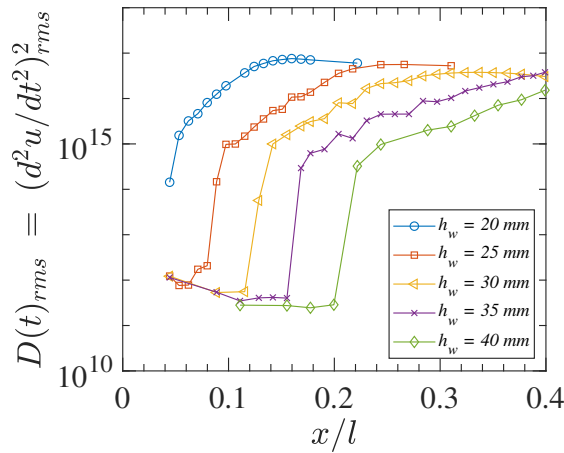


Figure 3.18: T_h along the streamwise station for various h_w .

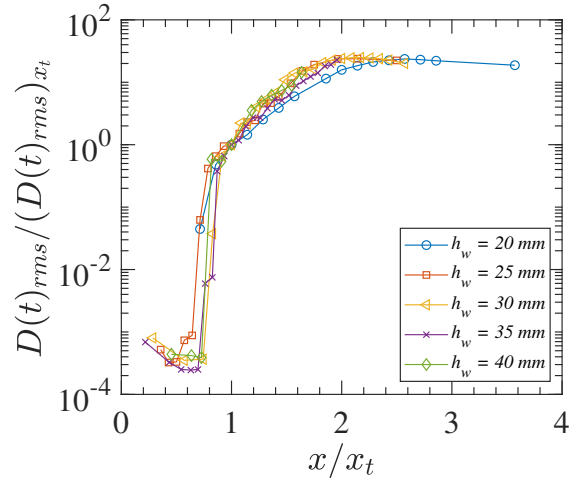


Figure 3.19: T_h scaled with the onset location, x_t .

Finally, the intermittency is determined for various h_w using the threshold value ($D(t)_{rms}$) chosen at the transition onset point. The results obtained are shown in figure 3.20 which explicitly reveal that the increase in h_w shifts the onset location downstream. Also, the intermittency calculations are compared with the intermittency distribution (equation 3.9) obtained using the hypothesis of concentrated breakdown (Narasimha, 1957), which agree fairly well with the present results.

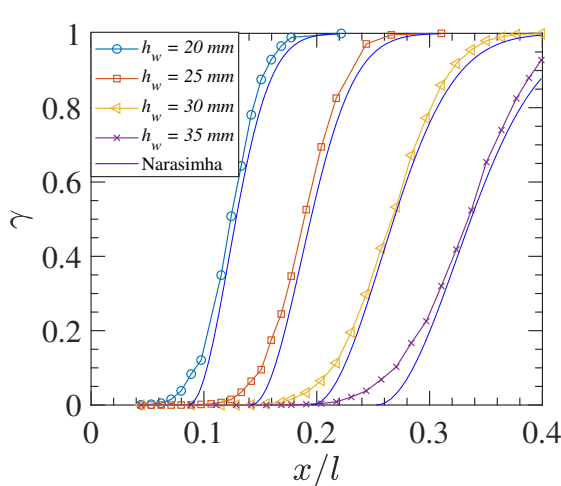


Figure 3.20: Intermittency distribution for various h_w .

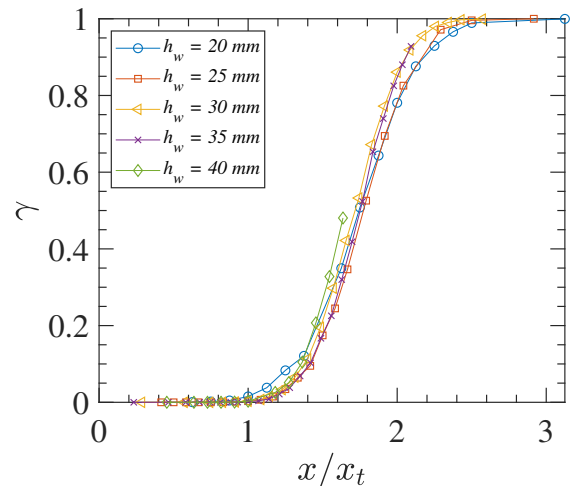


Figure 3.21: Intermittency distribution scaled with x_t .

$$\gamma = 1 - \exp(-0.41\xi^2) \quad (3.9)$$

$$\xi = (x - x_t)/\lambda; \quad \lambda = x(0.75\gamma) - x(0.25\gamma) \quad (3.10)$$

It was shown already that the streamwise distributions of the skewness and $D(t)_{rms}$ scaled with the transition onset points, x_t . It is further observed here that intermittency distribution also scaled with the x_t , as shown in figure 3.21. Another interesting revelation is the length of the transition zone (x_{lt}) also varies linearly with gap (h_w). The length of the transition zone (shown in figure 3.22) is calculated using the onset and breakdown points obtained by interpolating the curves from figure 3.20. Also, it is worth to note in figure 3.22 that the length of the transition zone obtained from skewness and intermittency distribution does not differ much.

The above observations confirm the validity of the idea of determining the transition region from the third moment and skewness distribution. Additionally, the method proposed for the threshold selection perfectly captures the intermittent nature of the flow.

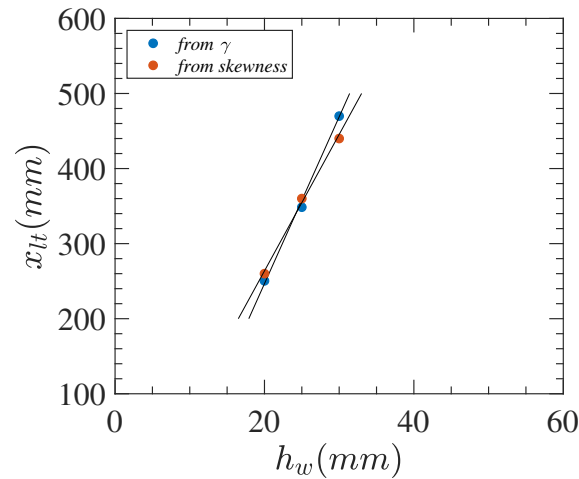


Figure 3.22: Length of the transition zone obtained from intermittency and skewness distribution.

3.4 Summary

Most of the intermittency estimation methods followed in the literature are subjective with some level of arbitrariness in choosing the threshold value. In the present work, a rational and objective technique is adopted to alleviate the shortcomings involved in the other methods. The underlying generic idea is to detect the maximum amount of laminar fluctuation in the transitional flow and further using it as the threshold for determining the intermittency. *The key question lies in how to detect the maximum laminar fluctuation in the transitional flow?* From the observation of the streamwise fluctuation signals along the transition zone (figure 3.12), it is noticed that the magnitude of laminar fluctuation increases along the downstream direction. However, from the point of transition onset, its magnitude does not change much further downstream. Therefore, it can be assumed that the level of laminar fluctuation reaches a maximum at the onset point and remains constant further downstream in the transitional zone. Hence, in the proposed approach, the laminar fluctuation level corresponding to the onset point is chosen as the threshold for determining the intermittency.

At this juncture, another question can be asked: *how to determine the onset point?* And from there, *how to extract the laminar fluctuation alone from the raw signals?* These questions were answered in this chapter by proposing several steps which ultimately helps in estimating the intermittency in a more physical and objective way. Transition onset location is generally determined by visually examining the raw fluctuation signals. The occurrence of an initial burst in the fluctuating signals would be considered as the onset point. Such a visual method might involve error in locating the onset; consequently, *here a method based on the third moment and skewness distribution is proposed to determine the transition onset and breakdown point.* With the proposed approach, we take the third moment of the fluctuating signals, $(\overline{u^3})$ and it is clear from the data that any initial deviation of $(\overline{u^3})$ from zero indicates the onset of transition. Also, it is shown that the point, downstream of transition onset, where the $(\overline{u^3})$ reaches a negative plateau, can be considered as the breakdown point. These measures of onset and breakdown are consistent with the raw time signals.

Nevertheless, accurately locating the deviation of the third moment from zero is rather difficult and subjective. In order to overcome this, the concept of skewness $(\overline{u^3}/u_{rms}^3)$ is utilised, whereby the initial peak of the skewness distribution is proposed to be the transition onset point, which is again consistent with the fluctuating signals for various h_w values (figure 3.5b), for which the location of the peak

skewness correlates well with the onset of transition. An interesting revelation from the study is that the location of the onset points vary linearly with the h_w of the aerofoil, despite the wake thickness and boundary layer thickness grows in $x^{1/2}$.

Knowing the onset location, the next challenge is to extract the laminar fluctuation alone from the signal at the onset point. For this purpose, the flow is first sensitized by double differentiating the fluctuating velocity and further squaring it (as used in [Ramesh et al. 1996](#)). The r.m.s value of the sensitized signal, $D(t)_{rms}$ at the onset point (x_t) is then chosen as the threshold value (T_h). Upon applying the chosen T_h throughout the transitional regime, intermittency is determined (shown in [figure 3.20](#)). It has been shown that the proposed approach to determining intermittency using the threshold value chosen at the onset point is both plausible and consistent with the time history results ([figure 3.17](#)). The intermittency determined using the proposed approach would be even more accurate if the hot wire measurements were obtained very close to the wall or if surface hot film were used for the measurements. The onset and breakdown points determined from the intermittency distribution is consistent with the characteristics of the third moment and skewness distributions. Additionally it is observed, that the skewness and intermittency estimations obtained for various heights of the aerofoil tend to scale with the onset location, (shown in [figure 3.6](#) and [3.21](#)). This confirms that along with the onset point (x_t), the length of the transition zone also increases linearly with increasing gap h_w between the aerofoil and the flat plate.

Chapter 4

Transition due to aerofoil wake-boundary layer interaction

In this chapter, the mechanism of laminar-turbulent transition occurring on a flat plate in the presence of an aerofoil wake is investigated in detail. From the author's literature review, it is believed that this is the first research study conducted using the aerofoil-flat plate setup to investigate the associated transitional characteristics. As no previous studies are available to author's knowledge using such setup, the present experimental results are compared with the characteristics of free-stream turbulence (FST) induced transition and cylinder wake induced transition established in the literature.

4.1 Introduction

From the previous chapter, the determination of intermittency enabled the laminar, transitional and turbulent regimes in the flow to be clearly distinguished. To examine the transition mechanism it is important to analyse, in depth, the pre-transitional region which extends up to the transition onset point (x_t). It is in this zone where the initial disturbance growth occurs which, in turn, determines the type of transition mechanism experienced by the flow. The different regions involved in the transition process are schematically shown in figure 4.1.

The experiments included variation of the Reynolds number and the proximity of the aerofoil with respect to the flat plate, both in the streamwise (x_w – overlap) and the wall-normal (h_w – gap) directions, as listed in table 4.1. By varying these parameters, the most favourable cases for transition analysis were identified as those having a larger initial disturbance growth region, allowing a more for detailed

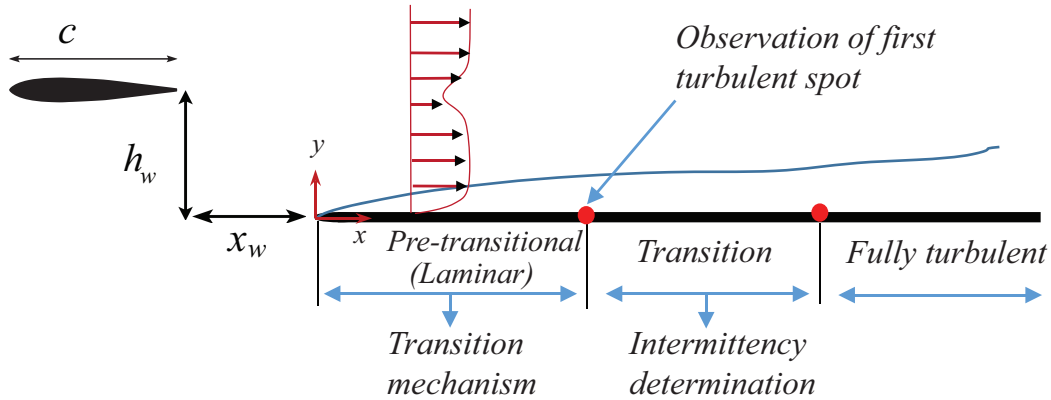


Figure 4.1: Schematic representation of wake-boundary layer interaction and the location of three different zones in the flat plate.

analysis of this part of the flow field. To this end, the results of the experimental investigations are discussed, followed by detailed analysis of the results to identify the transition mechanism.

Case	x_w	h_w (mm)	U_0 (m/s)	Re_c ($\times 10^5$)
Case 1	0.25c	20,25,30,35,40,60,80	5,10,20	0.8,1.7,3.4
Case 2	0.5c	20,40,60	5,10,20	0.8,1.7,3.4
Case 3	0.75c	20,40,60	5,10,20	0.8,1.7,3.4

Table 4.1: Cases measured in the present experiment.

From the intermittency calculations, it is known that the transition onset point corresponds to the peak in the skewness or the deviation of the third moment from zero. In this context, the third moment distributions corresponding to the variations in wall-normal gap (h_w), streamwise overlap (x_w) and Reynolds number of the aerofoil (Re_c) are shown in the figures 4.2 and 4.3. Only a selected number of relevant cases are shown in the figures in order to choose the appropriate case for detailed transition analysis. The effect of varying h_w , for a fixed x_w and Re_c , is shown in figure 4.2. It can be observed that the transition onset point shifts downstream with increase in the height. This is obvious, because if the wake is positioned (in h_w) far from the wall, then the amount of time and distance that it takes to interact with the boundary layer increases, which results in a delayed transition onset.

Figure 4.3a shows the third moment distribution for three different overlaps x_w . The trend of the third moment distribution remains the same as in the previous set of experiments conducted for various gaps. It is clear that, if the overlap between the

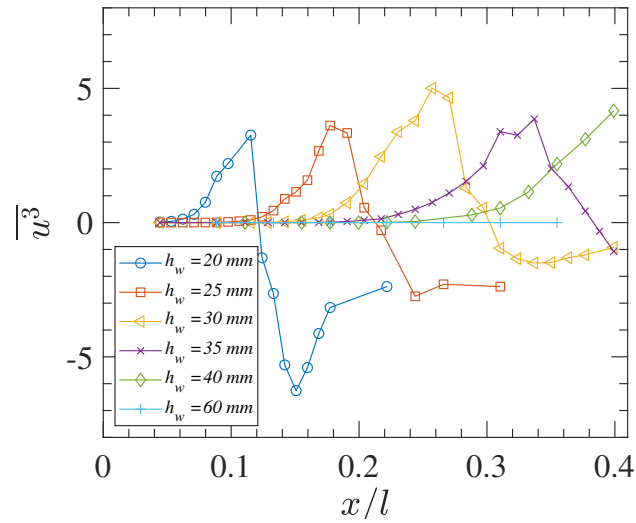


Figure 4.2: Third moment distribution for various h_w measured at $y/\delta^* = 0.5$, $x_w = 0.25c$ and $Re_c = 3.4 \times 10^5$.

aerofoil and the leading edge of the flat plate increases (i.e. as the aerofoil is moved upstream), then there would be an earlier interaction of wake with the boundary layer, which could lead to early transition onset. This is reflected in figure 4.3a, where the red curve shows much earlier transition as compared with the rest of the curves.

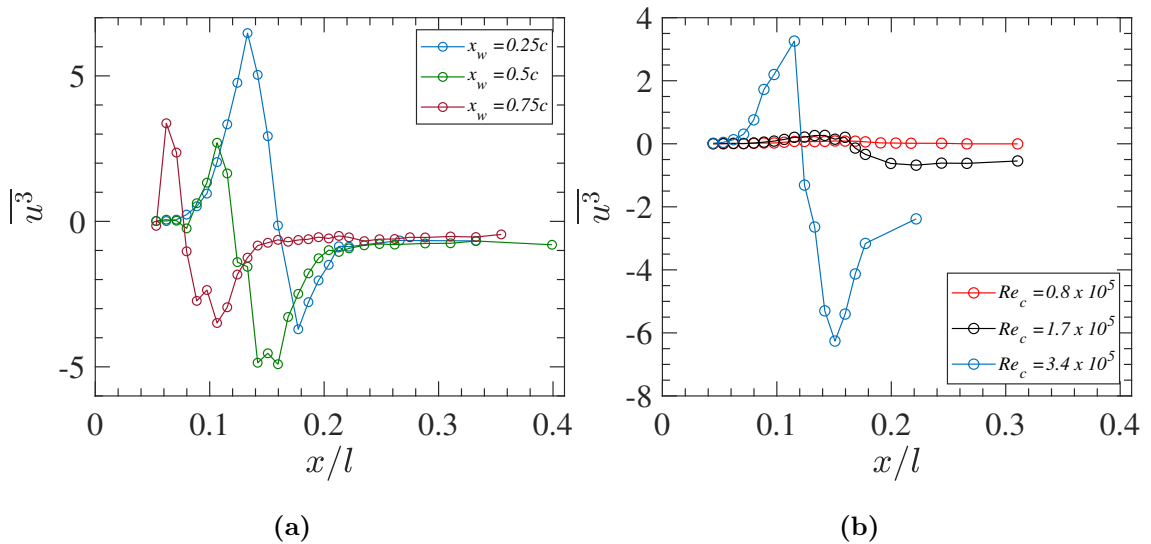


Figure 4.3: Third moment distribution for various x_w and Re_c , measured at (a) $y/\delta^* = 0.4$, $h_w = 20$ mm & $Re_c = 3.4 \times 10^5$ (b) $y/\delta^* = 0.4$, $x_w = 0.25c$, $h_w = 20$ mm.

The effect of Reynolds number on the transition onset is shown in the figure 4.3b. The response of the transition onset to the variation of Reynolds number is

not clearly readable in this figure due to the wide range of $\overline{u^3}$. Nonetheless, it is noted that the onset points for the Re_c of 0.8×10^5 , 1.7×10^5 and 3.4×10^5 are located at x/l of 0.08, 0.07 and 0.06 respectively. Thus, the transition onset occurs earlier with the increase in Reynolds number. This result is expected as the increase in Reynolds number increases the intensity of the fluctuations and hence causes an early instability and transition in the flow.

By observing the third moment plots (figure 4.2 & 4.3) for various h_w , x_w and Re_c , one can identify the favourable values of these three parameters for investigating the transition mechanism. In terms of the overlap, $x_w = 0.25c$ would be appropriate for transition analysis due to the larger initial disturbance growth region. Similarly, for the two gaps, $h_w = 40$ and 60 mm, the length of the initial disturbance growth is larger as compared with that of the other gaps. It is worth noting that for the gap $h_w = 60$ mm, the flow remains laminar and no transition onset is observed, while for $h_w = 40$ mm, the flow goes into the transition zone, but breakdown is not observed in the measurement region of the present experimental setup. Thus, it can be argued that these two stations with larger initial disturbance growth regions are favourable for further investigation of transitional characteristics in the pre-transition zone. From the effect of Reynolds number on the third moment distribution (figure 4.3b), the case $Re_c = 0.8 \times 10^5$ should be chosen. From a practical point of view, it would be advisable to consider a Re_c that is close to the operating Reynolds number in flaps ($Re_c = 9 \times 10^6$, Spaid 2000). However, such high Re_c cannot be achieved due to tunnel limitations. Hence, to have fair representation of high Re_c flow conditions in flaps and to study the transition under such conditions, a tripped aerofoil along with the highest Reynolds number ($Re_c = 3.4 \times 10^5$) achievable in the current wind tunnel setup is used.

Thus, the results corresponding to the following parameters given in table 4.2 are considered for the detailed transition analysis. At few instances in this chapter, some results corresponding to additional values of gap and Reynolds number are used in order to elucidate in detail the underlying transitional characteristics.

h_w (mm)	x_w	Re_c
40, 60	0.25c	3.4×10^5

Table 4.2: Cases considered for analysis.

4.2 Transitional characteristics

In this section, the laminar-turbulent transitional characteristics of the wake-boundary layer interaction are examined in detail. The skewness distribution for the gaps $h_w = 40$ and 60 mm are shown in figure 4.4 from which the pre-transitional zone can be identified. In this region, the transition behaviour is investigated through detailed analysis of mean velocity fluctuation profiles, energy distribution, spectral characteristics and coherent structures. The results of the analyses are presented below.

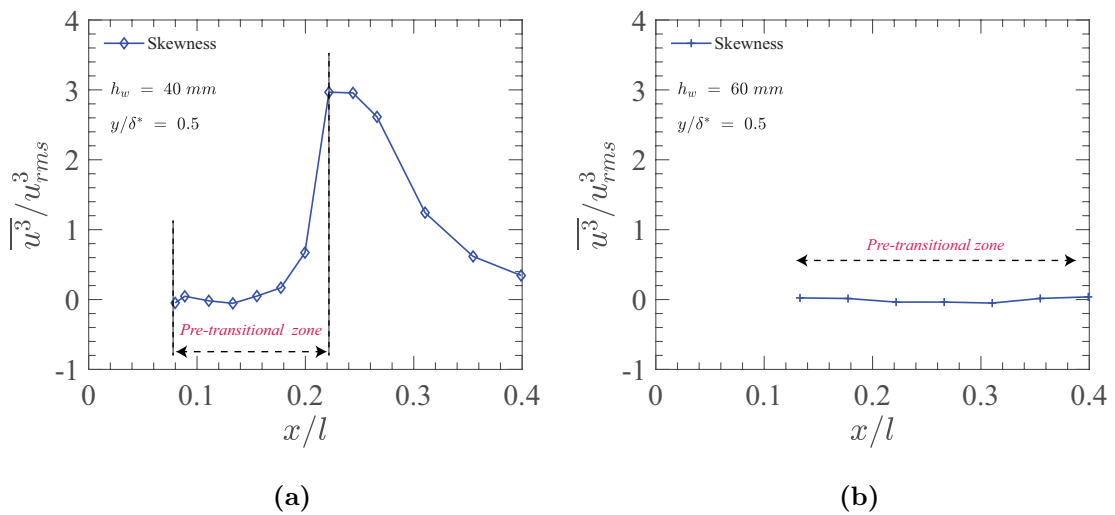


Figure 4.4: Skewness and third moment for (a) $h_w = 40$ mm and (b) $h_w = 60$ mm.

4.2.1 Mean velocity profile

Mean velocity profiles for two different h_w cases are shown in figure 4.5. Velocity profile measurements are carried out from the near-wall region up to various points. From the profile shown in figure 4.5, it can be observed that a potential core exists between the wall boundary layer and the wake. This implies that no mean shear layer exists in this region. Since the primary focus is on the receptivity and transition mechanism in the boundary layer, the region above the potential core is not considered in the present study. In particular, the disturbance growth in the boundary layer is examined closely.

For the case with $h_w = 40$ mm, the probe was moved in the wall-normal direction in steps of 0.1 mm. However as discussed above, it was deemed that such fine step size is not necessary especially above the potential core. Thus, for the gap of 60 mm, the step size of 0.1 mm was used up to the middle of the potential core above which a

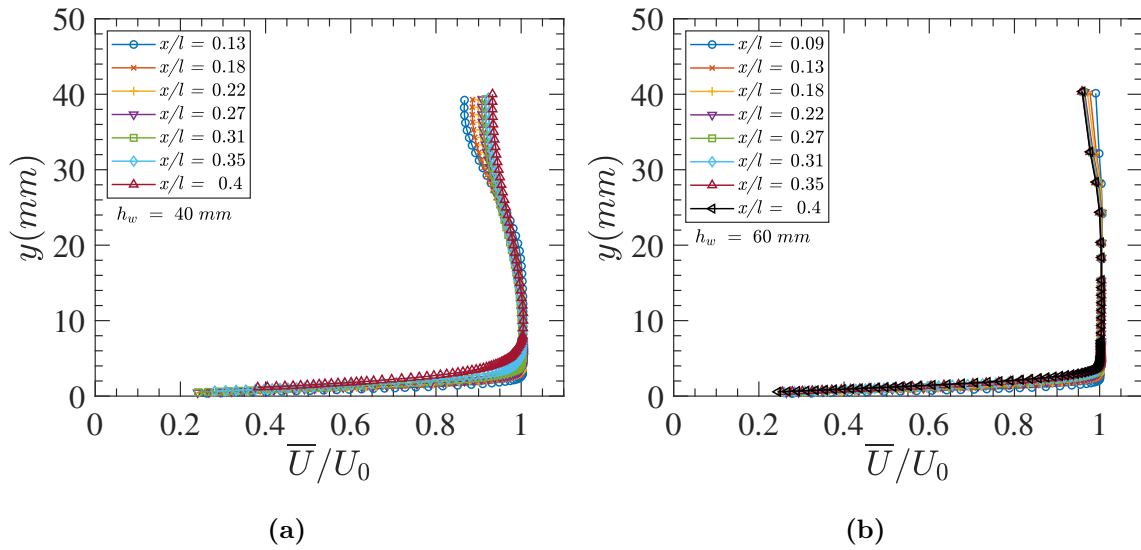


Figure 4.5: Mean velocity profile for (a) $h_w = 40$ mm and (b) $h_w = 60$ mm.

larger step size (5 mm) was used. The closest point of measurement to the wall had approximately 20% of the free-stream velocity, afterwards the curve is extrapolated linearly to the wall and the shift in the wall-normal direction is determined.

Throughout the present study, boundary layer thickness (δ) is calculated using the traditional 99% of the freestream velocity approach (height at which $u = 0.99U_0$). Such an approach is sufficient due to the existence of a potential core between the boundary layer and the wake despite the presence of a confluent boundary layer. Displacement thickness (δ^*) and momentum thickness (θ) are then calculated by integrating the velocity profile based on equations 4.1 and 4.2. The shape factor ($H = \delta^*/\theta$) is found by taking the ratio of the displacement thickness to the momentum thickness. All of the above boundary layer parameters obtained for $h_w = 40$ and 60 mm are given in table 4.3 and 4.4.

$$\delta^* = \int_0^\delta \left(1 - \frac{\bar{U}}{U_0}\right) dy \quad (4.1)$$

$$\theta = \int_0^\delta \frac{\bar{U}}{U_0} \left(1 - \frac{\bar{U}}{U_0}\right) dy \quad (4.2)$$

Before focussing on the transition mechanism, the mean velocity profile of the boundary layer region needs to be considered. Boundary layer profiles for $h_w = 40$ and 60 mm corresponding to various streamwise stations ranging from $x/l = 0.13$ to 0.4 are plotted below along with the Blasius profile. Figure 4.6 shows the mean velocity profile for $h_w = 40$ mm. By looking at the trend of the curves, it can

be clearly seen that the boundary layer profile is gradually deviating from laminar towards turbulent. Such an observation is also reflected in the skewness plot for $h_w = 40$ mm in figure 4.4a, where it was noted that transition onset occurs at $x/l = 0.22$.

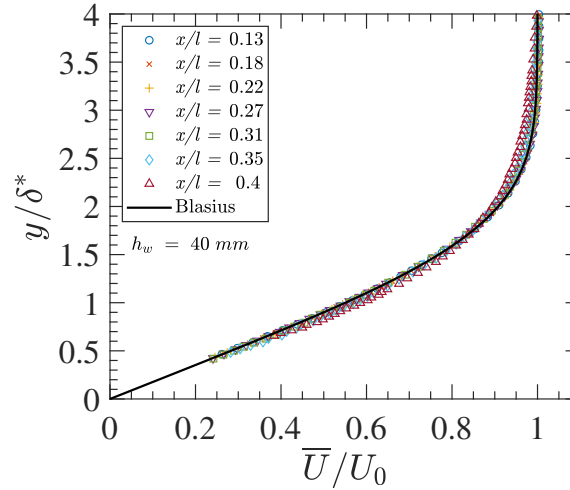


Figure 4.6: Boundary layer profile for $h_w = 40$ mm, in both pre-transitional and transitional zone.

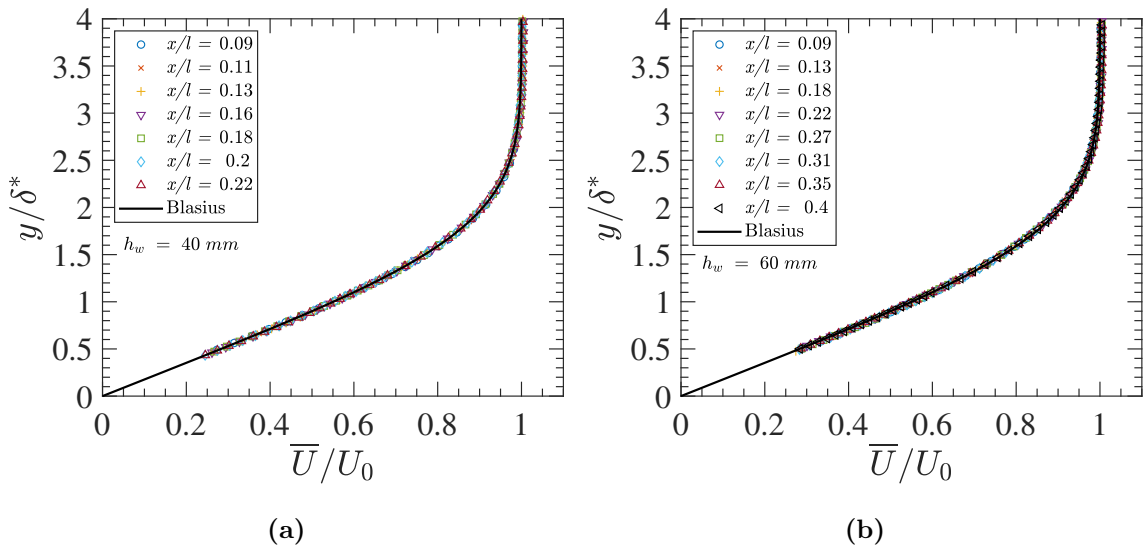


Figure 4.7: Boundary layer profile for (a) $h_w = 40$ mm and (b) $h_w = 60$ mm in the pre-transitional zone.

Figure 4.7a shows only the mean velocity profiles prior to the transition point. This clearly illustrates that the flow in the pre-transition region i.e., $x/l < 0.22$ remains laminar as the mean velocity profiles matches well with the Blasius solution. A similar observation can also be made for the gap $h_w = 60$ mm for which the mean

velocity profiles are plotted together with the Blasius profile in figure 4.7b. This is expected as the transition did not occur within the measurement domain for the gap, $h_w = 60$ mm, hinted by the corresponding skewness distribution in figure 4.4b.

By examining the boundary layer profiles for both the gaps, it appears that the wake disturbance interacting with the boundary layer would be low in magnitude which results in no discernible effect on the mean velocity profile. This can further be confirmed from the values of the boundary layer parameters shown in table 4.3 and 4.4. For the pure Blasius case, the shape factor (H) is equal to 2.59. From the table, it is clear that the shape factor calculated for the present profiles prior to the transition onset matches well with that of the Blasius solution. In addition, the normalised displacement and the momentum thicknesses corresponding to the Blasius solution are constants and are equal to 1.72 and 0.664 respectively as given in equations 4.3 and 4.4. For the case of $h_w = 40$ mm (table 4.3), the normalised values of δ^* and θ match reasonably well with that of the above Blasius values. In the case of $h_w = 60$ mm (table 4.4), only the normalised values of θ match with that of the Blasius, δ^* is slightly decreased, nevertheless it remains fairly constant in the streamwise distance and the value of shape factor is not affected. Further, for Blasius profiles, the boundary layer thickness and the displacement thickness grow as $x^{1/2}$, which is confirmed for the present measurements as shown in figure 4.8.

$$\delta^*/\sqrt{\nu x/U_0} = 1.72 \quad (4.3)$$

$$\theta/\sqrt{\nu x/U_0} = 0.664 \quad (4.4)$$

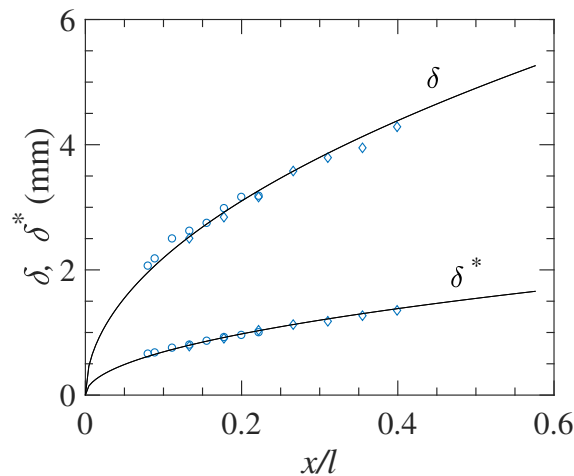


Figure 4.8: Growth of the boundary layer thickness and displacement for $h_w = 40$ (circle) and 60 mm (diamond).

x (mm)	x/l	δ (mm)	δ^* (mm)	θ (mm)	H	Re_{δ^*}	$\delta^*/\sqrt{\nu x/\bar{U}_0}$	$\theta/\sqrt{\nu x/\bar{U}_0}$
250	0.11	2.50	0.75	0.29	2.59	1015	1.74	0.67
300	0.13	2.62	0.80	0.31	2.58	1083	1.70	0.67
350	0.16	2.75	0.86	0.33	2.60	1164	1.70	0.66
400	0.18	2.99	0.93	0.36	2.58	1259	1.71	0.65
450	0.20	3.17	0.96	0.37	2.59	1299	1.66	0.64
500	0.22	3.19	1.00	0.39	2.56	1353	1.65	0.64

Table 4.3: Boundary layer parameters for $h_w = 40$ mm; $x_w = 0.25c$; $U_0 = 20.3$ m/s & $Re_c = 3.4 \times 10^5$.

x (mm)	x/l	δ (mm)	δ^* (mm)	θ (mm)	H	Re_{δ^*}	$\delta^*/\sqrt{\nu x/\bar{U}_0}$	$\theta/\sqrt{\nu x/\bar{U}_0}$
300	0.13	2.50	0.78	0.30	2.60	920	1.66	0.66
400	0.18	2.84	0.90	0.35	2.57	1218	1.66	0.64
500	0.22	3.16	1.02	0.39	2.61	1380	1.68	0.64
600	0.27	3.58	1.12	0.43	2.60	1516	1.68	0.65
700	0.31	3.80	1.17	0.45	2.60	1583	1.63	0.63
800	0.35	3.95	1.27	0.49	2.59	1719	1.65	0.64
900	0.40	4.29	1.35	0.52	2.59	1827	1.66	0.64

Table 4.4: Boundary layer parameters for $h_w = 60$ mm; $x_w = 0.25c$; $U_0 = 20.3$ m/s & $Re_c = 3.4 \times 10^5$.

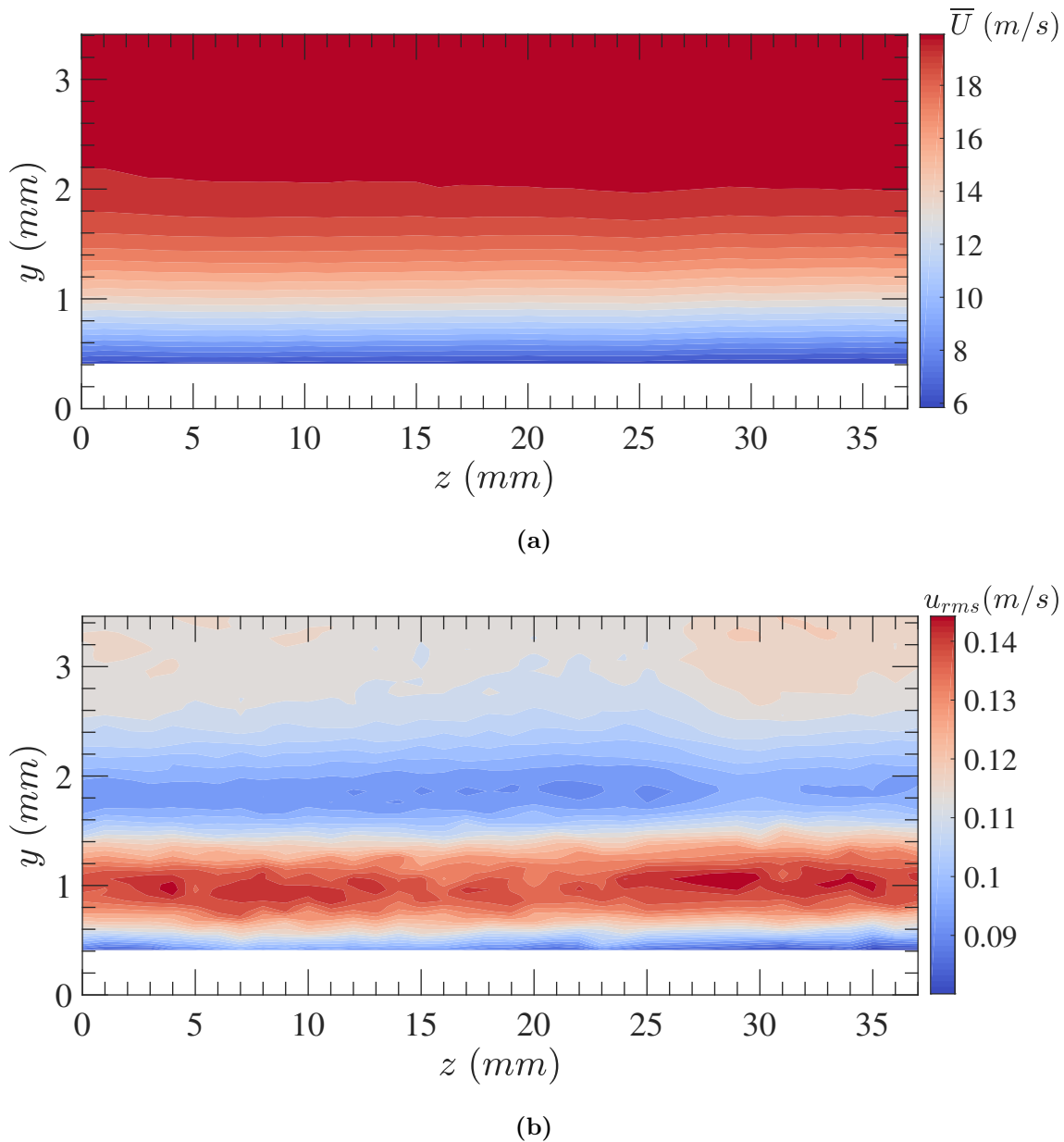


Figure 4.9: Spanwise distribution of streamwise (a) mean velocity and (b) fluctuation velocity measured at $x/l = 0.13$ for $h_w = 40$ mm.

To examine the spanwise variation of the streamwise velocity, a contour plot of the mean velocity is obtained in the $y - z$ plane and it is shown in figure 4.9a. The figure confirms a uniform distribution of mean velocity in the spanwise direction, thus leaving the Blasius profile undisturbed. Further, in the same plane, root mean square of the streamwise fluctuation velocity (u_{rms}) is obtained (shown in figure 4.9b), which shows that the fluctuation velocity possess a non-uniform distribution in the spanwise direction. To elucidate the characteristics of perturbation velocities in the streamwise and spanwise directions, further analyses are carried out in the below sections.

4.2.2 Fluctuating velocity

To gain further insights into the transition mechanism, the disturbance growth is analysed by looking at the fluctuating velocity signals. As a first step, for the case of $h_w = 40$ mm, the wall-normal distribution of the turbulent intensity (T_u) is plotted in figure 4.10 for various streamwise stations. Here, turbulent intensity is defined as the root mean square (*rms*) of the streamwise fluctuating velocity normalised with the local mean velocity. Further, the streamwise stations considered in figure 4.10 include the locations corresponding to both the pre-transitional ($x/l < 0.22$) and transition regions ($x/l > 0.22$).

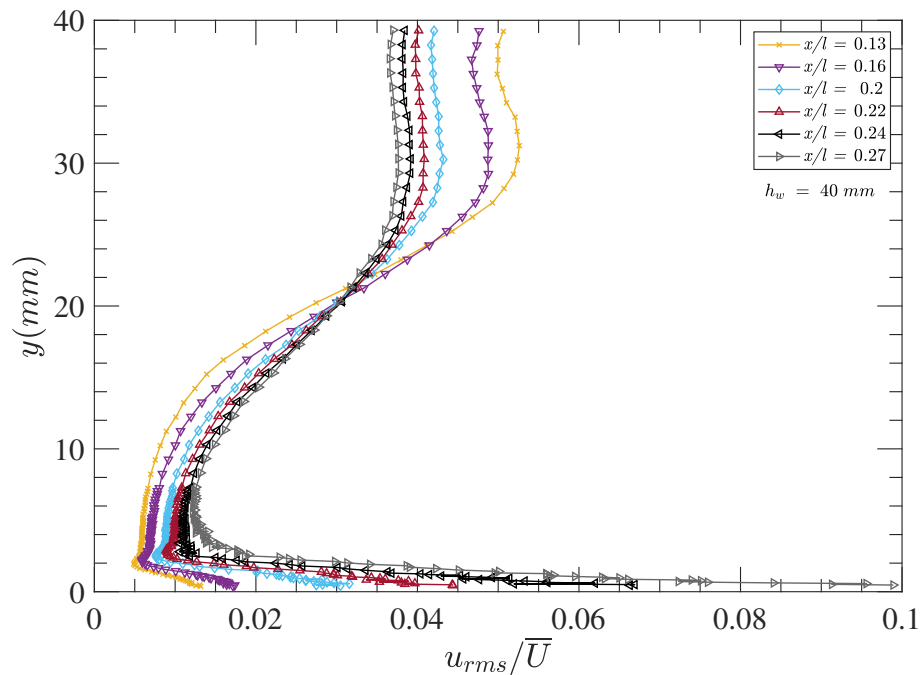


Figure 4.10: Turbulent intensity across the wall-normal direction for various streamwise station at $h_w = 40$ mm.

From the plot, two distinct observations can be made w.r.t. the turbulence level. Firstly, by looking at the turbulence level in the wake region (in the present case, the wake core is located at $y = 40$ mm), it can be noticed that the turbulent intensity decreases with downstream distance. This can be attributed to the decreasing wake defect velocity as it spreads downstream. On the other hand, near the edge of the boundary layer (around $y = 2-4$ mm), turbulence intensity increases with increase in x/l . For instance, at $x/l = 0.11$, near the edge of the boundary layer, T_u is less than 0.5% and then increases beyond 1% further downstream. This is due to the fact that both the boundary layer thickness and the wake thickness grow downstream resulting in a reduced potential core. This, in turn leads to stronger interaction of

the wake disturbance with the boundary layer, resulting in an increasing turbulence level near the edge of the boundary layer. It is important to notice a key difference between the interaction of the disturbance with the boundary layer in the present case and in the case of FST- induced bypass transition. In particular, in the FST case, the disturbance or the turbulence intensity in the free-stream decays downstream (Jacobs and Durbin, 2001; Balamurugan and Mandal, 2017), which results in a decreased forcing of the disturbance in the downstream of the boundary layer. On contrary, in the present case (from figure 4.10), the disturbance forcing into the boundary layer increases with downstream distance, presumably due to the increasing wake thickness (and therefore proximity to the boundary layer) and in turn, stronger wake/boundary layer interaction. In the case of FST induced transition, the general reference value of free-stream turbulence is usually measured in front of the leading edge of the plate (which is the maximum T_u), whereas in the present case of wake-boundary layer interaction as discussed above, the ‘free-stream’ value increases locally, in the streamwise direction. Hence, it would be logical to consider a local reference value for the turbulence level, with the values chosen at various streamwise locations corresponding to the edge of the local boundary layer.

Despite the differences between the two cases, some of the characteristics of FST-induced bypass transition are observed in the present work. So, it is worth comparing the present results with the characteristics of FST-induced bypass transition, as well as against the characteristics of cylinder wake boundary layer interaction, to explore the differences in the associated transition mechanisms.

A closer look at the streamwise fluctuation profiles (u_{rms}) inside the boundary layer is shown in figure 4.11 for the cases $h_w = 40$ and 60 mm. Free-stream velocity (U_0) and local boundary layer thickness (δ) are used as normalising parameters to demonstrate the disturbance growth in the streamwise direction and within the boundary layer. In both cases (figure 4.11a & 4.11b) the disturbance amplitude clearly increases in the downstream direction throughout the boundary layer. Further, the presence of both a maximum and a local minimum disturbance magnitude can be seen. For both $h_w = 40$ and 60 mm, the maximum ($u_{rms,max}$) occurs around $y/\delta = 0.4$ (or $y/\delta^* = 1.3$) and its position remains constant throughout the pre-transitional zone. The local minimum lies further out, above $y/\delta = 0.7$, and its location moves towards the edge of the boundary layer in the downstream direction, which is marked as a black dashed line in both figure.

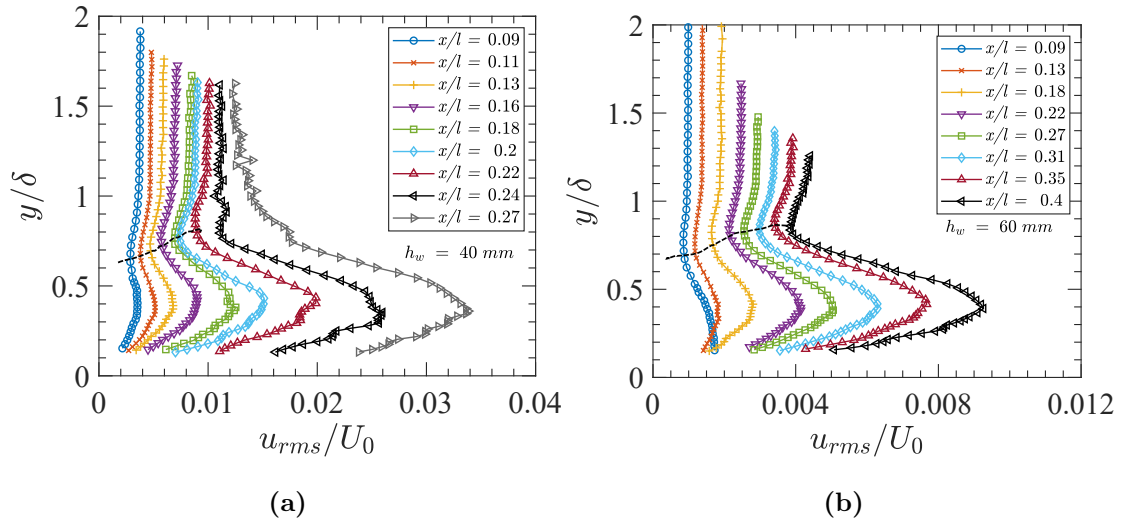


Figure 4.11: U_{rms} profiles for the case (a) $h_w = 40$ mm and (b) $h_w = 60$ mm, outer minima are connected with a dashed line.

Considering first the outer minimum, a similar trend in streamwise velocity fluctuations was observed in cylinder-wake induced transition reported by He et al. (2013). They ascribed the occurrence of the outer minimum to the shear sheltering phenomenon. Shear sheltering was first defined by Jacobs and Durbin (1998), especially for bypass transition, in which the boundary layer acts as a filter to block the outer high frequency disturbance while allowing the low frequency disturbance to penetrate inside the boundary layer. This sheltering effect is also confirmed by the spectral characteristics of the fluctuating signals in the present cases (to be discussed in next section). Another characteristic associated with this outer minimum can also be seen in figure 4.11a, whereby the minimum clearly persists till the point of transition onset ($x/l = 0.22$), but tends to disappear further downstream. For the case of $h_w = 60$ mm (figure 4.11b), the flow remains laminar throughout the domain and consequently, the minimum occurs at all the locations. Such an observation indicates a link between the presence of the outer minimum and the development of laminar breakdown.

Now, coming to the inner maximum ($u_{rms,max}$) in figure 4.11, its wall-normal position remains constant at around $y = 0.4\delta$ or $1.3\delta^*$ for both the cases in the pre-transitional zone. Downstream of the pre-transitional zone, $u_{rms,max}$ increases rapidly. To some extent, this can be seen for the case $h_w = 40$ mm in figure 4.11a, $x/l > 0.22$. Furthermore, for $x/l > 0.27$ the peak location of u_{rms} tends to move towards the wall, which is demonstrated in figure 4.12. The rapid growth of the u_{rms} and its inner peak moving towards the wall indicates the flow transitioning from laminar to turbulent.

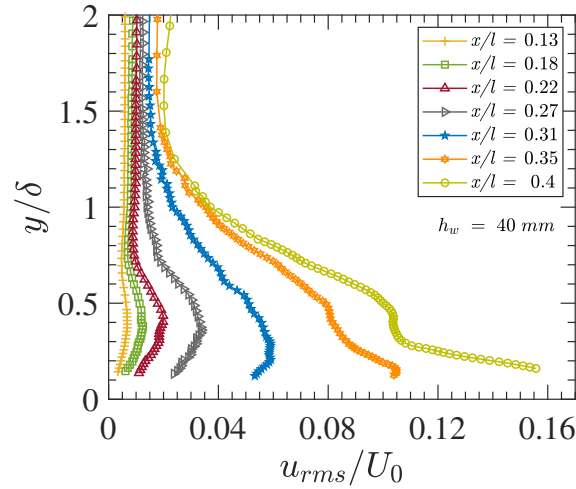


Figure 4.12: u_{rms} profiles for the case $h_w = 40$ mm, to demonstrate the rapid growth of u_{rms} in the transitional region.

It is found that the u_{rms} profile displays self-similarity when it is plotted as $u_{rms}/u_{rms,max}$ vs y/δ^* as shown in figure 4.13. It is also noted that the disturbance growth follows the transient growth theory developed by [Andersson et al. \(1999\)](#) and [Luchini \(2000\)](#). This theory was developed to understand the energy growth in FST induced bypass transition. According to this theory, the maximum disturbance growth ($u_{rms,max}$) is proportional to $x^{0.5}$. This type of disturbance growth is also referred to as algebraic growth or non-modal type (in contrast to the exponential growth of modal (T-S) disturbance). In addition, it can be seen in figure 4.13 that u_{rms} reaches its maximum at the wall-normal location $y = 1.3\delta^*$ and this value is widely accepted and confirmed in both experiments and numerical simulations of FST induced bypass transition ([Westin et al., 1994](#); [Matsubara and Alfredsson, 2001](#); [Jacobs and Durbin, 2001](#); [Brandt et al., 2004](#); [Fransson et al., 2005](#)). Cylinder wake-boundary layer interaction studies also showed similar non-modal growth, the later stage of pre-transitional characteristics being similar to bypass transition ([Mandal and Dey, 2011](#); [Ovchinnikov et al., 2008](#)).

Though the present measurements show non-modal behaviour in terms of u_{rms} , some unexpected characteristics can be seen when compared with FST and cylinder-wake induced bypass transition. For instance, figure 4.11a shows that laminar breakdown occurs at $x/l = 0.22$ in the $h_w = 40$ mm case and the maximum u_{rms} at this station is approximately 2% of U_0 . In contrast, u_{rms} values have been reported to be significantly higher (in the range of 5 - 20%) before the laminar breakdown for FST-induced transition ([Westin et al., 1994](#)) and cylinder-wake induced transitions ([Mandal and Dey, 2011](#)).

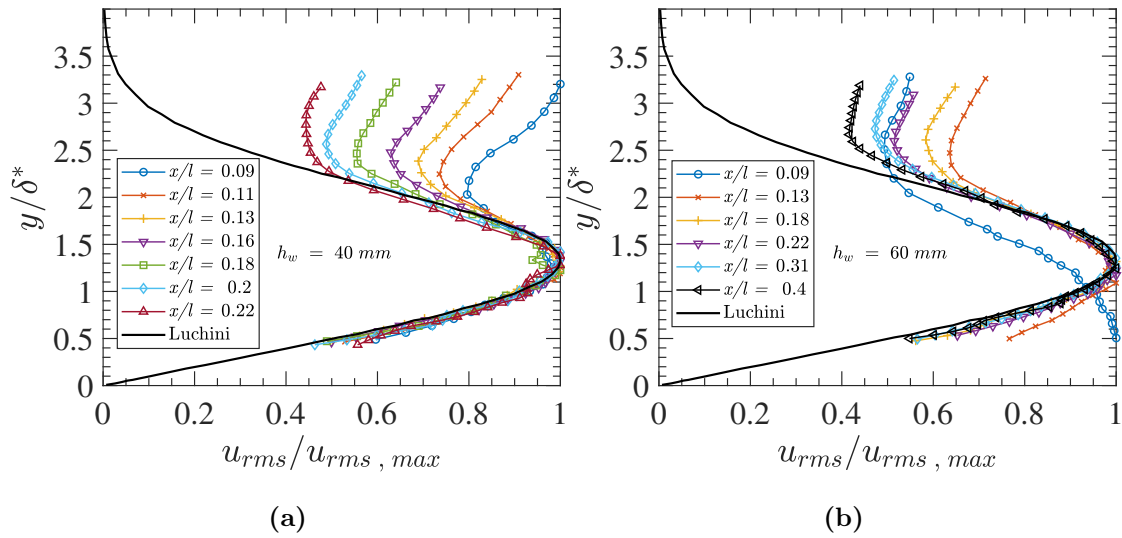


Figure 4.13: Normalised u_{rms} profiles for (a) $h_w = 40$ and (b) $h_w = 60$ mm compared with the u_{rms} obtained from the transient growth theory, Luchini (2000).

Another interesting observation can be made by comparing the u_{rms} distributions, specifically at $x/l = 0.09$ for $h_w = 40$ and 60 mm in figure 4.13. For the case $h_w = 60$ mm, u_{rms} does not follow the non-modal disturbance profile whereas it does for $h_w = 40$ mm. Further, the location of $u_{rms,max}$ for $x/l = 0.09$ tends to occur in the near-wall. It is to be noted that, in a low turbulence environment, for a T-S wave type modal disturbance, $u_{rms,max}$ occurs close to the wall. In the present experiment, if the wake is located farther from the wall (i.e., larger gap), then the initial upstream interactions (wake-boundary layer) occur at lower turbulent intensity. Hence, it could be expected that at such initial regions, the u_{rms} distribution behaves like that from a modal disturbance.

To further verify this reasoning, u_{rms} distribution is plotted for the gap $h_w = 80$ mm in figure 4.14, where one could expect that the initial interactions would occur at even lower turbulence intensity levels. From this figure, for $x/l = 0.13$ and 0.18, it is clear that $u_{rms,max}$ location appears to occur in the near-wall region. Further, for $x/l = 0.22$, $u_{rms,max}$ is located slightly below the $u_{rms,max}$ of the non-modal disturbance profile. For $x/l = 0.31$ and 0.4, the u_{rms} distribution follows the non-modal disturbance profile. From this observation, it can be inferred that the u_{rms} distribution is gradually transforming from a modal type of disturbance profile to a non-modal disturbance profile.

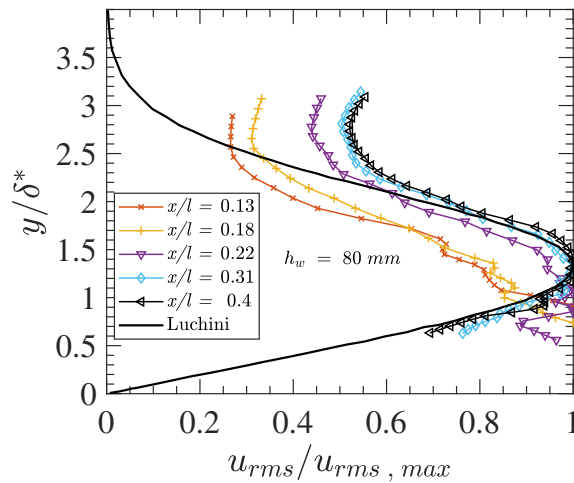


Figure 4.14: Transformation of u_{rms} profile from T-S type modal behaviour to non-modal behaviour for the case $h_w = 80$ mm.

To examine the effect of turbulent intensity on the transformation of disturbance profile from modal to non-modal behaviour, turbulent intensity of the forcing disturbance is plotted in figure 4.15 for the three different gaps reported above. It is emphasised here, that in the present experiment, the turbulent intensity of the forcing disturbance values correspond to the local values obtained at the edge of the boundary layer over a flat plate.

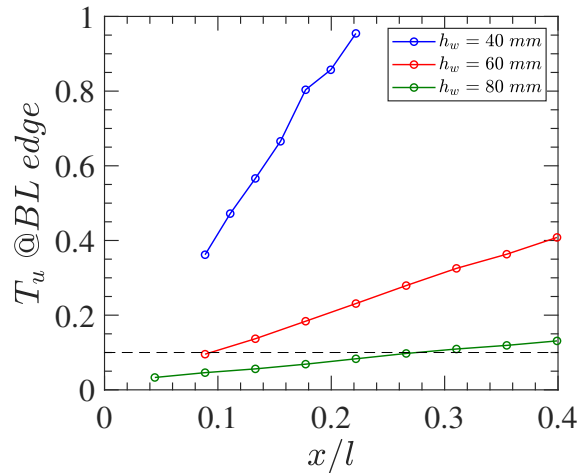


Figure 4.15: Distribution of turbulent intensity (%) at the edge of the boundary layer.

From figure 4.15, it can be noted that the turbulent intensity increases with streamwise distance and the rate of increase is higher if the gap is smaller. By comparing the disturbance profiles (figure 4.13 & 4.14) and the turbulent intensities (figure 4.15), it can be inferred that, for the turbulent intensity levels above

0.1%, the disturbance profile possesses non-modal characteristics, whereas for the lower intensity levels ($< 0.1\%$), the disturbance profiles turn modal. [Kosorygin and Polyakov \(1990\)](#) have mentioned that, in the case of FST-induced transition, the disturbance growth will be of modal type (T-S wave) at lower level of free-stream turbulence ($< 0.1\%$). The present observation of the transformation from modal to non-modal disturbance profile or in other words, the evolution of a non-modal disturbance profile is not reported in any other experimental study in the literature. This part of the flow with borderline characteristics would be very useful for studying the receptivity mechanism in detail, since the present experimental setup allows for investigating the evolution of disturbance profiles in the flow.

From a different perspective, figure 4.15 reveals an interesting feature that the turbulent intensity at the edge of the boundary layer increases linearly, however the wake and boundary layer thickness increases as $x^{1/2}$ ([Pope, 2000](#)), which invites further investigation.

Having observed the non-modal disturbance profiles for gaps $h_w = 40$ mm and 60 mm, we now proceed to investigate aspects such as linear energy growth, low frequency and streaky structure, since these are associated with non-modal disturbance profile.

4.2.3 Disturbance energy growth

To understand the growth of $u_{rms,max}$ and the perturbation energy in the downstream direction, $u_{rms,max}/U_0$ and $u_{rms,max}^2/U_0^2$ is plotted for various streamwise stations as shown in figure 4.16a and 4.16b. [Luchini \(2000\)](#) showed for a non-modal disturbance growth, the streamwise disturbance velocity is proportional to $x^{0.5}$ or the energy growth ($u_{rms,max}^2$) is proportional to x . Such algebraic growth was experimentally verified by [Matsubara and Alfredsson \(2001\)](#) for the FST induced bypass transition and [Mandal and Dey \(2011\)](#) for cylinder-wake induced transition. Since the present measurements follow the trend of non-modal disturbance profile, it is interesting to check whether the disturbance growth is algebraic or not. In figure 4.16a, $u_{rms,max}/U_0$ obtained from figure 4.11 for both the cases, $h_w = 40$ and 60 mm are plotted against $1.72\sqrt{Re_x}$ ($= Re_{\delta^*}$), and in figure 4.16b, the corresponding maximum energy inside the boundary layer is plotted for various streamwise stations. For better clarity, the log-linear plots of the variations are also shown in figure 4.16c and 4.16d.

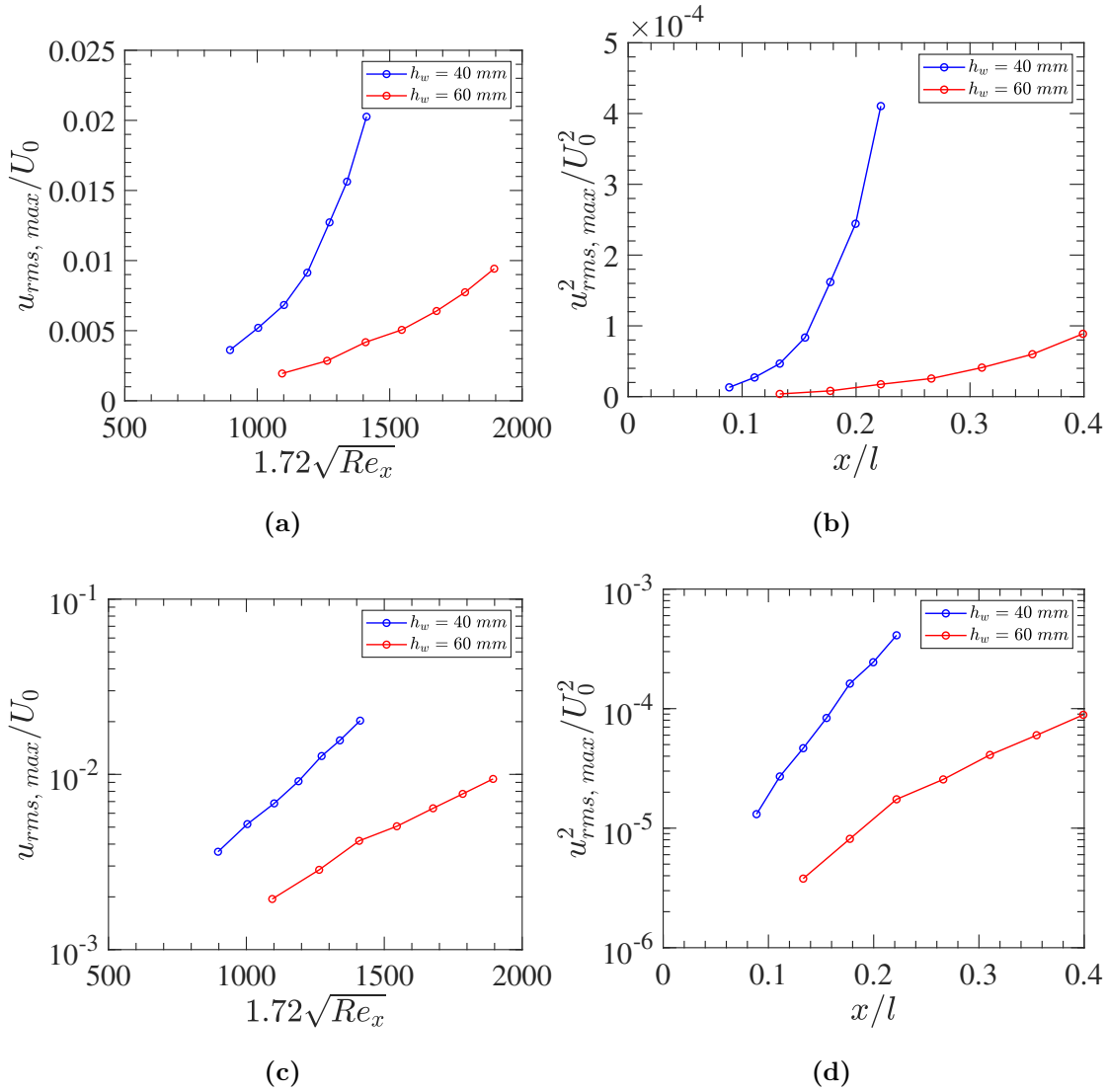


Figure 4.16: Streamwise growth of the $u_{rms, max}$ (a,c) and $u_{rms, max}^2$ (b,d).

In fact, figure 4.16a reveals that the disturbance growth is exponential rather than algebraic ($x^{0.5}$) as one would expect for a non-modal disturbance profile. The energy growth is also exponential as seen in figure 4.16b. Furthermore, from figure 4.16c and 4.16d, for the case $h_w = 60$ mm, it is noted that the disturbance and the energy growth occur in two phases.

To first explore the combination of exponential growth with a non-modal disturbance profile, the energy growth characteristics for FST induced bypass transition (Fransson et al., 2005) need to be looked at in great detail. It is noted in Fransson's study that there is an initial region of pre-algebraic growth where $u_{rms, max}^2$ increases exponentially at a slower rate, later increasing linearly following transient growth

theory. Fransson et al. attributed the initial non-linear (exponential) growth to the receptivity process, with the disturbance ‘adjusting’ to the boundary layer. However, the present results are in contrast to the previous observations, where for the whole pre-transitional region, $u_{rms,max}$ and its associated energy increase exponentially.

The possible mechanism behind the exponential energy growth can be reasoned as follows.

- In the case of FST induced bypass transition experiments, the disturbance is forced continuously from the leading edge, however its initial turbulence intensity is not varied for a given experiment. Rather here in the present experiments, the disturbance is forced through the edge of the boundary layer and its intensity level keeps increasing in the downstream direction, which is depicted in figure 4.15). This continuous variable forcing could lead to an energy growth in a non-algebraic route.
- There could be an element of modal growth (T-S wave) which is coexisting inside the boundary layer along with the non-modal u_{rms} distribution.

Having discussed the possibilities of exponential growth in figure 4.16, the energy growth appearing as a two-stage process for $h_w = 60$ mm is considered. As mentioned before, at $x/l = 0.09$, the interaction of the wake and boundary layer occurs at lower T_u (0.1%), which results in the u_{rms} distribution (figure 4.13) that appears like modal growth. On the other hand, for $x/l > 0.09$, the values of T_u at the edge of the boundary layer increase ($> 0.1\%$) and the non-modal disturbance growth is observed. Hence, the first stage of the disturbance growth could be responsible for the transformation from modal to non-modal behaviour and the reason for the second stage growth could be the same as discussed before.

In addition, it can be noticed from figure 4.16 that the energy growth rate of $h_w = 40$ mm is steeper when compared with that of $h_w = 60$ mm. This is especially due to the increase in turbulent intensity with decrease in gap of the aerofoil (figure 4.15). Fransson et al. (2005) and Norimatsu et al. (2011) have shown, for the case of FST induced bypass transition, if the FST levels are increased, energy growth rate in the pre-transitional zone increases.

Further, streamwise growth of the integral averaged boundary layer energy (figure 4.17) is calculated by using equation 4.5. Here, the integration is carried out up to the location of the minimum peak in the u_{rms} profile (sheltering edge) rather than the edge of the boundary layer. This is primarily done to consider the boundary layer disturbance alone by following He et al. (2013).

$$E_{u,se} = \int_0^{\delta_s} u_{rms}^2 dy / (U_0^2 \delta_s) \quad (4.5)$$

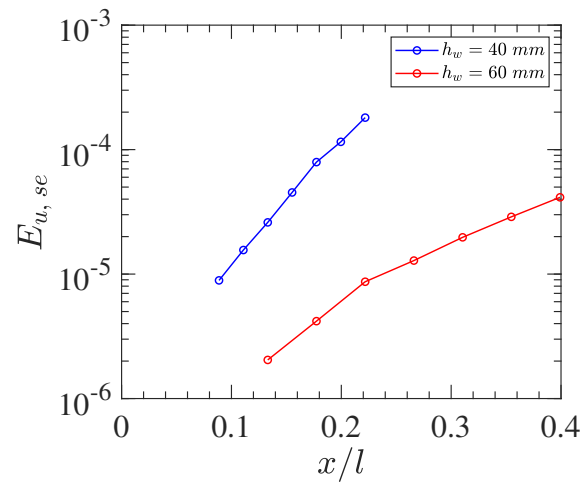


Figure 4.17: Integral energy growth of $h_w = 40$ and 60 mm.

Figure 4.17 reveals that the averaged boundary layer disturbance energy grows exponentially by following the same trend as in figure 4.16. It is noticed that in the case of cylinder-wake boundary layer interaction (He et al., 2013), energy growth also occurs exponentially, along with non-modal behaviour of u_{rms} . They reasoned that the formation and the destabilization of the secondary vortex (due to vortex shedding) in the near-wall region could be responsible for the exponential energy growth. Conversely, in the present scenario, there is no evidence of vortex shedding, hence the reason suggested by He et al. (2013) would not be appropriate to consider despite the similar disturbance growth.

4.2.4 Power spectral density

To understand the influence of dominant frequencies on the disturbance growth, the power spectral density is determined. Both the spectral power and the frequencies are normalised by following the equation 4.6 and 4.7 (Westin et al., 1994). The cases considered for this analysis are $h_w = 40$ and 60 mm at $x/l = 0.16$ and 0.31 respectively. The relevant mean velocity profile are plotted in figure 4.18 and the corresponding power spectral density are plotted in figure 4.19

$$P_n = p/0.5U_0^2\Delta F \quad (4.6)$$

$$F = 2\pi f\nu \times 10^6/U_0^2 \quad (4.7)$$

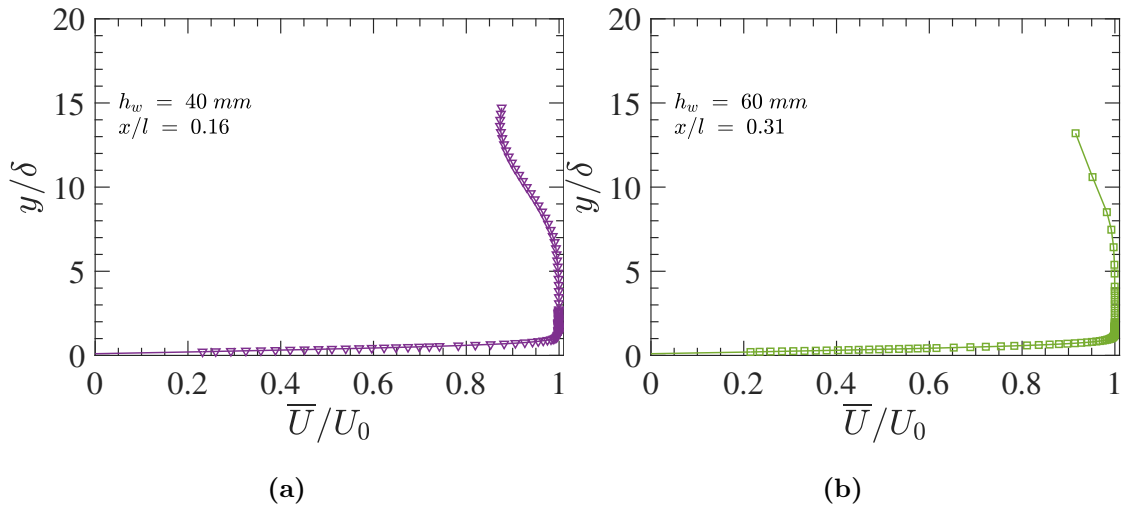


Figure 4.18: Normalised mean velocity profile of (a) $h_w = 40$ mm at $x/l = 0.16$ and (b) $h_w = 60$ mm at $x/l = 0.31$.

The power spectrum obtained at the wake core region in figure 4.19a ($y/\delta = 14.3$) and figure 4.19b ($y/\delta = 13.1$) clearly shows that the wake is fully turbulent (with no vortex shedding). In the potential core region ($y/\delta = 3.7$ and 4), a bandwidth of frequency ($F = 30$ - 110) appears to be pronounced, which could be attributed to the intermittent nature of the shear layer edge (as discussed in chapter 2). As the probe moves towards the edge of the boundary layer, high frequency perturbations associated with the small scales of the wake turbulence are attenuated. Nevertheless, the bandwidth of dominant frequency still remains. Further moving inside the boundary layer ($y/\delta = 0.8, 0.5$ and 0.2), it is clearly evident that the low frequency perturbations ($F = 1$ - 30) are amplified and the other frequencies are further diminished. In addition to that, at $y/\delta = 0.2$, a small portion of mid-range frequencies

(around $F = 50-70$) within the domain of dominant frequency from the wake gets amplified for both the cases.

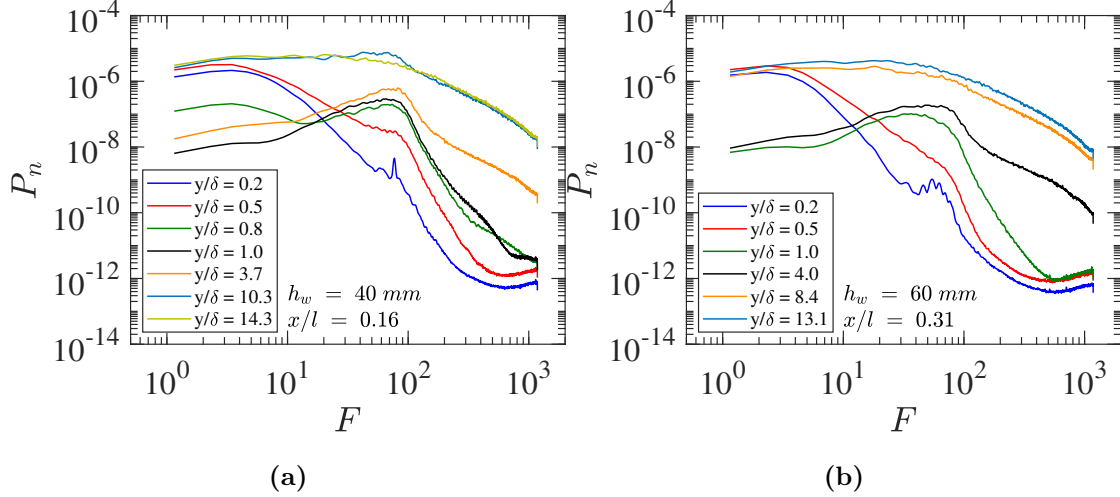


Figure 4.19: Normalised power spectral density for various wall-normal stations for (a) $h_w = 40$ mm and (b) $h_w = 60$ mm.

Amplification of low frequency fluctuations inside the boundary layer could be associated with shear sheltering phenomenon (Jacobs and Durbin, 1998, 2001). As discussed, shear sheltering will act as a filter for free-stream disturbances allowing only the low frequency to penetrate inside the boundary layer and, furthermore, to be amplified because of the mean shear. By observing figure 4.19, this phenomenon appears to occur in both cases. It is worth reiterating at this point that the local minimum in u_{rms} (figure 4.11) corresponds to the region where shear sheltering occurs, which can be confirmed from figure 4.19. It is seen that the low frequency amplification starts to occur below the edge of the boundary layer and the minimum in figure 4.11 is also located just below the boundary layer edge. This correlation confirms the link between shear sheltering and the local minimum of u_{rms} . The amplification of mid-range frequencies at $y/\delta = 0.2$ may be an indication of T-S waves or modal disturbances. This is supported by the streamwise development of the spectral distribution, shown in figure 4.20.

Figure 4.20 shows the spectral distribution for various streamwise stations obtained at $y/\delta = 0.2$. For both the cases $h_w = 40$ and 60 mm, it could be noticed that two particular frequencies, around $F = 50-70$ (mid-range frequency) and $F = 200-300$ (high frequency) are prominent at all streamwise stations (except $x/l = 0.2$ and 0.22 for $h_w = 40$ mm). In addition, for the case $h_w = 60$ mm (figure 4.20b), it can be noted that the power spectral density in the mid-range frequency band

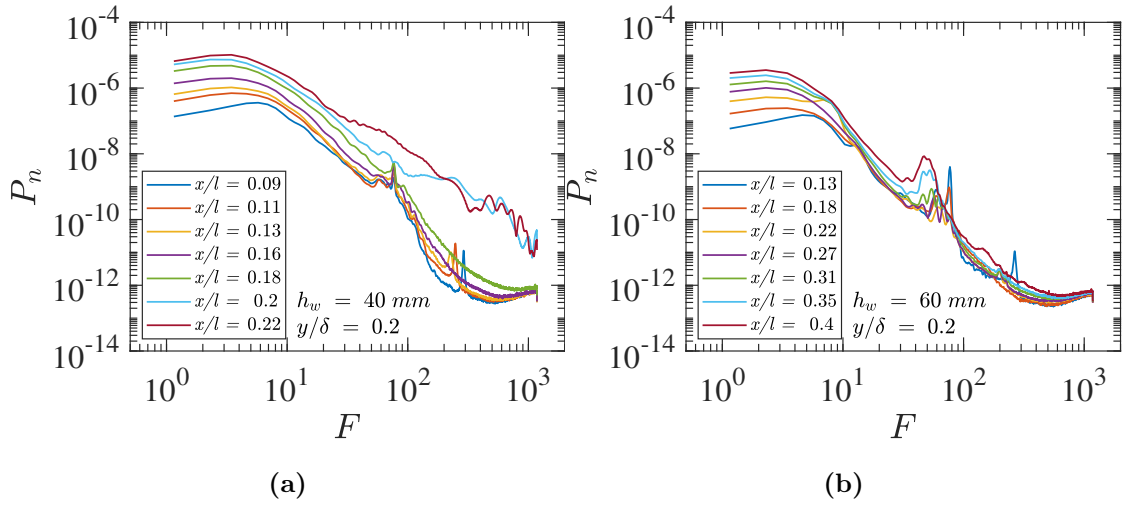


Figure 4.20: Normalised power spectral density for various streamwise stations, measured at $y/\delta = 0.2$ for the case (a) $h_w = 40$ and (b) $h_w = 60$ mm.

increases in the downstream direction. This kind of amplification, accompanied by a reduction in the dominant frequency, is typical of the evolution of T-S waves. This can be further explored by extracting the u_{rms} distribution at selected frequencies.

Figure 4.21 shows the u_{rms} profiles for selected frequencies at two streamwise stations for the case $h_w = 40$ mm. At low frequencies ($F < 29$), the u_{rms} profile possesses the characteristics of a non-modal disturbance for both streamwise stations. Conversely, for $F = 78$ and 249 (corresponding to the peaks in the power spectral density, figure 4.20a), a near-wall amplification of the u_{rms} is observed. The near-wall amplification for $F = 249$ is too noisy to consider for any interpretation. On the other hand, the near-wall peak for $F = 78$ can be considered as a characteristic of a modal disturbance as this particular frequency value matches with the frequency of the T-S wave. By comparing the two streamwise stations in figure 4.21a and 4.21b, at $F = 78$, it can be seen that u_{rms} is amplified as one moves downstream.

The equivalent results for the case $h_w = 60$ mm are presented in figure 4.22. In this case, the near-wall peak of the u_{rms} and its spatial amplification is clearly visible for $F = 53$. Such an amplification at the near-wall region for both $h_w = 40$ and 60 mm can be seen as the characteristic of modal growth. Again, the amplifications near the wall at $F = 150$ is noisy for any interpretation to make.

In order to check that these frequencies are consistent with modal growth, a linear stability analysis was conducted and is discussed in the next chapter. The

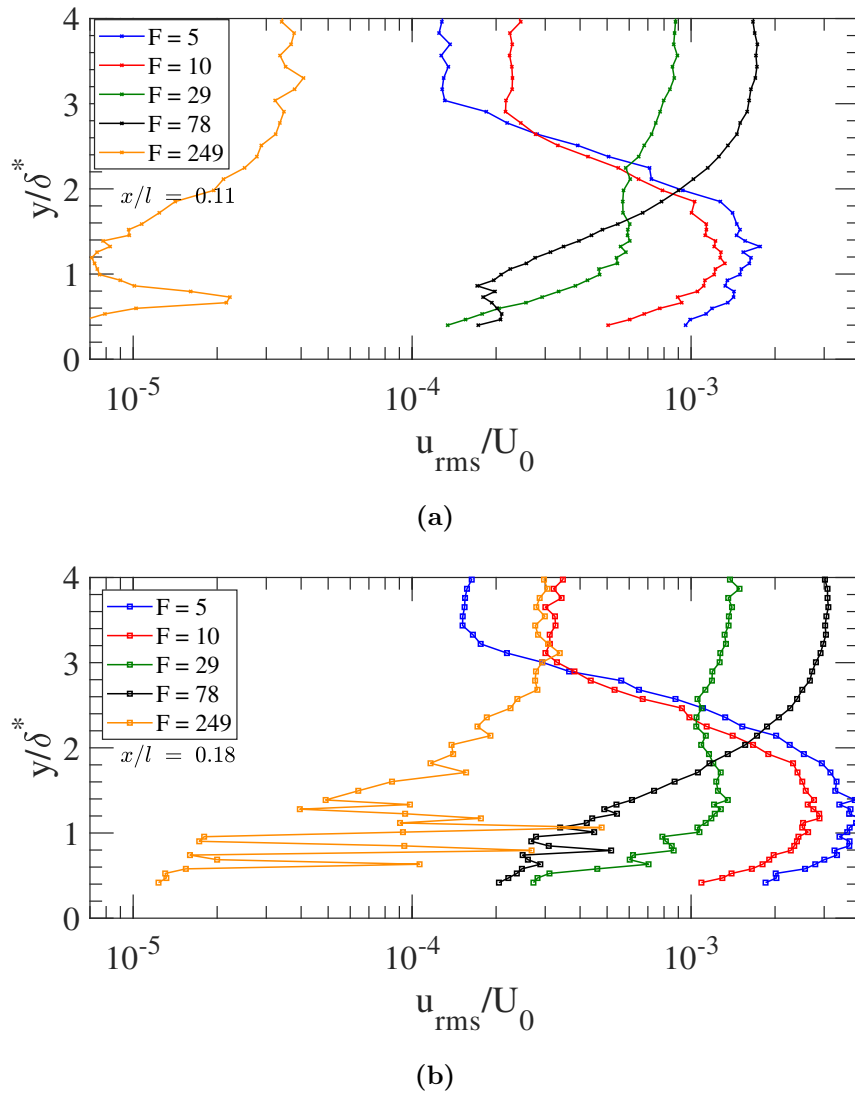


Figure 4.21: u_{rms} distribution obtained for the selected frequency band at $h_w = 40$ mm (a) $x/l = 0.11$, (b) $x/l = 0.18$.

frequencies (both mid-range & high) corresponding to spikes in the spectra (figure 4.20) were compared with the neutral curve of the Blasius flow. It was found that only the mid-range frequencies lie in the unstable regime ($F = 78$ and 53 for $h_w = 40$ and 60 mm respectively). Although there is scope for further measurements to resolve better these structures, the results are consistent with the coexistence of both modal and non-modal characteristics in the pre-transitional zone of the aerofoil-wake induced transition. In the case of moderate level of FST (0.3-0.7%) induced transition, Kosorygin and Polyakov (1990); Kenchi et al. (2008); Matsubara et al. (2010) have noticed T-S wave in the presence of non-modal u_{rms} distribution, however, other characteristics such as energy growth and streaky structures are different when compared with the present results. For instance, they reported an algebraic

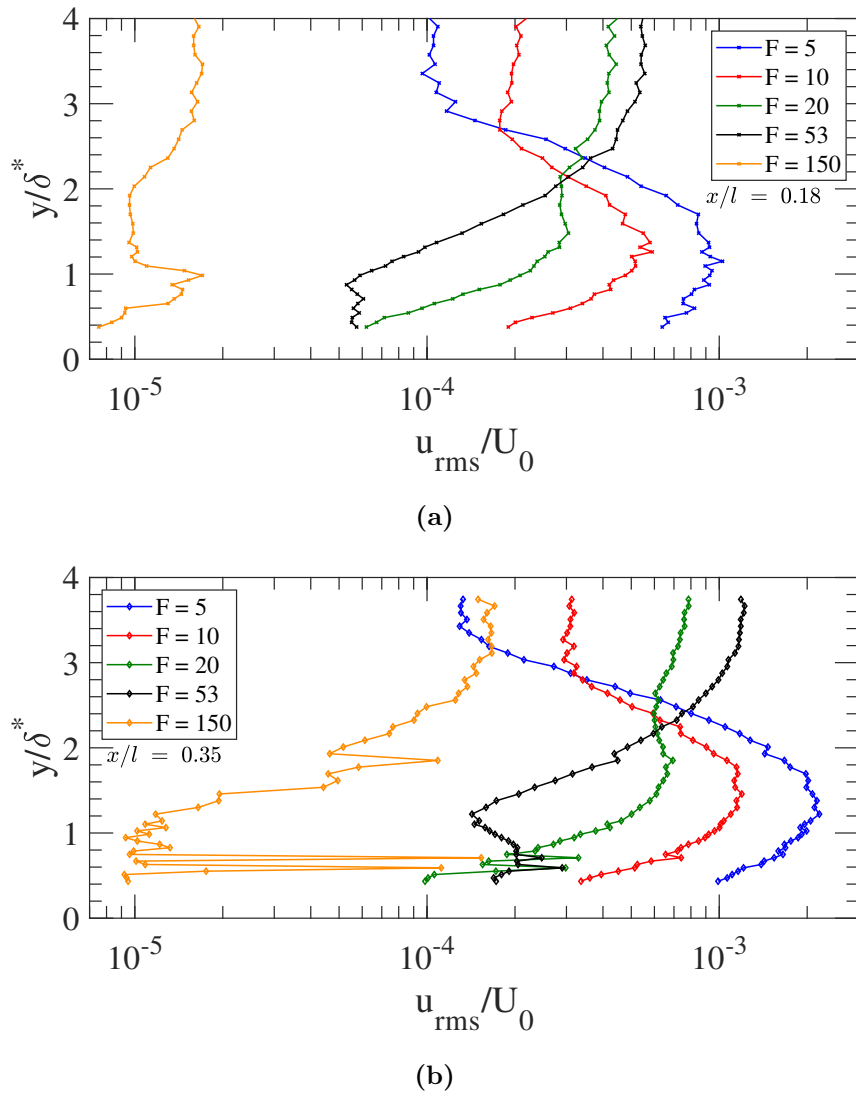


Figure 4.22: u_{rms} distribution obtained for the selected frequency band at $h_w = 60$ mm (a) $x/l = 0.18$, (b) $x/l = 0.35$.

energy growth in the pre-transitional region, conversely, in the present study, the energy growth is exponential.

Returning to the spectra shown in figure 4.20a, high frequency oscillations can be seen at $x/l = 0.2$ and 0.22 for $h_w = 40$ mm. According to Blair (1992), such high frequency fluctuations are due to turbulent spots. In the present case ($h_w = 40$ mm), it is known that transition onset occurs at $x/l = 0.22$, accordingly the high frequency perturbations are likely to be associated with turbulent spots. Also at $x/l = 0.2$, some occasional spots are noticed in the fluctuating velocity signals which is reflected as high frequency fluctuations in the spectrum. In the case of $h_w = 60$ mm (figure 4.20b), as already mentioned, transition onset was not noticed, which would

explain why no high frequency oscillations are seen in the spectra.

4.2.5 Correlation measurement

As the present experimental results displayed some of the characteristics of bypass transition, an attempt was made to check whether streaky structures could be detected inside the boundary layer. The presence of streaky structures in the pre-transitional zone can be identified by measuring spanwise correlations or by flow visualisation. Here, spanwise correlations of streamwise velocity fluctuations are obtained using the correlation function in equation 4.8.

$$R = \frac{\overline{u(t, z)u(t, z + \Delta z)}}{u(z)_{rms}u(z + \delta z)_{rms}} \quad (4.8)$$

For the present experiment, figure 4.23 shows the correlation function obtained for both the gap cases considered. The correlation measurements were carried out at a wall-normal location that approximately corresponds to $u_{rms,max}$. It is known that any presence of streaky structure would result in a negative correlation and vice versa. The results presented in figure 4.23 therefore offer a clear indication of the existence of streaks in the present experiment.

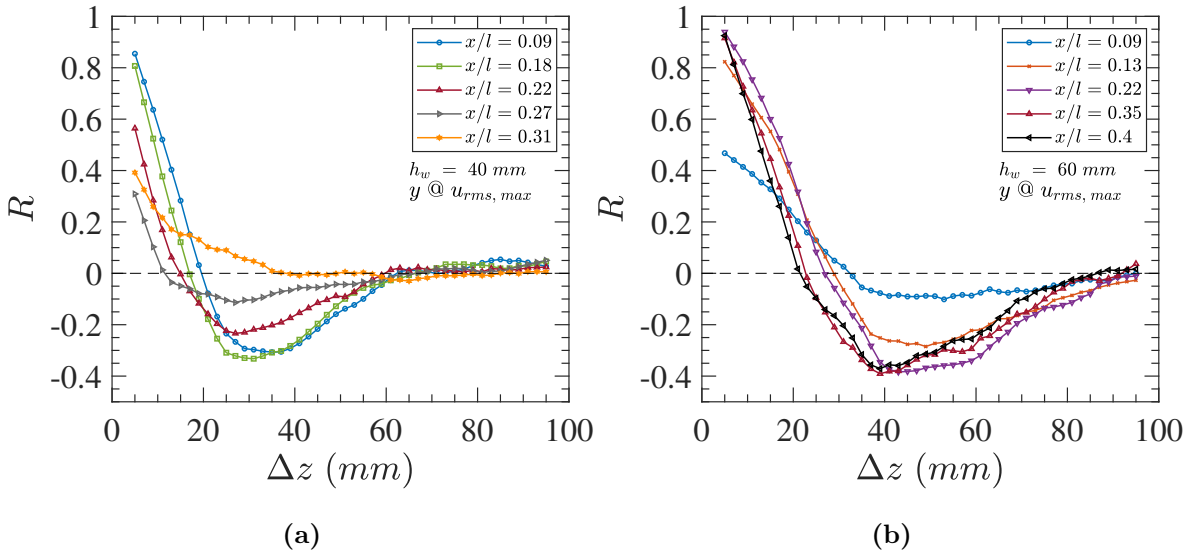


Figure 4.23: Spanwise correlation function (R) measured close to $u_{rms,max}$ for (a) $h_w = 40$ mm and (b) $h_w = 60$ mm.

For the case $h_w = 40$ mm (figure 4.23a), the measurements were carried out on both pre-transitional and transitional zones. Up to the location of transition onset,

$x/l < 0.22$, i.e., for $x/l = 0.09$ and 0.18 the correlation function is negative showing the presence of streaky structures. Further downstream in the transitional region, $x/l > 0.22$, it is evident that the value of the correlation function increases from a negative value and move towards a positive value. This indicates the breakdown of streaks into turbulent spots.

In the case of $h_w = 60$ mm (figure 4.23b), it is to be noted that all the streamwise stations lie in the pre-transitional zone. The correlation function in the free-stream is plotted along with that of the other x/l stations for base reference. By observing the figure, two features can be highlighted: a) at $x/l = 0.09$ and 0.13 , the value of the negative maximum of R is less when compared to that of the downstream stations and b) the location and the value of negative maximum of R appear to remain constant for $x/l > 0.13$. These trends are consistent with the u_{rms} profiles shown in figure 4.13b, where the disturbance profiles at $x/l = 0.09$ and 0.13 differ from the rest, and support the hypothesis that the flow is adapting from a T-S type modal behaviour to a non-modal behaviour. Further, energy growth for the case $h_w = 60$ mm in figure 4.16d also occurs at two different phases. From these supporting observations, it can be conjectured that, correlations obtained at $x/l = 0.09$ and 0.13 indicate the process of formation of streaky structures. If the gap (h_w) is increased further, one might expect to observe a more obvious transformation from modal to non-modal behaviour and more detail of the formation of streaky structures in the pre-transitional zone. Such information would help the understanding of the receptivity mechanism and the genesis of streaky structure, perhaps more so than the FST-induced transition case.

The relation between average streak spacing and the correlation function was initially arrived by Kendall (1985). It was reported that the distance between the origin and the location of most negative correlation is equal to half the wavelength of the streak spacing (here, wavelength is defined as the distance between two consecutive positive streaks). With this definition, for the present experiments, the average streak spacing in the pre-transitional zone can be obtained. From the figure 4.23, the streak spacing for $h_w = 40$ and 60 mm are obtained as 60 mm (30×2) and 80 mm (40×2) approximately and this value remains constant in the pre-transitional zone, meaning the spanwise scale of the structure does not vary in the downstream.

Further, the spanwise scale of the above streaks are observed to be very large when compared to the corresponding boundary layer thickness. For clarity, the above correlation plots are re-plotted in figure 4.24 with the x-axis normalised using

boundary layer thickness. From figure 4.24, it can be seen that the streak size is at least 10 times larger than the boundary layer thickness. In FST case, the spanwise scale of the streaks are initially larger near the leading edge and gradually it coincides with the value of the boundary layer thickness in the downstream (Matsubara and Alfredsson, 2001). However, in the present scenario, the streak size is much larger and does not approach the boundary layer thickness before the laminar breakdown (figure 4.24a). Also, it is established in literature studies that the presence of streaky structure would be reflected in the mean velocity profile in terms of a small deviation from the Blasius solution. In the present results, as previously noted, no deviation was observed in the mean velocity profiles (figure 4.7a) and the corresponding disturbance levels (figure 4.11a) are much less ($\sim 2\%$ of U_0 at transition onset) when compared to the FST induced bypass transition case ($\sim 10\%$ of U_0 at transition onset). Hence, it can be argued that the streaky structures observed in the present experiments are weaker despite their larger spanwise scale.

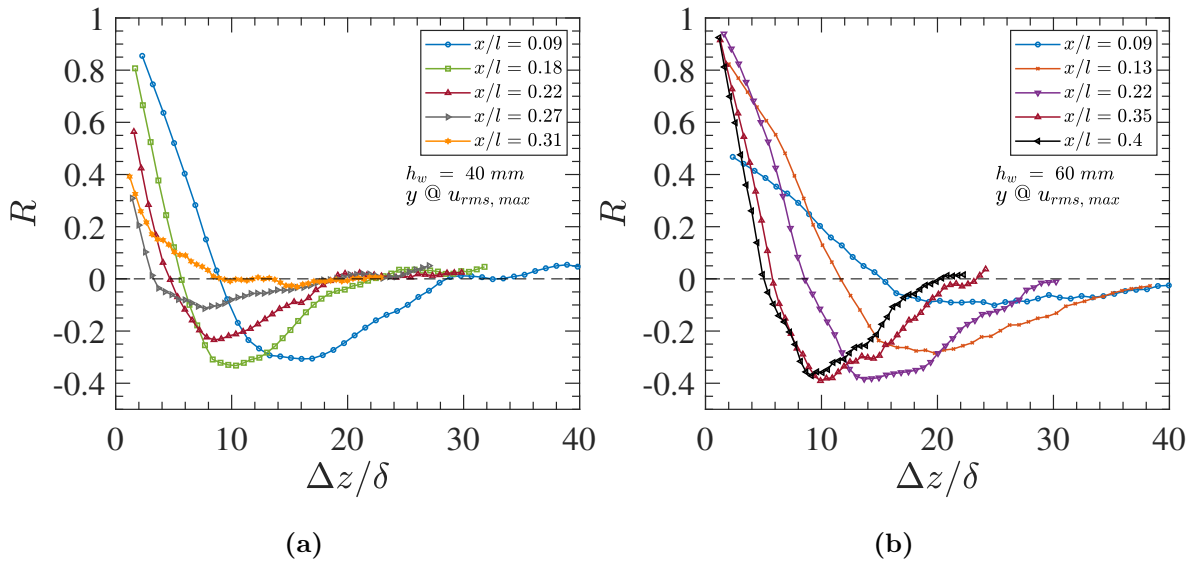


Figure 4.24: Spanwise correlation function (R) measured close to $u_{rms,max}$ for (a) $h_w = 40$ mm and (b) $h_w = 60$ mm, spanwise distance is normalised with local boundary layer thickness.

The height of the streaky structures inside the boundary layer can be obtained by measuring the correlation function in the $y - z$ plane. This is achieved through two point correlation measurements carried out at various wall-normal stations inside the boundary layer. From the measurements, a contour plot of the correlation function in the $y - z$ plane is obtained as shown in figure 4.25. The spanwise step size used in the contour plot is 2 mm and the wall-normal step size is 0.1 mm. The plot shown in the figure is for the case $h_w = 40$ mm at $x/l = 0.18$ and the local boundary

layer thickness at this station is 2.99 mm. The dashed and solid lines in the plot correspond to negative and positive correlations respectively. By observing the plot, it can be found that the streak extends up to 65% of the boundary layer thickness, whereas in the case of FST induced transition, the height of the structure is almost equal to the boundary layer thickness as reported by Matsubara and Alfredsson (2001).

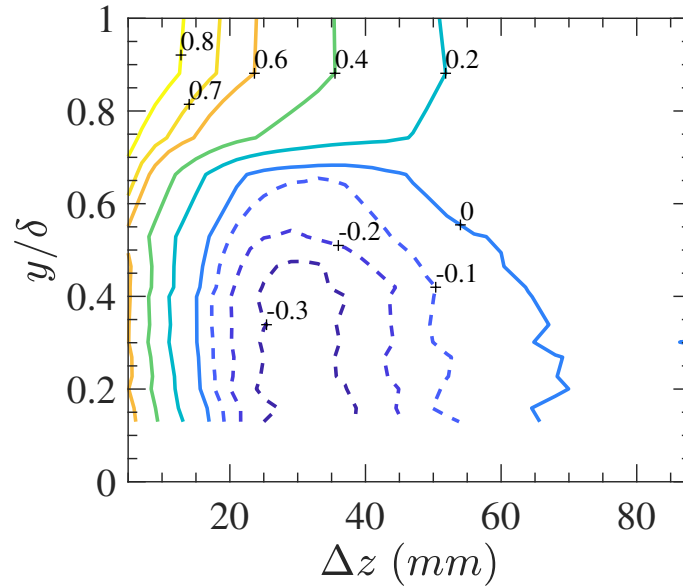


Figure 4.25: Wall-normal contour of spanwise correlation, dashed line represents the negative correlation and the values are correspond to the correlation function, $h_w = 40$ mm, $x/l = 0.18$.

To summarise, the spanwise and wall-normal scales of the longitudinal streaks were found to be different to those reported by other transition studies in literature. The factors determining the streak spacing are not well established. In the next two subsections, the influence of the gap and the Reynolds number on the streak spacing is analysed using the correlation measurements.

4.2.6 Effect of gap on the streak spacing

Correlation functions are obtained for three different gaps, $h_w = 20, 40$ and 60 mm for a fixed Reynolds number ($Re_c = 3.4 \times 10^5$). The resulting correlation plots are shown in figure 4.26. The streamwise stations for all three gaps are chosen in the pre-transitional zone. For gap $h_w = 40$ and 60 mm, correlation is measured at the $x/l = 0.18$, however for $h_w = 20$ mm, transition onsets early, so the correlation is measured in an upstream location at $x/l = 0.04$. Because, as observed previously in figure 4.24, streak spacing does not vary with x/l in the pre-transitional zone, it is reasonable

to deduce the effect of the gap (from figure 4.26) despite the measurements being taken at different streamwise locations. To ascertain the effect of gap on the streak spacing, power spectral density is obtained at the edge of the boundary layer for the corresponding streamwise stations in correlation measurement, which is shown in figure 4.27.

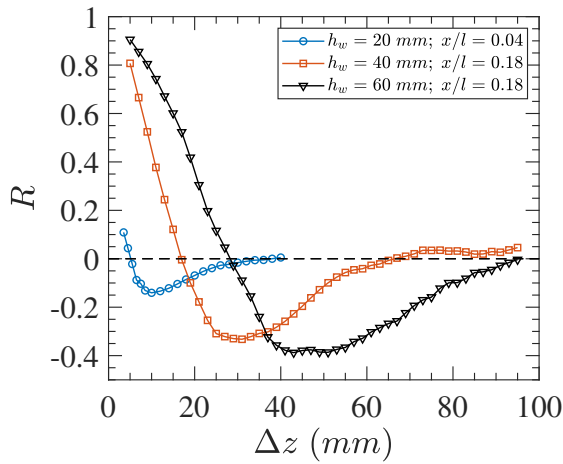


Figure 4.26: Spanwise correlation measurement for various gap, $Re_c = 3.4 \times 10^5$.

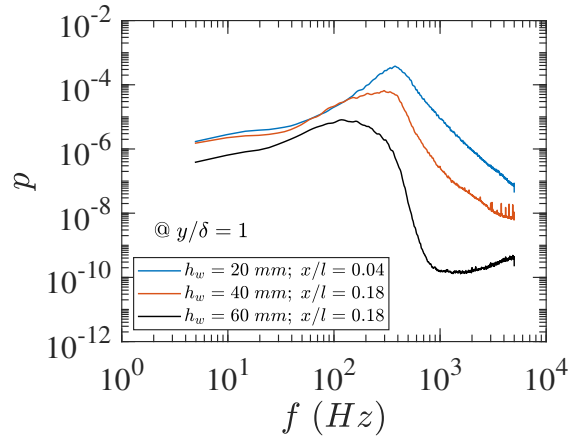


Figure 4.27: Power spectral density, obtained at the edge of the boundary layer for the corresponding stations in figure 4.26.

From figure 4.26, it can be found that the average spanwise spacing of the streak increases with increase in gap. The exact reasoning for such an effect is not explicitly known, however, varying the gap alters two specific aspects in the current experiments. Firstly, with increase in the gap, the interaction between the wake and the boundary layer occurs at a reduced turbulence level (figure 4.15). Secondly, by looking at the spectral plot (obtained at the edge of the boundary layer) in figure 4.27, it can be seen that the bandwidth of disturbance frequency increases when the gap is increased.

As already mentioned, the absolute value of the streak spacing seems to be independent of streamwise location in the pre-transitional zone. It is also observed that the frequency at which the disturbance acts on the boundary layer is also independent of streamwise location in the pre-transitional zone, as shown in figure 4.28. On the other hand, when the gap is varied, both the streak spacing and the bandwidth of frequency are altered, suggesting a link between the two. Further investigations will be required to understand the streak spacing characteristics in detail.

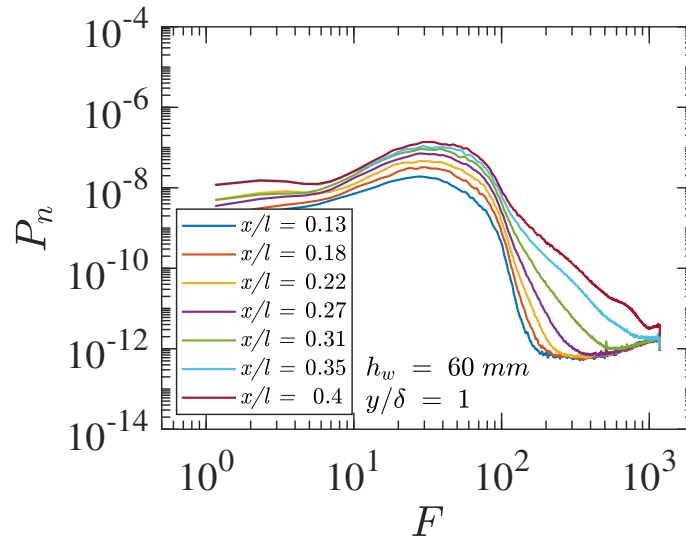


Figure 4.28: Power spectral density measured at the edge of the boundary for various streamwise stations, $h_w = 60$ mm.

4.2.7 Effect of Reynolds number on the streak spacing

To study the effect of Reynolds number on the streak spacing, three different free-stream velocities, $U_0 = 5, 10$ and 20 m/s are considered in the experiments, resulting in three values of Reynolds number, given by $Re_c = 0.8 \times 10^5, 1.7 \times 10^5$ and 3.4×10^5 . The spanwise correlation measurements obtained for three different Re_c , for two gaps are shown in Figure 4.29. The two streamwise stations chosen for the measurements are given by $x/l = 0.18$ and 0.22 for the gaps $h_w = 40$ and 60 mm respectively. The wall-normal position considered for this measurement corresponds to a location of $u_{rms,max}$.

Upon observing the correlation plots for both the gaps, figure 4.29a and 4.29b, the effect of Re_c on the streak spacing appears to be independent for $Re_c = 1.7 \times 10^5$ and 3.4×10^5 , since the minimum negative correlation occurs at the same spanwise location. On the other hand, for $Re_c = 0.8 \times 10^5$, the minimum negative correlation occurs early, thus the streak spacing is observed to be slightly reduced from the other two Re_c values.

Earlier in this section on the effect of gap, a link was observed to exist between the spanwise scale and the bandwidth of disturbance frequency interacting the boundary layer. Here, a similar attempt is made to check if any such link exists. For this, the power spectral density obtained at the edge of the boundary layer is given in figure 4.30a and 4.30b. The values of Re_c, h_w and x/l correspond to the figure 4.29a and 4.29b respectively.

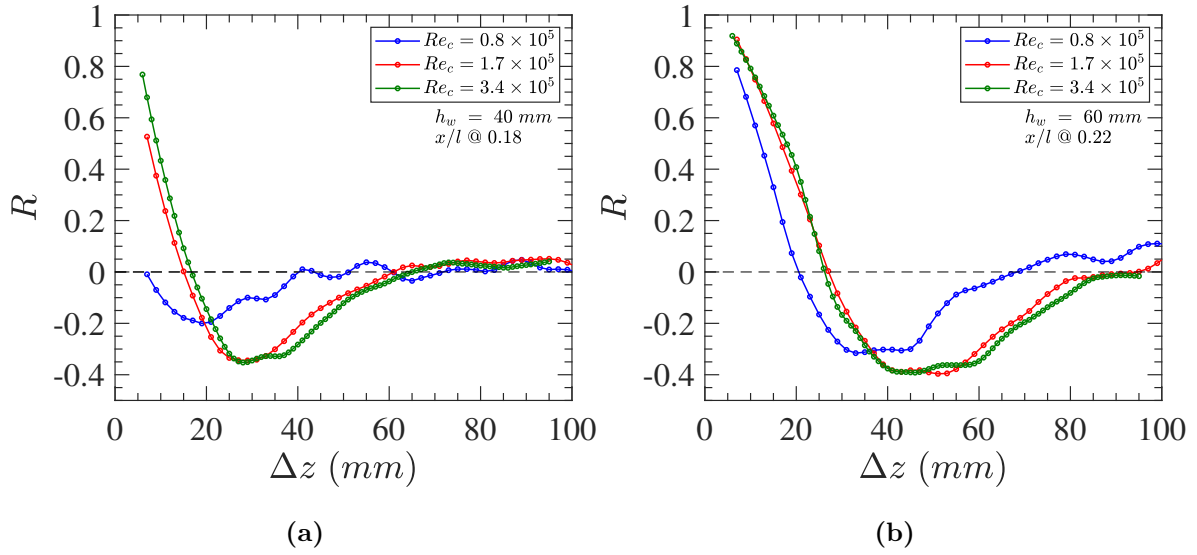


Figure 4.29: Spanwise correlation measurement for three different Reynolds number for the case (a) $h_w = 40$ mm, measured at $x/l = 0.18$ and $y/\delta^* = 1.3$ and (b) $h_w = 60$ mm, measured at $x/l = 0.22$ and $y/\delta^* = 1.3$.

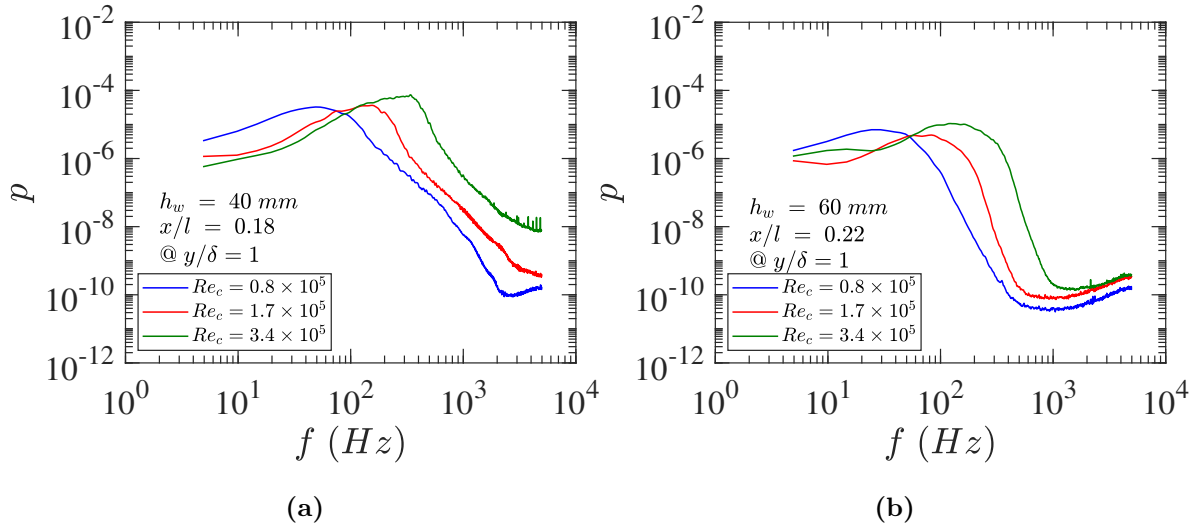


Figure 4.30: Streamwise power spectral density obtained at the edge of the boundary layer for corresponding correlation plot in figure 4.29.

From figure 4.30, for a given gap, it could be noticed that the spectral distribution follows the same trend for $Re_c = 1.7 \times 10^5$ and 3.4×10^5 . On the other hand, for $Re_c = 0.8 \times 10^5$, the energy content at the lower frequency is increased and the frequency of the dominant disturbance also shifts to the lower side. This observation is consistent with the correlation plot, (Figure 4.29) where the spanwise spacing does not change for $Re_c = 1.7 \times 10^5$ and 3.4×10^5 but it does for $Re_c = 0.8 \times 10^5$. Thus, the

change in the spectral characteristics at the low Reynolds number $Re_c = 0.8 \times 10^5$ would have led to different streak spacing.

To check the effect of Re_c on streamwise fluctuation profile, the u_{rms} distribution and its corresponding streamwise energy growth are plotted for three different Re_c for the gap $h_w = 40$ mm in Figure 4.31 and 4.32. From the u_{rms} profile and the energy growth characteristics, it can be observed that the Reynolds number does not influence the disturbance profile and its energy growth characteristics. Thus, it can be argued that the distinct behaviour of the spanwise streak spacing at the low Re_c (0.8×10^5) in Figure 4.29 can be due to the change in the wake characteristics at such low Reynolds number. This in turn would need a rigorous study to reveal the effect of Re_c comprehensively.

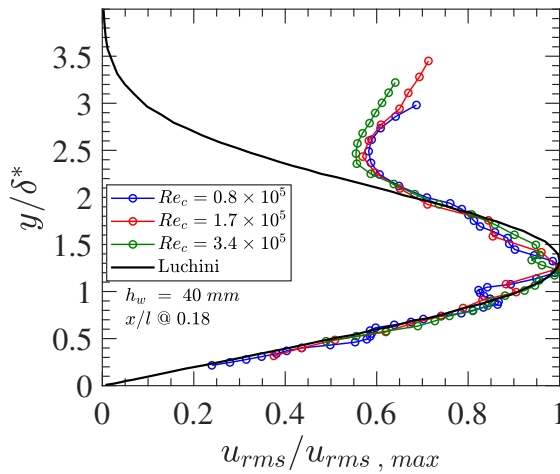


Figure 4.31: Normalised u_{rms} profile measured at $x/l = 0.18$ for the case $h_w = 40$ mm for three different Reynolds number.

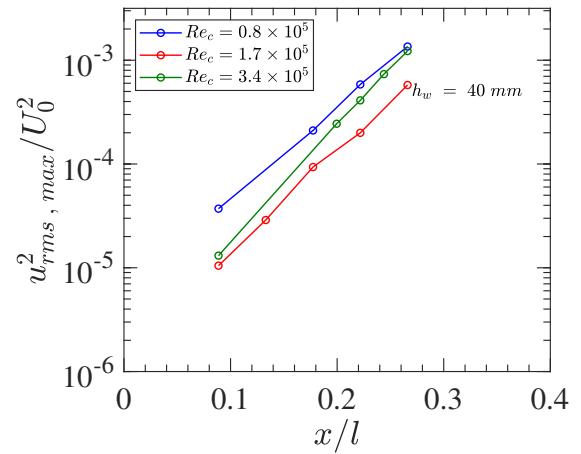


Figure 4.32: Maximum streamwise energy growth for the case $h_w = 40$ mm, for three different Reynolds number.

4.3 Discussion and Summary

In the present work, an attempt was made to understand the laminar-turbulent transitional characteristics of aerofoil wake-boundary layer interaction. Further emphasis was placed on elucidating the differences between the transition characteristics of the present configuration with that of the other transition mechanisms established in the literature (FST induced transition and cylinder wake-boundary layer interaction).

For the experiments, a new experimental setup involving a combination of an aerofoil and a flat plate configuration was used and the measurements were carried out on the flat plate especially in the pre-transitional zone. The pre-transitional zone is defined as the region from the leading edge up to the point where the first turbulent spots are spotted in the streamwise station.

This chapter has presented a systematic analysis of the measurements carried out for two gap heights, $h_w = 40$ and 60 mm, with a fixed overlap ($x_w = 0.25c$) and Reynolds number ($Re_c = 3.4 \times 10^5$). The key observations are summarised below.

1. The mean velocity profile is well matched with the Blasius profile, see figure 4.7.
2. For the most part, the u_{rms} distributions follow the non-modal disturbance profile obtained from the transient growth theory, figure 4.13. For the case $h_w = 60$ mm at the initial two streamwise stations ($x/l = 0.09$ and 0.13), the u_{rms} distribution deviates from the non-modal type in the sense that the u_{rms} peak occurs near the wall ($x/l = 0.09$), figure 4.13b. This initial deviation may indicate the transformation of disturbance profile from modal to non-modal which was confirmed from the results corresponding to $h_w = 80$ mm (figure 4.14).
3. The observed outer minimum in the u_{rms} profile in the pre-transitional zone is consistent with the occurrence of shear sheltering phenomenon.
4. The value of $u_{rms,max}$ at the laminar breakdown is found to be around $0.02U_0$, which is much less than that for FST-induced bypass transition, see figure 4.11a.
5. $u_{rms,max}$ and the corresponding measure of disturbance energy growth vary exponentially in the streamwise station in contrast to the algebraic growth usually observed for a non-modal disturbance profile, refer figure 4.16.

6. Turbulent intensity (T_u) at the edge of the boundary layer is found to increase linearly in the downstream distance, however the wake and boundary layer thicknesses, and therefore separation, vary with $x^{1/2}$, see figure 4.15.
7. Power spectral densities of the streamwise velocity fluctuations at various wall-normal locations show that the low frequency disturbances are amplified inside the boundary layer, figure 4.19. In addition, in the near-wall region, disturbances appear at frequencies typical of T-S waves and are amplified in the streamwise direction, figure 4.20b. These disturbances displayed different u_{rms} profiles from the other frequencies (figure 4.21 and 4.22).
8. Spanwise correlation measurements close to the $u_{rms,max}$ location indicate the presence of longitudinal streaky structures in the pre-transitional zone, figure 4.23. The average spanwise scale of the streaks is found to be much larger than the boundary layer thickness, ($> 10\delta$). Further, the streak spacing does not seem to vary in the downstream direction. The average wall-normal scale of the streak is found to be about 65% of the boundary layer thickness, figure 4.25.
9. Spanwise spacing of the streaks is observed to vary with the gap height h_w , figure 4.26. There appears to be a link between the frequency of disturbance and the spanwise spacing of the streak, figure 4.27.
10. The effect of Reynolds number is observed to be less significant for the cases considered. In particular, among the three Re_c values considered, the streak spacing is found to be similar for the two Re_c on the higher side, but a distinct behaviour is observed for the lowest Re_c , which was attributed to the change in the wake characteristics at low Re_c . On the other hand, the disturbance profile and the energy growth characteristics are found to be independent of the Reynolds number. Further investigations would be necessary to arrive at any concrete insights on the effect of Re_c .

By comparing the present observations with the transition characteristics of natural, bypass and cylinder wake-boundary layer interaction, summarised in table 4.5, it could be seen that the features observed in the current experiments do not correspond to one particular type of transition. Rather the present results show a mixed transitional behaviour in the aerofoil-wake boundary layer interaction. Specifically, for a lower gap ($h_w = 40$ mm), non-modal characteristics were predominantly observed. When the gap is increased to $h_w = 60$ mm, co-existence of both modal and non-modal characteristics was observed. For the height $h_w = 80$ mm, the transitional characteristics were primarily modal. Thus, it can be concluded that when the

Features	Natural Transiiton	Bypass transiiton	Cylinder wake-boundary layer interaction	Present experiment
Mean velocity profile	Blasius	Slightly deviated from Blasius	Slightly deviated from Blasius	Blasius
Urms profile	Near wall peak	Non-modal distribution	Non-modal distribution	Both non-modal and near-wall peak is observed for a selected bandwidth of frequency
Disturbance growth	Exponential	Algebraic	Initially exponential, later algebraic	Exponential
Streaky structure & its spanwise spacing	Absent	Present, order of boundary layer thickness	Present, order of boundary layer thickness	Present, much larger than boundary layer thickness

Table 4.5: Comparison of present transitional characteristics with the FST induced transition and cylinder wake induced transition.

gap is increased, the transition characteristics is observed to shift from non-modal to modal with mixed characteristics for intermediate gaps.

In the presence of such mixed transitional features, an understanding of the laminar breakdown process would be useful in establishing the transition mechanism in the aerofoil wake-boundary layer interaction. From the literature, it is generally observed that breakdown occurs when the amplitude of fluctuations, expressed as a fraction of the free-stream velocity, is greater than 1.5% (Fasel, 2002) and 10% (Westin et al., 1994; Balamurugan and Mandal, 2017) for natural and bypass transition respectively. However, in the present study, the amplitude of fluctuations corresponding to the T-S wave (near-wall peak) and the streamwise streaks are found to be approximately equal to 0.1% and 2% of the free-stream velocity. With these observations, it can be stated that either T-S wave or streamwise streaks alone would not be sufficient to induce laminar breakdown. Therefore, a combined instability of the T-S wave and streaks together may be responsible for inducing the transition onset.

Chapter 5

Linear stability analysis

Spatial linear stability analysis has been carried out on the measured wake-boundary layer profile. The aim of this numerical analysis is to verify whether the spatial amplification of the disturbance observed in the near-wall region (for $h_w = 60 \text{ mm}$) of spectrum is consistent with the presence of T-S waves, and how the wake deficit profile affects the growth rates of such modes.

5.1 Introduction

The fully turbulent wake acts as a source of forcing for disturbances in the boundary layer beneath. The frequency content of this forcing mechanism is broadband (similar to a turbulent distribution). This broadband forcing should lead to amplification of disturbances at some select frequencies within the boundary layer, based on its stability characteristics. Certainly, the presence of the wake would alter the stability characteristics but, as seen later, not to a significant degree. Linear stability has been used to analyse unsteady wakes ([Barkley, 2006](#); [Leontini et al., 2010](#)) and fully developed turbulent flows as well as the more usual steady, laminar flow. [Sreenivasan \(1988\)](#) used the concept of critical layers in fully developed turbulent boundary layers, which actually originated from linear stability theory. In this chapter, a local, spatial stability analysis of the measured wake profiles is described, starting with an outline of the approach, some validation examples, before discussing the results obtained for the present measured velocity profiles.

Linear stability theory is used to understand the evolution of infinitesimal perturbations in laminar flow by means of the linearized Navier-Stokes equations. To solve the linearized equation numerically with a reasonable computational cost, the parallel flow assumption is used, where streamwise flow gradients and the wall-normal mean velocity component is assumed to be zero. According to Squire's theorem, two-dimensional disturbances are more unstable than three-dimensional, hence the

most significant infinitesimal disturbance is assumed to be two-dimensional. By considering the two-dimensional disturbance as a wave form (equation 5.1-5.3) and substituting in the linearized non-dimensional Navier-Stokes equations, a fourth order differential equation can be obtained. This is the Orr-Sommerfeld equation (5.4); for a detailed derivation one can refer to Schmid and Henningson (2012).

$$\psi = \phi(y)e^{i(\alpha x - \omega t)} \quad (5.1)$$

$$\tilde{u} = \frac{\partial \psi}{\partial y} = \phi'(y)e^{i(\alpha x - \omega t)} \quad (5.2)$$

$$\tilde{v} = -\frac{\partial \psi}{\partial x} = \phi(y)e^{i(\alpha x - \omega t)}(-i\alpha) \quad (5.3)$$

$$[(D^2 - \alpha^2)(iU\alpha - i\omega) - i\alpha U'' - \frac{1}{Re_{\delta^*}}(D^2 - \alpha^2)^2]\tilde{v} = 0 \quad (5.4)$$

$$[iU(D^2 - \alpha^2) - iU'' - \frac{1}{\alpha Re_{\delta^*}}(D^2 - \alpha^2)^2]\tilde{v} = ic(D^2 - \alpha^2)\tilde{v} \quad (5.5)$$

Here, the disturbance equation is given in terms of streamfunction ψ . The perturbation mode shape, ϕ , is assumed to be a function of y alone. All quantities are dimensionless and the prime symbol and the symbol D both represent differentiation with respect to η ($= y/\delta^*$). α , ω & c represent the wave number in the streamwise (x) direction, angular frequency and phase velocity ($= \omega/\alpha$) respectively. By rearranging equation 5.4, the Orr-Sommerfeld equation can be seen as an eigenvalue problem, equation 5.5.

In general the eigenvalue problem formulated in equation 5.5 has solutions involving both complex frequency (ω) and wavenumber (α). In the case of open flows, like boundary layers and free shear flows, disturbances practically evolve in space rather than time, therefore the present aerofoil wake-boundary layer interaction is considered as a spatial problem and equation 5.5 is solved for complex streamwise wave number (α), by constraining ω to be real. It can be noted that α and differential operator, D in equation 5.5 appear raised to the power of 4. By applying a simple transformation (equation 5.6, suggested in Haj-Hariri, 1988), the fourth order non-linear eigenvalue problem can be reduced to a second order problem, given in equation 5.7.

$$\tilde{v} = \widehat{V}e^{-\alpha y} \quad (5.6)$$

$$(D^2 - 2\alpha D)(i\omega - i\alpha U)\widehat{V} + i\alpha U''\widehat{V} + \frac{1}{Re_{\delta^*}}(D^2 - 2\alpha D)^2\widehat{V} = 0 \quad (5.7)$$

This second order system is further reduced to two first order systems to yield a simpler, linear eigenvalue problem (Schmid and Henningson, 2012). This can be obtained by introducing the vector $(\alpha\widehat{V}, \widehat{V})$ which is described in equation (5.8).

$$\begin{bmatrix} -R_1 & R_0 \\ I & 0 \end{bmatrix} \begin{bmatrix} \alpha\widehat{V} \\ \widehat{V} \end{bmatrix} = \alpha \begin{bmatrix} R_2 & 0 \\ 0 & I \end{bmatrix} \begin{bmatrix} \alpha\widehat{V} \\ \widehat{V} \end{bmatrix} \quad (5.8)$$

where,

$$R_1 = -2i\omega D - \frac{4}{Re_{\delta^*}}D^3 - iUD^2 + iU''$$

$$R_2 = \frac{4}{Re_{\delta^*}}D^2 + 2iUD$$

$$R_0 = i\omega D^2 + \frac{1}{Re_{\delta^*}}D^4$$

To solve this eigenvalue problem $U(y)$, Re_{δ^*} and ω need to be specified to obtain the coefficients of the matrix. Further, defining the suitable set of boundary conditions for the mean flow, the solution procedure will yield an eigenfunction ($\phi(y)$ or \tilde{v}) and its corresponding complex eigenvalue (either α or c). The method of spatial discretisation of equation 5.8 plays an important role in determining the accuracy of the solution. In the present analysis, the Chebyshev spectral method is used to discretise the equation in the wall-normal direction, as is laid-out in Schmid and Henningson (2012). High accuracy and exponential rate of convergence can be achieved in spectral methods by expanding the eigenfunctions through Chebyshev polynomials. The computational grid used for the Chebyshev spectral method must lie in a domain $\xi \in [-1,1]$ so the semi-infinite physical domain is transformed into a finite computational domain, equation 5.9.

$$\eta = l \frac{1 - \xi}{1 + s + \xi} \quad (5.9)$$

where,

$$\xi = \cos\left(\frac{\pi j}{K}\right), \quad j = 0, 1, 2, \dots, K$$

$$s = \frac{2l}{\eta_e}, \quad l = \frac{\eta_e \eta_h}{\eta_e - 2\eta_h}, \quad \eta = [0, \eta_e]$$

One of the disadvantages of the spectral method is that the eigenspectrum contains a few mesh-dependent spurious modes. These modes can easily be identified by changing the number of Chebyshev polynomials used for the computation. In the present analysis, 201 Chebyshev polynomials are used. The validation of this numerical scheme and the results are discussed below.

5.2 Solver validation

Based on the above eigenvalue formulations and spectral discretisation technique, an Orr-sommerfeld code was written in MATLAB based on the algorithm of [Haj-Hariri, 1988](#); [Varghese, 2016](#); [Mitra, 2018](#) and was validated with two cases from the literature.

Blasius profile:

The classical problem of a boundary layer on a semi-infinite flat plate is first considered. The differential equation governing the flat plate boundary layer problem is given in equation 5.10. The nonlinear equation is numerically solved using Runge-Kutta based shooting method along with the boundary conditions given by $f(0) = 0$ and $f(\eta \rightarrow \infty) = 1$. As a result, the familiar self-similar Blasius profile is obtained and it is shown in figure 5.1.

$$\frac{1}{2}f(\eta)f''(\eta) + f'''(\eta) = 0 \tag{5.10}$$

where,

$$f'(\eta) = U = \bar{U}/U_0$$

$$\eta = \frac{y}{\sqrt{\frac{\nu x}{U_0}}}$$

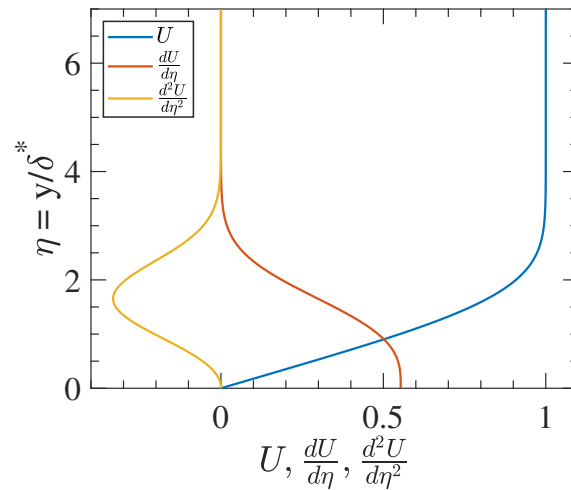


Figure 5.1: Blasius velocity profile and its derivatives.

The obtained Blasius profile $U(y)$ is then fed into the Orr-Sommerfeld code and the corresponding eigenvalue problem is solved for various values of Re_{δ^*} and ω . Here the eigenvalues are obtained in terms of complex phase velocity ($c = c_r + ic_i$). Here c_r describes the phase velocity of the applied disturbance and c_i determines whether the disturbance wave is amplified ($c_i > 0$) or damped ($c_i < 0$). Based on the obtained c_i values, a contour plot is generated and it is shown in figure 5.2.

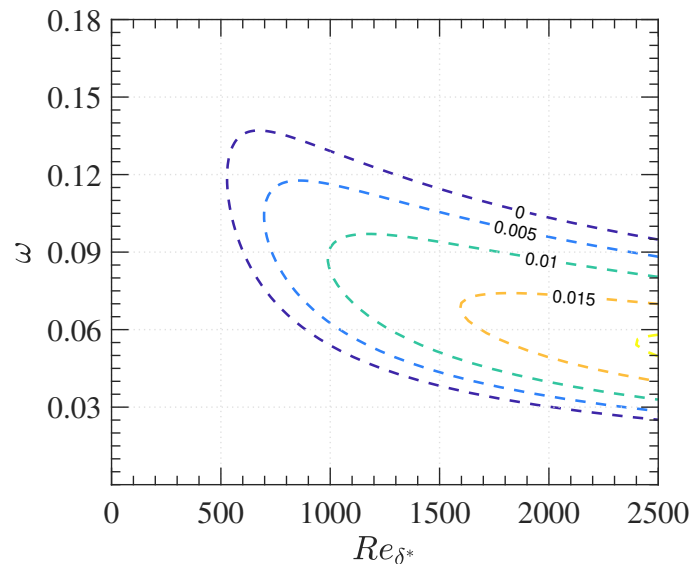


Figure 5.2: Neutral curve for Blasius profile - obtained by solving spatial Orr-Sommerfeld equation. The labels in the curves are corresponding c_i values.

The contour with the label $c_i = 0$ is referred to as the neutral curve. The other curves shown in the figure with positive c_i values ($c_i > 0$) indicates unstable regions, whereas the regions outside the neutral curve are stable ($c_i < 0$). The minimum

Reynolds number where $c_i = 0$ is referred as critical Reynolds number. For a flow over a flat plate with Blasius boundary layer profile, the critical Reynolds number was found to be 520 by [Jordinson \(1970\)](#). It can be seen from figure 5.2 that the present solver also yields a very similar value of critical Reynolds number.

Further, the present eigenvalues are compared with the values obtained from Runge-Kutta based shooting technique (provided by Prof. Michael Gaster) and the values match satisfactorily as shown in table 5.1. Gaster's results are obtained using a shooting method which converges on a single eigenvalue, rather than the complete spectrum yielded by the present approach. This explains the small discrepancies in the comparisons.

Re_{δ^*}	ω	$\alpha_r(\text{MG})$	α_r (present)	$\alpha_i(\text{MG})$	α_i (present)
1000	0.2	0.479815584	0.474494124	0.057954546	0.060144809
1000	0.14999	0.394003281	0.390611284	0.010494305	0.010410943
1000	0.1	0.279827398	0.276166985	-0.00728719	-0.007369102
1000	0.05	0.158272189	0.153389833	0.001908451	0.00120584

Table 5.1: Compared the eigenvalues of Blasius profile obtained from Prof. Michael Gaster (MG) with the present solver values.

Wake-boundary layer profile:

As the present experiments involve confluent wake-boundary layer in the flow, a second validation case was chosen from a literature study, [Liou and Liu \(2001\)](#) dealing with local spatial stability analysis of such confluent boundary layers. The base flow velocity profile is obtained by superposition of the Blasius boundary layer profile and the Gaussian wake profile (equation 5.11). The superposition was done carefully to avoid discontinuities in the wall-normal derivatives of the profiles. The base flow velocity profile and its derivatives are shown in figure 5.3.

$$U = 1 - 0.6e^{-0.5(y-h_w)^2} \quad (5.11)$$

The geometry of the wake, Re_{δ^*} and ω are similar to those reported in [Liou and Liu \(2001\)](#). By solving the Orr-Sommerfeld equation for spatial stability using the present solver, three discrete unstable modes are noticed; one boundary layer mode and two wake modes (shown in figure 5.4) The wake modes 1 and 2 correspond to antisymmetric and symmetric modes respectively. These three unstable modes

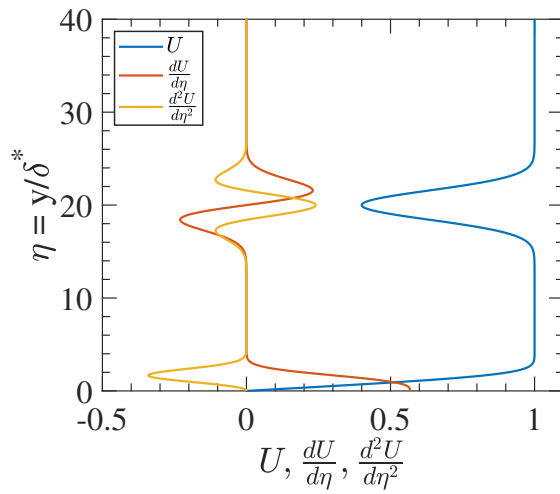


Figure 5.3: Wake boundary layer profile and its derivative.

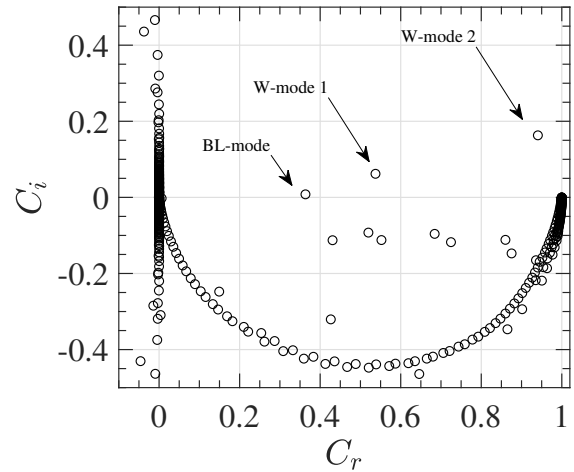


Figure 5.4: Eigenvalue spectrum for the case $Re_{\delta^*} = 998$, $\omega = 0.112$ for the velocity profile in figure 5.3. BL & W - stands for boundary layer and wake modes.

obtained here are also reported by [Liou and Liu \(2001\)](#). For further validation, the eigenfunctions corresponding to the three unstable modes are compared and are shown in figures 5.5a and 5.6.

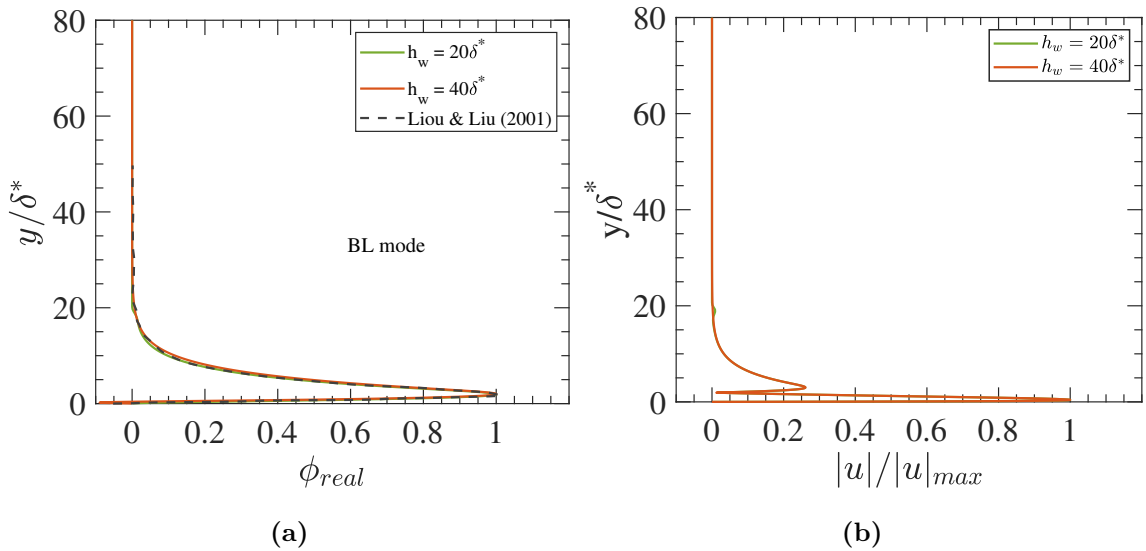


Figure 5.5: (a) Eigenfunctions for the boundary layer mode in figure 5.4 and its corresponding (b) streamwise fluctuation profiles for two different gaps.

In both the figures, the eigenfunctions are plotted for two different wake heights with their values normalised with their corresponding maximum. From the com-

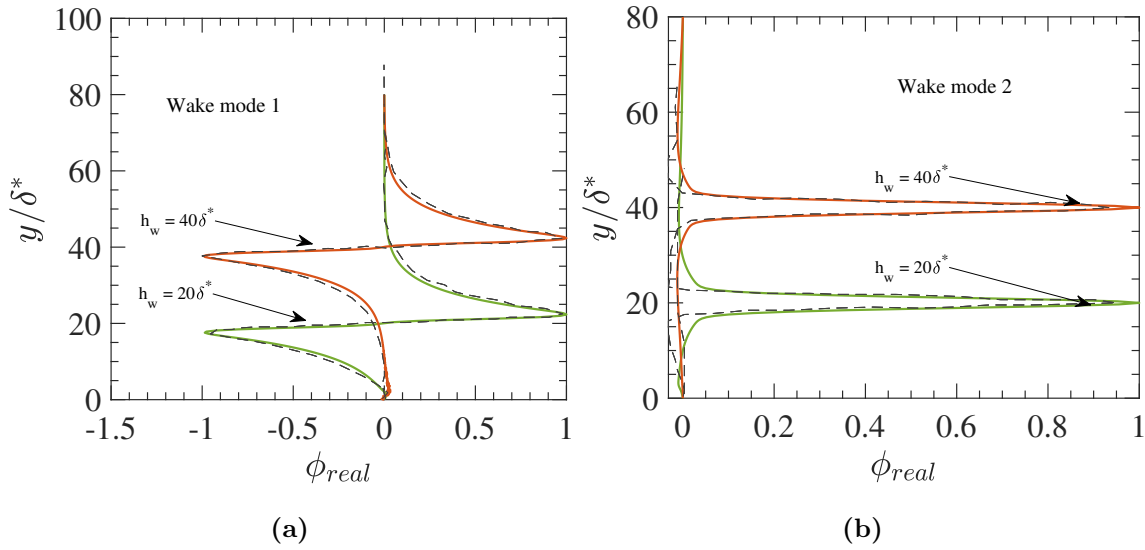


Figure 5.6: Eigenfunctions for the wake mode 1 and 2 in figure 5.4. Dashed line correspond to Liou and Liu (2001).

parison plots, a reasonable match between the present results (solid lines) and the literature (dashed lines) can be observed.

5.3 Base flow velocity profile

Having validated the solver, the spatial stability analysis is applied to the present experimental results, focussing on the base flow velocity profile corresponding to $h_w = 60$ mm. From the power spectral distribution plots for $h_w = 40$ and 60 mm discussed in chapter 4, clear evidence is seen of the amplification of T-S wave like disturbances for the case $h_w = 60$ mm. Hence, the base flow velocity profile corresponding to $h_w = 60$ mm is chosen for the present spatial stability analysis.

To obtain a smooth velocity profile without any discontinuities in the derivatives, a confluent wake-boundary layer profile is generated numerically to match the measured wake profile. There is a considerable potential core between the wake region and boundary layer for the case $h_w = 60$ mm. The potential core suggests that the wake and the boundary layer have minimal effect on each other in a time-averaged sense. From this observation, it is assumed that the downstream wake growth is not distorted due to the boundary layer. Therefore, in order to obtain the confluent wake-boundary layer, the velocity profiles of the aerofoil wake and the boundary layer are superposed. The procedure followed for the superposition is described below.

From the data measured for the pure aerofoil wake, reported in chapter 2, the characteristics of the aerofoil wake are obtained in terms of decaying defect velocity and development of wake thickness in the downstream direction, which are shown in figure 5.7 respectively. Through a curve fitting technique, expressions for the defect velocity and wake thickness can be obtained as given in equations 5.12 and 5.13 respectively. With this information, and using the self-similarity equation for aerofoil wake given by equation 5.14 (Wynanski et al., 1986 and figure 5.8), the velocity profiles of the wake at any streamwise station can be obtained.

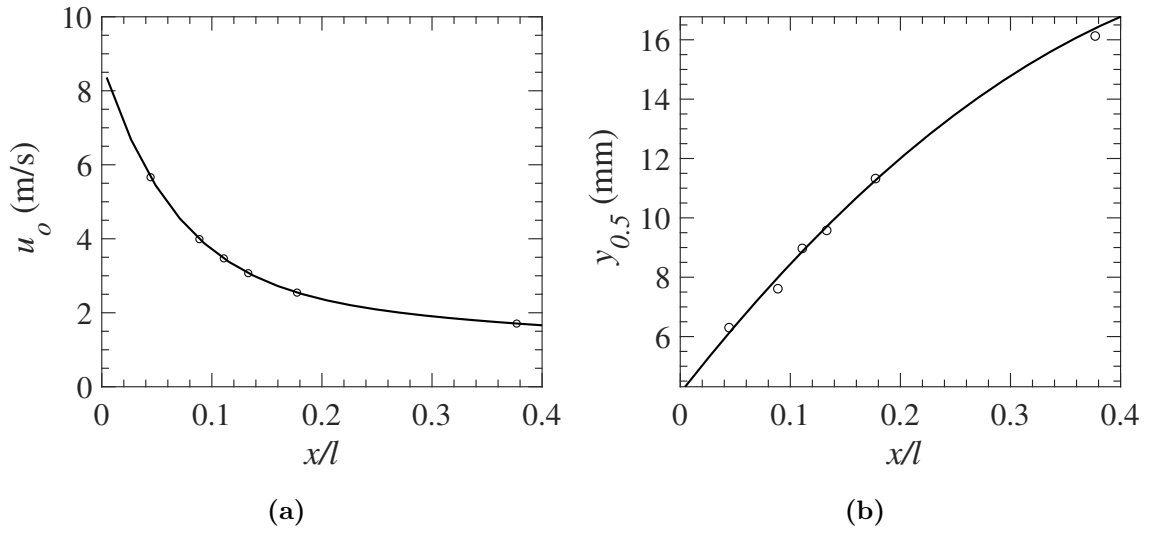


Figure 5.7: (a) Decay of defect velocity(u_0) and (b) Position of $0.5u_0$ of the wake in the downstream distance.

$$u_0 = 6.26 \exp[-0.00648(x/l)] + 2.506 \exp[-0.000468(x/l)] \quad (5.12)$$

$$y_{0.5} = -7.7 \times 10^{-6}(x/l)^2 + 0.024(x/l) + 4.1 \quad (5.13)$$

$$f(\eta_{0.5}) = \frac{U_0 - \bar{U}}{u_0} = \exp[-0.637(\eta_{0.5})^2 - 0.056(\eta_{0.5})^4] \quad (5.14)$$

where,

$$\eta_{0.5} = (y/y_{0.5})$$

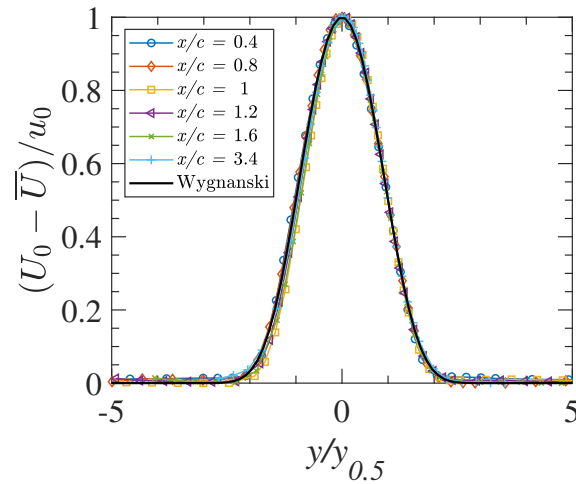


Figure 5.8: Self-similar profile of the aerofoil wake.

From chapter 4, it is known that the boundary layer profiles for case $h_w = 60$ mm matches the Blasius solution. Having the velocity profiles for the wake and the boundary layer, the velocity profile of the confluent wake-boundary layer can be obtained. The resulting profiles of the confluent wake-boundary layer for various streamwise stations are shown in figure 5.9

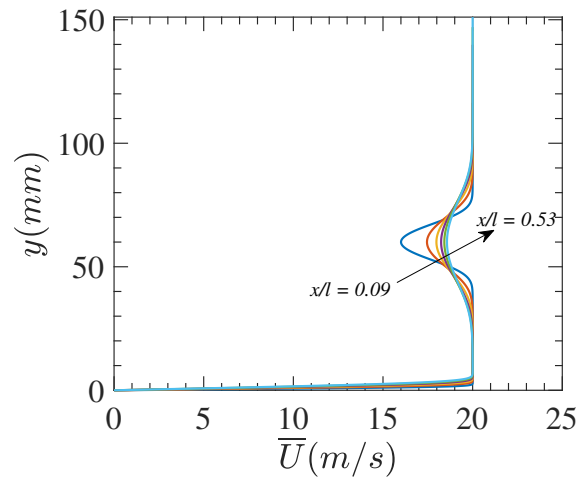


Figure 5.9: Numerically generated confluent wake boundary layer profile for the case $h_w = 60$ mm.

The combined boundary layer and wake profiles shown in figure 5.9 are derived for various streamwise stations ranging from $x/l = 0.09 - 0.53$. The corresponding wall-normal derivatives are shown in figure 5.10.

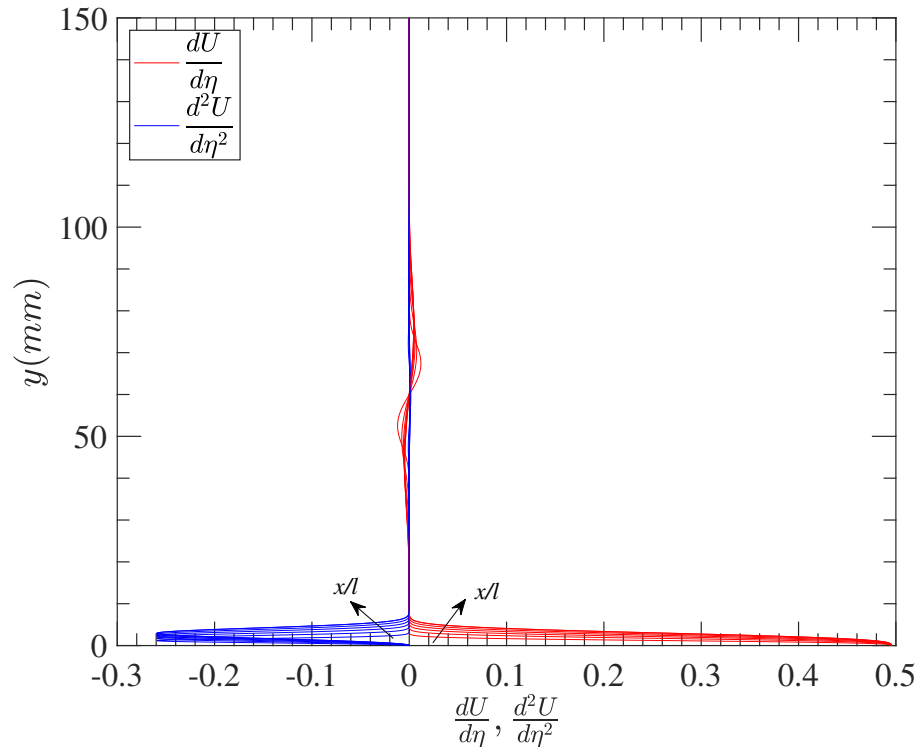


Figure 5.10: First and second derivatives of the confluent wake-boundary layer shown in figure 5.9.

5.4 Results and discussion

By solving the Orr-Sommerfeld equation with the obtained base flow velocity profiles for various streamwise stations, the spatial growth rate ($-\alpha_i$) of the unstable boundary layer mode is obtained as shown in figure 5.11a. It can be observed that the maximum growth rate increases in the downstream direction, while its corresponding frequency decreases. The same trends were previously noted (chapter 4) for the mid-range frequency of the streamwise spectral distribution, which is reproduced again in figure 5.12.

To study the effect of the wake on boundary layer stability, the growth rate of the Blasius mode (i.e. in the absence of the wake) is compared with that of the presently-computed boundary layer mode (i.e. in the presence of the wake), shown in figure 5.11b. Firstly, from figure 5.11b, the growth rate trend for both the cases is similar. However, the maximum growth rate of the boundary layer mode (solid line) is greater than the growth rate of the Blasius mode (dashed line) and the frequency of the most-amplified boundary layer mode is slightly higher than for the Blasius mode. The difference between the growth rates of the two modes tends to

decrease as one moves downstream. It is clear that the presence of the wake above the boundary layer amplifies the growth rates of the boundary layer mode and, as the wake decays (weakens) moving downstream, the growth rates of the boundary layer mode tend to those of the Blasius mode.

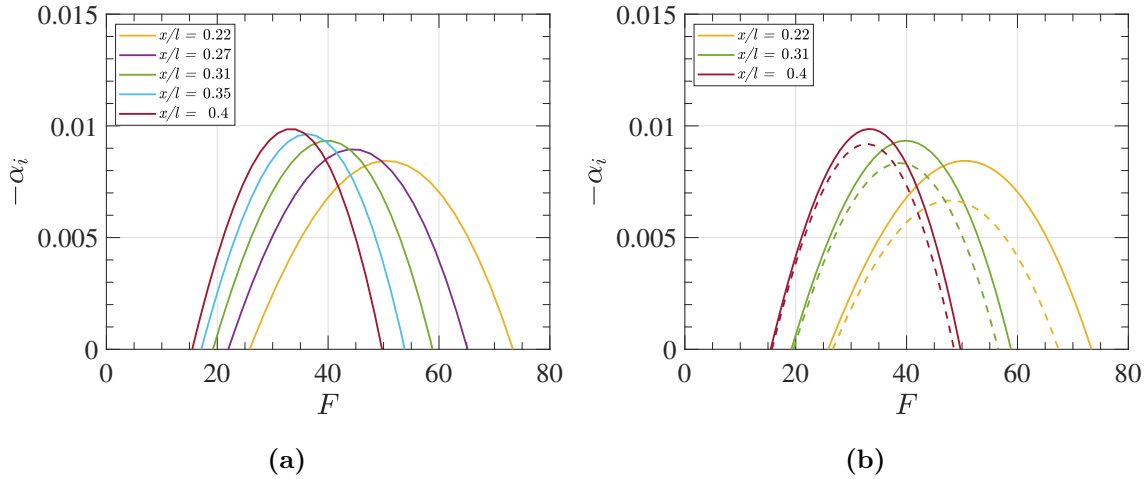


Figure 5.11: (a) Growth rate of the boundary layer mode from the confluent boundary layer profiles, which is (b) compared with the growth rate of the Blasius profile (dashed line).

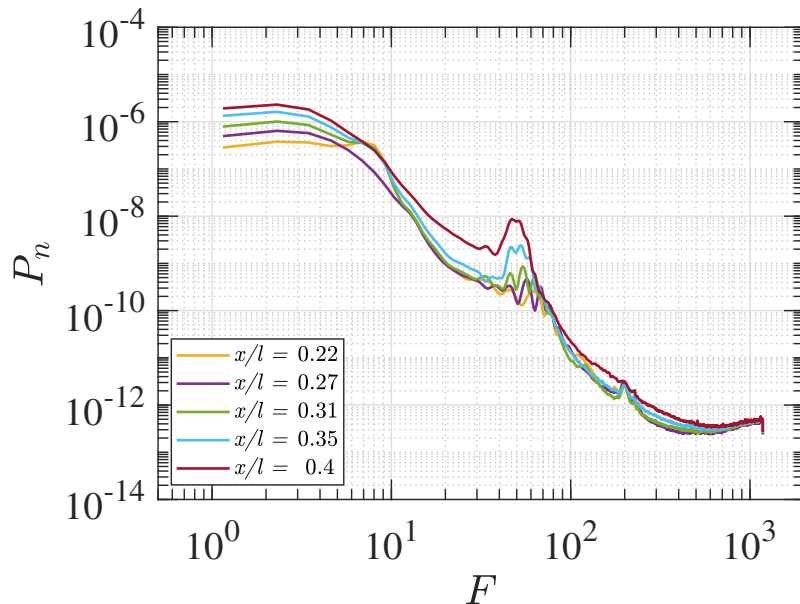


Figure 5.12: Normalised power spectrum measured at $y/\delta = 0.2$ for the case $h_w = 60$ mm.

To compare the mid-range frequencies observed in the spectrum (figure 5.12) with those of the modal disturbances (T-S waves), the N -factor of the boundary

layer mode is calculated. The N -factor or e^N technique is a method based on linear stability theory to predict the transition location and it was first proposed by [Smith \(1956\)](#) and [Van Ingen \(1956\)](#). A brief explanation of this method is given below followed by an N -factor calculation on the present case.

N is defined as the amplitude factor of the disturbance, which is obtained using the ratio of amplitudes of the disturbance, A and $A+dA$ at two streamwise locations, x and $x+dx$ respectively. The amplitudes of the disturbance are given by $A = e^{-\alpha_i x}$ and $A + dA = e^{-\alpha_i(x+dx)}$. The ratio between these two amplitudes provide the information on the disturbance (wave) growth and is given by:

$$\frac{A + dA}{A} = e^{-\alpha_i(x+dx)} \quad (5.15)$$

or

$$\ln(A + dA) - \ln(A) = d[\ln(A)] = -\alpha_i dx \quad (5.16)$$

By integrating the above equation from x_0 , which is the position where the instability starts to grow, to the location x , one can obtain the expression for the N -factor as:

$$N = \int_{x_0}^x -\alpha_i dx \quad (5.17)$$

From equation 5.17, for a given frequency (ω), the amplification factor N can be calculated for various streamwise stations. The results are plotted in figure 5.13. Each coloured line in the figure corresponds to a frequency (ω) chosen from the range 0.05 to 0.09 in a step size of 0.001. From the envelope of the set of curves for various ω , the maximum amplification factor (N_m) is obtained.

It can be hypothesized that, if the frequency of the maximum N -factor of the boundary layer mode (from figure 5.13) is comparable to the spatial amplification of the mid-range frequencies in the experimental spectrum (from figure 5.12), then it would be a strong indication that T-S waves are present in the present experiment. Table 5.2 provides the comparison between the two frequencies for various streamwise stations.

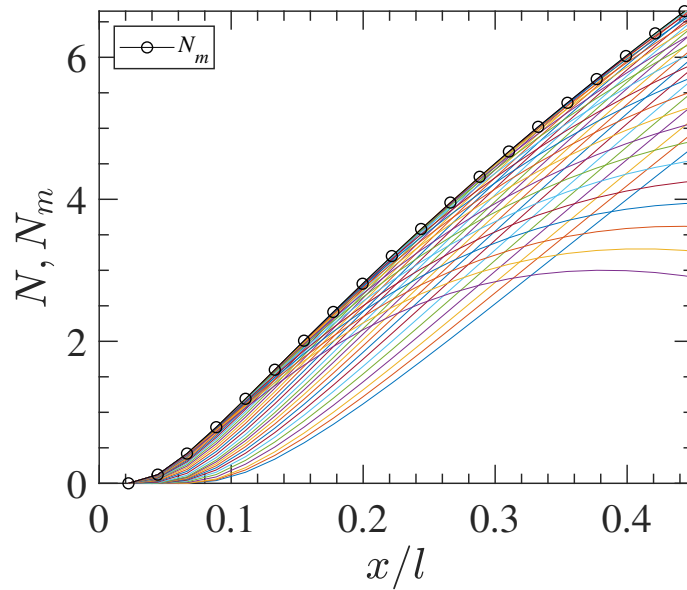


Figure 5.13: N, N_m -factor values of the boundary layer mode obtained from the wake boundary layer profile.

x (mm)	x/l	δ^* (mm)	ω at N_m	F from ω	F from experiment
500	0.22	1.0062	0.07483	56	61
600	0.27	1.1023	0.07275	50	56
700	0.31	1.1906	0.07172	45	53
800	0.35	1.2728	0.06965	41	52
900	0.4	1.3500	0.06862	39	47

Table 5.2: Comparison of the dominant frequency from the growth rate of the boundary layer mode with the frequency corresponding to the amplification of mid-range frequency in figure 5.12.

In table 5.2, using

$$F = \frac{2\pi f\nu}{U_0^2} = \frac{2\pi f(\delta^*/U_0)}{U_0\delta^*/\nu} = \frac{\omega}{Re_{\delta^*}} \times 10^6 \quad (5.18)$$

the angular frequency (ω) is transformed into the non-dimensional frequency (F). Table 5.2 shows that that the frequencies obtained from the N -factors and those from the spectrum are comparable to each other. The small differences may be associated with slight mismatches between boundary layer profiles measured in the experiment and used for the computation. Despite these differences, the decreasing trend of the frequency in the downstream distance is observed in both cases. However, one can certainly argue that the mid-range frequencies observed in the experiment (figure.

5.12) correspond well with the predicted T-S frequencies. Thus, from the above observation along with one of the inferences from the previous chapter, i.e., the near-wall peak occurring in mid-range frequencies (figure 4.22), it can be stated that T-S waves are likely to be present.

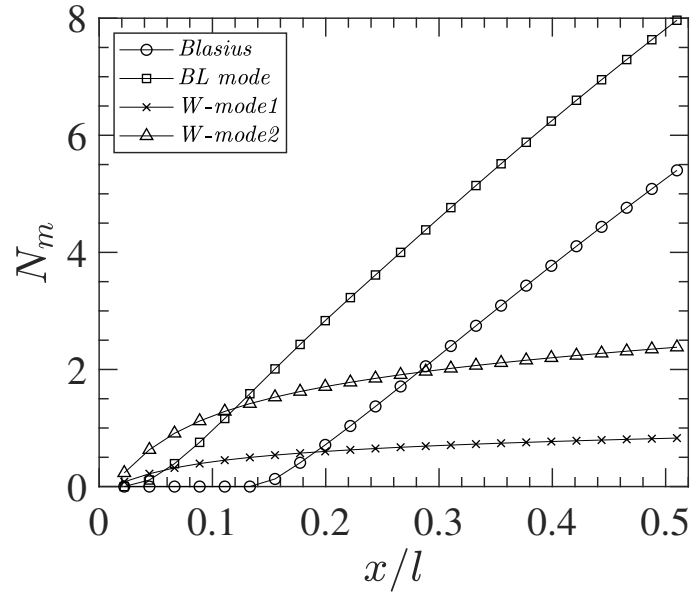


Figure 5.14: N_m -Factor for the three different modes of the confluent wake-boundary layer and Blasius boundary layer profile

To ascertain how the growth of the wake modes differs from the Blasius and boundary layer modes, the calculated N_m for all the cases are compared in figure 5.14. N_m for the boundary layer mode is higher than that for the Blasius mode by a value of 2. In figure. 5.11b, it was observed that the spatial growth rates of the boundary layer modes were higher than that of the Blasius mode, which is why N_m is higher for the boundary layer modes. This indicates that the presence of wake above the boundary layer would result in earlier natural transition in comparison to the Blasius boundary layer case. So, as well as stimulating non-modal growth, the wake also plays an important role in growth of the natural boundary layer modes and hence transition onset.

Chapter 6

Conclusions and recommendations

In the present thesis, an attempt is made to gain insight into the laminar-turbulent transitional characteristics of the aerofoil wake-boundary layer interaction, which is prevalent in multi-element aerofoils and turbomachines. The work is novel in featuring a fully-developed turbulent wake acting at a distance from an otherwise undisturbed laminar boundary layer with very low turbulence intensity in the surrounding field.

Two original contributions are the development of a new, rational procedure for measuring the intermittency in the transition zone and the evidence of both modal and non-modal transition mechanisms in this flow field. The key findings and conclusions with regards to the above two contributions are discussed below.

Transitional intermittency distribution

The extraction of intermittency information from the flow helps in determining the level of turbulence in the transition zone and further to determine the length of the transition zone. It has been demonstrated that the available intermittency measurement techniques in the literature are subjective due to their dependence on an arbitrary threshold value. In the present work, a rational technique for the intermittency measurement, particularly in the streamwise direction, is proposed to overcome the subjectivity involved in other methods. The underlying idea is based on a simple assumption that the magnitude of the laminar perturbation at the transition onset point is considered as the maximum laminar perturbation throughout the flow. In the present work, the transition onset point was identified using a combined third moment ($\overline{u^3}$) and skewness ($\overline{u^3}/\overline{u_{rms}^3}$) based approach, which in turn helps to determine the maximum laminar perturbation. Subsequently, by filtering the maximum laminar perturbation from the transitional flow, the intermittency

distribution can be obtained.

The resulting values of the intermittency are validated against the values obtained using the dual-slope method (Kuan and Wang, 1990), which is a commonly used method in recent times. It is observed that a reasonable match between the two methods is achieved. However, it should be noted that the dual-slope method is itself arbitrary in terms of selecting a threshold value. It is recommended that the approach proposed in this thesis, which employs a rigorous method for threshold selection, would be a more robust alternative for intermittency determination in the streamwise direction.

The developed measures of skewness and intermittency were further used to analyse the effect of the gap on the transition onset and breakdown points and the length of the transition zone. A surprising finding is that all the above three parameters are observed to vary linearly with respect to the gap, despite the nonlinear growth of wake and boundary thicknesses in the downstream direction. A good agreement has been demonstrated between the intermittency distribution obtained using the hypothesis of concentrated breakdown (Narasimha, 1957) and the present results.

Laminar-turbulent transitional characteristics

The transitional characteristics of aerofoil wake-boundary layer interaction were studied using an upstream aerofoil- downstream flat plate configuration. As stated earlier, this is believed to be the first study to use an aerofoil-flat plate configuration. The flow field analysis was focused on the pre-transitional zone in order to study the initial disturbance growth.

Two cases (aerofoil-plate gap heights of $h_w = 40$ and 60 mm) were considered for particular attention due to their larger pre-transitional zone length, which in turn allows for detailed analysis of the disturbance growth. An emphasis was placed on elucidating the differences between the transition characteristics of the present configuration with that of the other transition mechanisms established in the literature (FST induced transition and cylinder wake-boundary layer interaction).

From the analysis results, it was observed that the upstream wake contains a broad bandwidth of disturbances, dominated by mid-range frequencies (80-300 Hz), which then interact with the downstream boundary layer and induces laminar-turbulent transition. Further, the bandwidth of the wake disturbance is found to

vary with respect to the proximity (gap) of the aerofoil, which in turn influences the level of turbulent intensity with which the interaction occurs. As a consequence, the flow in the pre-transitional zone is observed to exhibit both the natural and bypass transition characteristics. In particular, the streamwise disturbance growth was exponential in character, the power spectral density confirming that the spatial amplification of the disturbance was similar to that of T-S wave growth as predicted by linear stability analysis. On the other hand, in the same region, two distinct features of bypass transition were observed, namely the non-modal disturbance profile and the presence of a longitudinal streaky structure. Surprisingly, the spanwise spacing of the streaky structure is much larger than that predicted by transient growth theory and it is found to increase as the aerofoil is moved further away from the plate. Such a variation of the spacing with respect to the gap also correlates with the bandwidth of the frequency with which the disturbance acts on the boundary layer.

In the case of FST induced transition, it was reported that the longitudinal streaky structure originates from the leading edge (Kendall, 1985; Westin et al., 1994). On the other hand in the present experiment, the origin of the streaky structure appears to be controlled by the proximity of the wake. Also, it is demonstrated for the cases $h_w = 60$ & 80 mm, that there is a gradual transformation of modal to non-modal type of disturbance profile and it appears to occur more or less at the streamwise location where the turbulent intensity at the edge of the boundary layer attains 0.1%. On a different note, this part of the flow with borderline characteristics would be very useful for studying the receptivity mechanism and the streak formation in detail, and the present experimental set up allows the length of the initial receptivity region to be controlled.

From the above results, it can be established the transition mechanism associated with the aerofoil-wake boundary layer interaction possesses mixed characteristics and is significantly different to the transition characteristics associated with cylinder wake-boundary layer interaction. The aerofoil-wake boundary layer interaction exhibits both exponential disturbance growth as well as non-modal disturbance profiles and widely-spaced streaky structures. These observations indicate that the underlying transition mechanism may be different in nature to that induced by FST.

Progress towards objective

Now, returning to the objective of the thesis, how would the present results of intermittency distribution and laminar-turbulent transitional characteristics help to increase the accuracy of $C_{L,max}$ prediction? The present measurements have revealed some new flow physics in the pre-transitional zone which need to be included, at some point, in the future CFD models used for high-lift systems analysis and design. For example, from the linear stability calculation, it is observed that there is a constant shift in the N_m -factor value for the wake-boundary layer profile when compared with the boundary layer profile alone. By repeating this calculation for various wake geometries, a correlation can be obtained between N_m and the wake geometry, which would help to determine the transition onset for the multi-element aerofoil case. On the other hand, in the case of commercial transition models (e.g. γ - θ model, [Menter et al. 2006](#)), transition onset and length of the transition zone are obtained using an empirical correlation function. By validating the solver with the present results for transition onset and transition length, more reliable correlation functions could be obtained.

However, the new knowledge will not be sufficient to create a complete model of wake-boundary layer interaction for accurate transition prediction on multi-element aerofoils. There are other factors (e.g. flow curvature, pressure gradients, compressibility, multiple wake interaction, sweep) which need to be considered before a better model would be available.

Recommendations for further work

1. Variation of spanwise spacing of the streaky structures, as the aerofoil gap (h_w) and Reynolds number were varied, was observed in the present work. The reasons behind this variation are not clear, however it appears that a link exists between the frequencies of the dominating disturbances and the spanwise spacing. This could potentially be studied by designing a separate experiment whereby the upstream disturbance frequencies can be varied in a controlled fashion.
2. Additional insight could be derived by conducting further experiments with the aerofoil at non-zero angles of attack, leading to an interaction of asymmetric wake with the downstream boundary layer, as would be the case in a high-lift system. An asymmetrical turbulent wake displays an interesting phenomenon

called counter gradient diffusion (i.e., turbulent diffusion takes place against the mean velocity gradient, resulting in a transfer of energy from the turbulence to mean flow), thereby exposing additional phenomena which may be relevant to the real problem.

3. Another interesting study would be to investigate the effect of an upstream aerofoil wake on a downstream body which is more realistic than a zero-pressure gradient flat plate. To achieve this, an experiment can be designed by imposing a user-specified pressure gradient (favourable or adverse) on the flat plate.
4. Most of the FST induced transition studies in the literature are carried out by placing the grid upstream of the leading edge and covering the whole test section. In such a case, the interaction of the turbulence from the free-stream with the flat plate starts at the leading edge. Instead, if the grid is placed above the leading edge as similar to the position of the aerofoil in the present experiment, it would lead to an interaction of isotropic turbulence with the flat plate boundary layer downstream of the leading edge. Such a study would help to investigate the receptivity mechanism in detail.

Appendix A

Uncertainty analysis

In this section, uncertainty estimates on the surface pressure measurements and velocity measurements from pitot static tube/hot wire anemometry are carried out. For the calculation, standard ISO uncertainty model (based on [Bell, 1999](#) and [Jørgensen, 2005](#)) has been used which combines all the uncertainties from each input variable and gives the total uncertainty.

The standard uncertainty of any individual measurement, u_s is defined based on the standard deviation, S and is given by

$$u_s = \frac{S}{\sqrt{n}} \quad (\text{A.1})$$

Where S is the standard deviation given by

$$S = \sqrt{\frac{\sum_{i=1}^n (x_i - \bar{x})^2}{(n-1)}} \quad (\text{A.2})$$

Here, n is the number of sample measured, x_i is the result of the i^{th} measurement and \bar{x} is the arithmetic mean of all x_i .

A second type of standard uncertainty, termed as type B uncertainty is used if the number of sample measurements are scarce. Using this type, one can obtain the upper and lower limits of uncertainty. The type B uncertainty is defined as

$$u_s = \frac{a}{\sqrt{3}} \quad (\text{A.3})$$

Where a is the semi-range between the upper and lower limits.

The combined standard uncertainty of a quantity can be determined by summation in quadrature with the uncertainties corresponding to the individual input variables. For a function $Y = f(X_1, X_2, \dots, X_N)$, the combined standard uncertainty, $u_c(Y)$ is given as

$$u_c(Y) = \sqrt{\left[\frac{\partial Y}{\partial X_1} u_s(X_1)\right]^2 + \left[\frac{\partial Y}{\partial X_2} u_s(X_2)\right]^2 + \dots + \left[\frac{\partial Y}{\partial X_N} u_s(X_N)\right]^2} \quad (\text{A.4})$$

Here, the function Y represents the output quantity of interest which possesses several sources of uncertainties arising from variables X_1, X_2, \dots, X_N . $u_s(X_1), u_s(X_2), \dots, u_s(X_N)$ denotes the standard uncertainties of the individual sources. The combined uncertainty can be expressed in summation form as below.

$$u_c(Y) = \sqrt{\sum_{i=1}^N \left(\frac{\partial Y}{\partial X_i}\right)^2 u_s(X_i)^2} \quad (\text{A.5})$$

The relative combined standard uncertainty can be obtained as follows

$$\frac{u_c(Y)}{Y} = \sqrt{\sum_{i=1}^N \left(\frac{\partial Y}{\partial X_i}\right)^2 \frac{u_s(X_i)^2}{Y^2}} \quad (\text{A.6})$$

The combined standard uncertainty, u_c is often multiplied by a coverage factor k to obtain expanded combined uncertainty, u_e . The coverage factor k is calculated based on the error distribution (Gaussian or rectangular).

$$u_e = K_c \frac{u_c(Y)}{Y} \quad (\text{A.7})$$

In the present experiments, the quantities of interest for uncertainty calculations are the coefficient of pressure and velocities from pitot tube/hot wire.

The coefficient of pressure is given as

$$C_p = \frac{p_d}{1/2\rho U_0^2} \quad (\text{A.8})$$

where, p_d , ρ and U_0 are the pressure, density and velocity respectively.

Using equation A.6, the combined relative standard uncertainty of the coefficient of pressure can be obtained as

$$\frac{u_c(C_p)}{C_p} = \sqrt{\left[\frac{u_s(p_d)}{p_d}\right]^2 + \left[\frac{u_s(\rho)}{\rho}\right]^2 + \left[\frac{2u_s(U_0)}{U_0}\right]^2} \quad (\text{A.9})$$

The relative standard uncertainty for the density can be obtained using the ideal gas equation $p = \rho RT$ and is given by

$$\frac{u_s(\rho)}{\rho} = \sqrt{\left[\frac{u_s(p)}{p}\right]^2 + \left[\frac{u_s(T)}{T}\right]^2} \quad (\text{A.10})$$

The relative standard uncertainty for the velocity can be obtained from the dynamic pressure equation $q_\infty = \frac{1}{2}\rho U_0^2$ and is given by

$$\frac{u_s(U_0)}{U_0} = \sqrt{\left[\frac{\frac{1}{2}u_s(q_\infty)}{q_\infty}\right]^2 + \left[\frac{\frac{1}{2}u_s(\rho)}{\rho}\right]^2} \quad (\text{A.11})$$

The standard uncertainties for the differential static pressure and the dynamic pressure are obtained directly from the measurements using the formula (A.1 & A.3). The standard uncertainties and their relative values for all the variables are shown in the table below.

Variable, X	Reference	u_s type	$u_s(X)$	$u_s(X)/X$
p_d	2.7 pa	Type A	0.001	0.37%
p	101325 pa	Type A	0.0004	0.04%
q_∞	246 pa	Type B ($1/\sqrt{3}$)	0.0682	0.02%
T	20°C	Type B ($1/\sqrt{3}$)	0.0708	0.35%

Table A.1: Uncertainty estimates of surface pressure distribution

The relative combined uncertainty estimate of C_p is found as 0.62%

Further, the expanded combined uncertainty for a confidence level of 95% is 1.2%

Next, the relative standard uncertainty for the velocity measured using a hot wire is obtained. The sources of uncertainty for the hot wire measurements stem from calibration and data acquisition. First, the individual standard uncertainties from the sources are calculated and are given by

$$u_s(U_{calib}) = \frac{S(U_{pitot})}{\sqrt{n}} \quad (\text{A.12})$$

$$u_s(U_{fit}) = \frac{S(U_{linear})}{\sqrt{n}} \quad (\text{A.13})$$

$$u_s(U_{A/D}) = K_c \frac{E_{range}}{2^n} \frac{\partial u}{\partial E} \quad (\text{A.14})$$

$U_s(U_{calib})$, $u_s(U_{fit})$ and $u_s(U_{A/D})$ are the individual uncertainties corresponding to the errors in the calibration, linearisation and analogue to digital data acquisition. In the above expression, E_{range} represents measured voltage. The combined standard uncertainty for the velocity obtained from the hot wire is then calculated as

$$U_s(U) = \sqrt{[u_s(U_{calib})]^2 + [u_s(U_{fit})]^2 + [u_s(U_{A/D})]^2} \quad (\text{A.15})$$

From the present measurements, for 20 m/s, the individual uncertainties, $U_s(U_{calib})$, $u_s(U_{fit})$ and $u_s(U_{A/D})$ are obtained as 0.06 , 0.0095 and 0.0035 m/s. Further, the combined relative standard uncertainty for the hot-wire velocity is obtained as 0.3%.

Bibliography

- Abu-Ghannam, B. and Shaw, R. (1980), ‘Natural transition of boundary layers—the effects of turbulence, pressure gradient, and flow history’, *Journal of Mechanical Engineering Science* **22**(5), 213–228.
- Anderson, J. D. (1999), *Aircraft performance and design*, McGraw-Hill Science/Engineering/Math.
- Andersson, P., Berggren, M. and Henningson, D. S. (1999), ‘Optimal disturbances and bypass transition in boundary layers’, *Physics of Fluids* **11**(1), 134–150.
- Arnal, D. and Juillen, J. (1978), ‘Experimental contribution to the study of the receptivity of a laminar limit layer, to the turbulence of the general flow’, *ONERA, Technical Report* (1/5018).
- Balamurugan, G. and Mandal, A. (2017), ‘Experiments on localized secondary instability in bypass boundary layer transition’, *Journal of Fluid Mechanics* **817**, 217–263.
- Balint, J.-L., Wallace, J. M. and Vukoslavčević, P. (1991), ‘The velocity and vorticity vector fields of a turbulent boundary layer. part 2. statistical properties’, *Journal of Fluid Mechanics* **228**, 53–86.
- Barkley, D. (2006), ‘Linear analysis of the cylinder wake mean flow’, *EPL (Europhysics Letters)* **75**(5), 750.
- Bell, S. (1999), ‘A beginner’s guide to uncertainty of measurement’, *Measurement good practice guide* **11**, 1.
- Bertelrud, A. (1998), Transition on a three-element high lift configuration at high Reynolds numbers, in ‘36th AIAA Aerospace Sciences Meeting and Exhibit’, p. 703.
- Bertelrud, A. and Anders, J. (2002), ‘Transition Documentation on a Three-Element High-Lift Configuration at High Reynolds Numbers—Analysis’, *NASA CR-2002-211438*.

- Blair, M. (1992), ‘Boundary-layer transition in accelerating flows with intense freestream turbulence: Part 2—The zone of intermittent turbulence’, *Journal of Fluids Engineering* **114**(3), 322–332.
- Boiko, A., Westin, K., Klingmann, B., Kozlov, V. and Alfredsson, P. (1994), ‘Experiments in a boundary layer subjected to free stream turbulence: Part 2- The role of TS-waves in the transition process’, *Journal of Fluid Mechanics* **281**, 219–245.
- Brandt, L., Schlatter, P. and Henningson, D. S. (2004), ‘Transition in boundary layers subject to free-stream turbulence’, *Journal of Fluid Mechanics* **517**, 167–198.
- Bruun, H. H. (1996), *Hot-wire anemometry: principles and signal analysis*, IOP Publishing.
- Canepa, E., Ubaldi, M. and Zunino, P. (2002), Experiences in the application of intermittency detection techniques to hot-film signals in transitional boundary layers, *in* ‘The 16th Symposium on Measuring Techniques in Transonic and Supersonic Flow in Cascades and Turbomachines’, pp. 2077–2085.
- Corrsin, S. (1943), ‘Investigation of flow in an axially symmetric heated jet in air’, *NACA Wartime Reports, W-94* .
- Coull, J. D. and Hodson, H. P. (2011), ‘Unsteady boundary-layer transition in low-pressure turbines’, *Journal of Fluid Mechanics* **681**, 370–410.
- De Zhou, M. and Squire, L. (1985), ‘The interaction of a wake with a turbulent boundary layer’, *The Aeronautical Journal* **89**(882), 72–81.
- Dryden, H. L. (1937), ‘Air flow in the boundary layer near a plate’, *NACA Tech. Rep. 562* .
- Ellingsen, T. and Palm, E. (1975), ‘Stability of linear flow’, *The Physics of Fluids* **18**(4), 487–488.
- Emmons, H. (1951), ‘The laminar-turbulent transition in a boundary layer-part 1’, *Journal of the Aeronautical Sciences* **18**(7), 490–498.
- Falco, R. and Gendrich, C. (1990), ‘The turbulence burst detection algorithm of Z. Zaric’, *Near-wall turbulence* pp. 911–931.
- Fasel, H. F. (2002), ‘Numerical investigation of the interaction of the Klebanoff-mode with a Tollmien–Schlichting wave’, *Journal of Fluid Mechanics* **450**, 1–33.

- Fasihfar, A. and Johnson, M. W. (1992), An improved boundary layer transition correlation, *in* ‘ASME 1992 International Gas Turbine and Aeroengine Congress and Exposition’, American Society of Mechanical Engineers, pp. V004T09A025–V004T09A025.
- Fransson, J. H. M. (2003), Flow control of boundary layers and wakes, PhD thesis, KTH Royal Institute of Technology.
- Fransson, J. H., Matsubara, M. and Alfredsson, P. H. (2005), ‘Transition induced by free-stream turbulence’, *Journal of Fluid Mechanics* **527**, 1–25.
- Gomes, R. A., Stotz, S., Blaim, F. and Niehuis, R. (2015), ‘Hot-film measurements on a low pressure turbine linear cascade with bypass transition’, *Journal of Turbomachinery* **137**(9), 091007.
- Haj-Hariri, H. (1988), ‘Transformations reducing the order of the parameter in differential eigenvalue problems’, *Journal of Computational Physics* **77**(2), 472–484.
- Halstead, D. E., Wisler, D. C., Okiishi, T. H., Walker, G. J., Hodson, H. P. and Shin, H.-W. (1997), ‘Boundary layer development in axial compressors and turbines: Part 1 of 4—composite picture’, *Journal of Turbomachinery* **119**(1), 114–127.
- Harun, Z. (2012), The structure of adverse and favourable pressure gradient turbulent boundary layers, PhD thesis, University of Melbourne.
- Hazarika, B. K. and Hirsch, C. (1995), Transition over c4 leading edge and measurement of intermittency factor using pdf of hot-wire signal, *in* ‘ASME 1995 International Gas Turbine and Aeroengine Congress and Exposition’, American Society of Mechanical Engineers, pp. V001T01A080–V001T01A080.
- He, G., Wang, J. and Pan, C. (2013), ‘Initial growth of a disturbance in a boundary layer influenced by a circular cylinder wake’, *Journal of Fluid Mechanics* **718**, 116–130.
- Hedley, T. B. and Keffer, J. F. (1974), ‘Turbulent/non-turbulent decisions in an intermittent flow’, *Journal of Fluid Mechanics* **64**(4), 625–644.
- Herbert, T. (1988), ‘Secondary instability of boundary layers’, *Annual Review of Fluid Mechanics* **20**(1), 487–526.
- Hultgren, L. S. and Gustavsson, L. H. (1981), ‘Algebraic growth of disturbances in a laminar boundary layer’, *The Physics of Fluids* **24**(6), 1000–1004.

- Jacobs, R. and Durbin, P. (2001), ‘Simulations of bypass transition’, *Journal of Fluid Mechanics* **428**, 185–212.
- Jacobs, R. G. and Durbin, P. A. (1998), ‘Shear sheltering and the continuous spectrum of the orr–sommerfeld equation’, *Physics of Fluids* **10**(8), 2006–2011.
- Jahanmiri, M., Rudra Kumar, S. and Prabhu, A. (1991), ‘A method for generating the turbulent intermittency function’, *Dept. Aero. Engg., Ind. Inst. Science, Bangalore*.
- Johnson, M. W. and Fashifar, A. (1994), ‘Statistical properties of turbulent bursts in transitional boundary layers’, *International Journal of Heat and Fluid Flow* **15**(4), 283–290.
- Jordinson, R. (1970), ‘The flat plate boundary layer: Part 1. Numerical integration of the Orr—Sommerfeld equation’, *Journal of Fluid Mechanics* **43**(4), 801–811.
- Jørgensen, F. E. (2005), *How to measure turbulence with hot-wire anemometers: a practical guide*, Dantec Dynamics.
- Kachanov, Y. S. (1994), ‘Physical mechanisms of laminar-boundary-layer transition’, *Annual Review of Fluid Mechanics* **26**(1), 411–482.
- Keller, F. J. and Wang, T. (1993), Effects of criterion functions on intermittency in heated transitional boundary layers with and without streamwise acceleration, in ‘ASME 1993 International Gas Turbine and Aeroengine Congress and Exposition’, American Society of Mechanical Engineers, pp. V002T08A003–V002T08A003.
- Kenchi, T., Matsubara, M. and Ikeda, T. (2008), ‘Laminar turbulent transition in a boundary layer subjected to weak free stream turbulence’, *Journal of Fluid Science and Technology* **3**(1), 56–67.
- Kendall, J. (1985), Experimental study of disturbances produced in a pre-transitional laminar boundary layer by weak freestream turbulence, in ‘18th Fluid Dynamics and Plasma dynamics and Lasers Conference’, p. 1695.
- Klebanoff, P. (1971), Effect of free-stream turbulence on a laminar boundary layer, in ‘Bulletin of the American Physical Society’, Vol. 16, p. 1323.
- Klebanoff, P. S., Tidstrom, K. and Sargent, L. (1962), ‘The three-dimensional nature of boundary-layer instability’, *Journal of Fluid Mechanics* **12**(1), 1–34.

- Klingmann, B., Boiko, A., Westin, K., Kozlov, V. and Alfredsson, P. (1993), ‘Experiments on the stability of Tollmien-Schlichting waves’, *European Journal of Mechanics-B/Fluids* **12**(4), 493–514.
- Kosorygin, V. and Polyakov, N. P. (1990), Laminar boundary layers in turbulent flows, in ‘Laminar-Turbulent Transition’, Springer, pp. 573–578.
- Kuan, C. and Wang, T. (1990), ‘Investigation of the intermittent behavior of transitional boundary layer using a conditional averaging technique’, *Experimental Thermal and Fluid Science* **3**(2), 157–173.
- Kyriakides, N., Kastrinakis, E., Nychas, S. and Goulas, A. (1999), ‘Aspects of flow structure during a cylinder wake-induced laminar/turbulent transition’, *AIAA Journal* **37**(10), 1197–1205.
- Landahl, M. (1980), ‘A note on an algebraic instability of inviscid parallel shear flows’, *Journal of Fluid Mechanics* **98**(2), 243–251.
- Lee, H. and Kang, S. (2000), ‘Flow characteristics of transitional boundary layers on an airfoil in wakes’, *Journal of Fluids Engineering* **122**(3), 522–532.
- Leontini, J., Thompson, M. and Hourigan, K. (2010), ‘A numerical study of global frequency selection in the time-mean wake of a circular cylinder’, *Journal of Fluid Mechanics* **645**, 435–446.
- Liou, W. W. and Liu, F. (2001), ‘Spatial linear instability of confluent wake/boundary layers’, *AIAA Journal* **39**(11), 2076–2081.
- Liu, X. and Rodi, W. (1991), ‘Experiments on transitional boundary layers with wake-induced unsteadiness’, *Journal of Fluid Mechanics* **231**, 229–256.
- Luchini, P. (1996), ‘Reynolds-number-independent instability of the boundary layer over a flat surface’, *Journal of Fluid Mechanics* **327**, 101–115.
- Luchini, P. (2000), ‘Reynolds-number-independent instability of the boundary layer over a flat surface: optimal perturbations’, *Journal of Fluid Mechanics* **404**, 289–309.
- Mandal, A. and Dey, J. (2011), ‘An experimental study of boundary layer transition induced by a cylinder wake’, *Journal of Fluid Mechanics* **684**, 60–84.
- Matsubara, M. and Alfredsson, P. H. (2001), ‘Disturbance growth in boundary layers subjected to free-stream turbulence’, *Journal of Fluid Mechanics* **430**, 149–168.

- Matsubara, M., Takaichi, K. and Kenchi, T. (2010), Experimental study of boundary layer transition subjected to weak free stream turbulence, *in* ‘Seventh IUTAM Symposium on Laminar-Turbulent Transition’, Springer, pp. 277–282.
- Mayle, R. and Dullenkopf, K. (1990), ‘A theory for wake-induced transition’, *Journal of Turbomachinery* **112**(2), 188–195.
- Menter, F. R., Langtry, R. B., Likki, S., Suzen, Y., Huang, P. and Völker, S. (2006), ‘A correlation-based transition model using local variables—part i: model formulation’, *Journal of turbomachinery* **128**(3), 413–422.
- Meredith, P. (1993), Viscous phenomena affecting high-lift systems and suggestions for future CFD development, *in* ‘AGARD, High-Lift Systems Aerodynamics, CP-515’, pp. 19.1–19.7.
- Mitra, A. (2018), Dynamics of Laminar Separation Bubbles on Low Reynolds Number Airfoils, PhD thesis, Indian Institute of Science.
- Monty, J., Harun, Z. and Marusic, I. (2011), ‘A parametric study of adverse pressure gradient turbulent boundary layers’, *International Journal of Heat and Fluid Flow* **32**(3), 575–585.
- Morkovin, M. V. (1969), On the many faces of transition, *in* ‘Viscous drag reduction’, Springer, pp. 1–31.
- Narasimha, R. (1957), ‘On the distribution of intermittence in the transition region of a boundary layer’, *Journal of Aeronautical Science* **24**, 711–712.
- Norimatsu, R., Takai, S. and Matsubara, M. (2011), Relation between disturbance of boundary layer and free stream turbulence component, *in* ‘ASME-JSME-KSME 2011 Joint Fluids Engineering Conference’, American Society of Mechanical Engineers, pp. 2987–2992.
- Ovchinnikov, V., Choudhari, M. M. and Piomelli, U. (2008), ‘Numerical simulations of boundary-layer bypass transition due to high-amplitude free-stream turbulence’, *Journal of Fluid Mechanics* **613**, 135–169.
- Ovchinnikov, V., Piomelli, U. and Choudhari, M. M. (2006), ‘Numerical simulations of boundary-layer transition induced by a cylinder wake’, *Journal of Fluid Mechanics* **547**, 413–441.
- Pan, C., Wang, J. J., Zhang, P. F. and Feng, L. H. (2008), ‘Coherent structures in bypass transition induced by a cylinder wake’, *Journal of Fluid Mechanics* **603**, 367–389.

- Pfeil, H. and Herbst, R. (1979), Transition procedure of instationary boundary layers, in 'ASME 1979 International Gas Turbine Conference and Exhibit and Solar Energy Conference', American Society of Mechanical Engineers.
- Pomeroy, B. W., Diebold, J. M., Ansell, P. J. and Selig, M. S. (2014), 'Study of burst wakes in a multi-element airfoil flowfield', *AIAA Journal* **52**(4), 821–831.
- Pope, S. B. (2000), *Turbulent flows*, Cambridge university press.
- Rai, M. M. and Moin, P. (1993), 'Direct numerical simulation of transition and turbulence in a spatially evolving boundary layer', *Journal of Computational Physics* **109**(2), 169–192.
- Ramesh, O., Dey, J. and Prabhu, A. (1996), 'Transitional intermittency distribution in a three-dimensional constant pressure diverging flow', *Experiments in Fluids* **21**(4), 259–263.
- Ramesh, O. and Hodson, H. (1999), 'A new intermittency model incorporating the calming effect', *Rolls Royce PLC-Report-PNR* .
- Rudolph, P. K. (1996), 'High-lift systems on commercial subsonic airliners', *NASA Contractor Report 4746* .
- Rumsey, C. L., Slotnick, J. P. and Sclafani, A. J. (2018), Overview and summary of the third AIAA High Lift Prediction Workshop, in 'AIAA Aerospace Sciences Meeting', p. 1258.
- Rumsey, C. L. and Ying, S. X. (2002), 'Prediction of high lift: review of present cfd capability', *Progress in Aerospace Sciences* **38**(2), 145–180.
- Saric, W. (1986), 'Visualization of different transition mechanisms', *Physics of Fluids* **29**, 2770–2770.
- Savill, A. and Zhou, M. (1983), Wake/boundary layer and wake/wake interactions-smoke flow visualization and modeling, in 'Proceeding of the 2nd Asian Congress of Fluid Mechanics', edited by NMC Ko, Science Press, Beijing, pp. 743–754.
- Schmid, P. J. and Henningson, D. S. (2012), *Stability and transition in shear flows*, Vol. 142, Springer Science & Business Media.
- Schneider, S. (1995), 'Improved methods for measuring laminar-turbulent intermittency in boundary layers', *Experiments in Fluids* **18**(5), 370–375.
- Schubauer, G. B. and Klebanoff, P. S. (1955), 'Contributions on the mechanics of boundary-layer transition'.

- Shaw, R., Eng, B., Harcastle, J., Riley, S. and Roberts, C. (1985), 'Recording and analysis of fluctuating signals using a microcomputer', *Measurement* **3**(1), 33–39.
- Smith, A. (1975), 'High-lift aerodynamics', *Journal of Aircraft* **12**(6), 501–530.
- Smith, A. M. O. (1956), 'Transition, pressure gradient and stability theory', *Douglas Aircraft Co., Report ES 26388* .
- Spaid, F. W. (2000), 'High Reynolds number, multielement airfoil flow field measurements', *Journal of Aircraft* **37**(3), 499–507.
- Squire, L. (1989), 'Interactions between wakes and boundary-layers', *Progress in Aerospace Sciences* **26**(3), 261–288.
- Sreenivasan, K. (1988), A unified view of the origin and morphology of the turbulent boundary layer structure, *in* 'Turbulence Management and Relaminarisation', Springer, pp. 37–61.
- Taylor, G. (1939), Some recent developments in the study of turbulence, *in* 'In Proc. 5th Intl Congr. Appl. Mech.', Wiley, New York, pp. 294–310.
- Tennekes, J. L. and Lumley (1972), *A first course in turbulence*, MIT press.
- Townsend, A. (1948), 'Local isotropy in the turbulent wake of a cylinder', *Australian Journal of Chemistry* **1**(2), 161–174.
- Van Dam, C. P. (1999), 'Recent experience with different methods of drag prediction', *Progress in Aerospace Sciences* **35**(8), 751–798.
- Van Ingen, J. (1956), 'A suggested semi-empirical method for the calculation of the boundary layer transition region', *Technische Hogeschool Delft, Vliegtuigbouwkunde, Rapport VTH-74* .
- Varghese, J. (2016), Linear Instability and Transition of Incompressible Plane Wall Jet, Master's thesis, Indian Institute of Science.
- Veerasamy, D. (2011), Experimental Investigation of Turbulent Plane Wall Jet, Master's thesis, Indian Institute of Science.
- Walker, G. and Solomon, W. (1992), Turbulent intermittency measurement on an axial compressor blade, *in* '11th Australasian Fluid Mechanics Conference', pp. 1277–1280.

- Watanabe, S., Kato, H. and Yamamoto, K. (2006), Velocity field measurements of a wing-flap configuration via stereoscopic piv, *in* '44th AIAA Aerospace Sciences Meeting and Exhibit', p. 43.
- Westin, K., Boiko, A., Klingmann, B., Kozlov, V. and Alfredsson, P. (1994), 'Experiments in a boundary layer subjected to free stream turbulence: Part 1- Boundary layer structure and receptivity', *Journal of Fluid Mechanics* **281**, 193–218.
- Wu, X., Jacobs, R. G., Hunt, J. C. and Durbin, P. A. (1999), 'Simulation of boundary layer transition induced by periodically passing wakes', *Journal of Fluid Mechanics* **398**, 109–153.
- Wynanski, I., Champagne, F. and Marasli, B. (1986), 'On the large-scale structures in two-dimensional, small-deficit, turbulent wakes', *Journal of Fluid Mechanics* **168**, 31–71.
- Zhang, D., Chew, Y. and Winoto, S. (1996), 'Investigation of intermittency measurement methods for transitional boundary layer flows', *Experimental Thermal and Fluid Science* **12**(4), 433–443.